

Laura Susana Vargas Valencia

**Human Gait Monitoring:
Methods and Systems Using Wearable
Technologies**

Vitoria - Brazil

August 2019

Laura Susana Vargas Valencia

Human Gait Monitoring: Methods and Systems Using Wearable Technologies

Thesis submitted to the Postgraduate Program in Electrical Engineering (PPGEE), Federal University of Espirito Santo (UFES) as a preliminar requirement to obtain the PhD degree in Electrical Engineering.

Federal University of Espirito Santo - UFES, Brazil
Postgraduate Program in Electrical Engineering

Supervisor: Dr. Anselmo Frizera Neto

Co-supervisor: Dr. Teodiano Freire Bastos

Vitoria - Brazil

August 2019

Ficha catalográfica disponibilizada pelo Sistema Integrado de
Bibliotecas - SIBI/UFES e elaborada pelo autor

V297h VARGAS VALENCIA, LAURA SUSANA, 1988-
Human Gait Monitoring: Methods and Systems Using
Wearable Technologies / LAURA SUSANA VARGAS
VALENCIA. - 2019.
147 f. : il.

Orientador: Anselmo Frizera Neto.

Coorientador: Teodiano Freire Bastos Filho.

Tese (Doutorado em Engenharia Elétrica) - Universidade
Federal do Espírito Santo, Centro Tecnológico.

1. Wearable sensors. 2. Inertial sensors. 3. POF sensors. 4.
Sensor fusion. 5. Sensor-to-body calibration. 6. Joint angles. I.
Frizera Neto, Anselmo. II. Bastos Filho, Teodiano Freire. III.
Universidade Federal do Espírito Santo. Centro Tecnológico. IV.
Título.

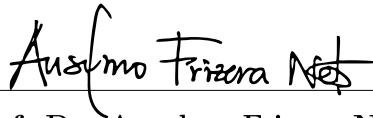
CDU: 621.3

Laura Susana Vargas Valencia

Human Gait Monitoring: Methods and Systems Using Wearable Technologies

Thesis submitted to the Postgraduate Program in Electrical Engineering (PPGEE), Federal University of Espírito Santo (UFES) as a preliminar requirement to obtain the PhD degree in Electrical Engineering.

Examined by:



Prof. Dr. Anselmo Frizera Neto
Supervisor (PPGEE/UFES/Brazil)



Prof. Dr. Teodiano Freire Bastos Filho
Co-supervisor (PPGEE/UFES/Brazil)



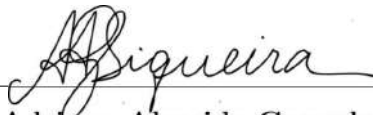
Prof. Dr. Eduardo Rocon de Lima
Jury (CAR/CSIC/Spain)



Prof. Dr. Luis Eduardo Rodríguez Cheu
Jury (ECIJG/Colombia)



Prof. Dr. Patrick Marques Ciarelli
Jury (DEL/UFES/Brazil)



Prof. Dr. Adriano Almeida Gonçalves Siqueira
Jury (EESC/USP/Brazil)

Vitoria, Brazil

To Magdo, Miguel, Jesús and Susana, my great loves.
Thank you so much!

Acknowledgements

Firstly, I would like to thank God for allowing me to reach one more achievement in my life.

I would like to thank my parents, my brother and my fiancé for their unconditional love, support and for always encouraging me in the most difficult moments. I can't express in words how much I love you all. Magdo, my love, I wouldn't have done it without your help. You and your family made me happy in many difficult times.

My sincere gratitude to my advisors, Dr. Anselmo Frizera Neto and Dr. Teodiano Bastos Filho, for their guidance, patience and friendship. Also for giving me the opportunity to work in the Center for Assistive Technology (Núcleo de Tecnologia Assistiva - NTA) and for trusting in my work. Anselmo, thank you very much for your patience and understanding.

My kinder thanks to my colleagues Felipe Schneider and Arnaldo Leal Junior for sharing knowledge with me and for their help in the final stage of this work.

I would like to thank Pablo, Catalina, Prof. Alexander Sierra and Prof. Dr. Luis Eduardo Rodríguez Cheu for all their help and support during my short research visit at the Colombian School of Engineering Julio Garavito. Also, I am grateful to all experiment participants and lab staff.

Also, I would like to express my gratitude to my friends, Denis, Eliete, Nicolas, Alan and Jessica for always telling me not to give up during the last months of this process, and for sharing with me knowledge and funny moments.

I would like to thank Cecilia, Astrid, Javier, Aline, Silas, Hamilton, German, Fabiane, Alexander and Graciela for sharing a home with me in different moments of this process. Great friendships remain for my life.

I thank to all my friends and colleagues of NTA group, specially to Rosita, Kevin, Alejandra, John, Thomaz, Christiane, Andrés, Mario, Manuel, Jonathan and Dolores for sharing with me knowledge and life experiences.

This research was financed by CAPES (process numbers 88882.160536/2017-01, 88887.095626/2015-01), FAPES (80605893, 85426300 and 84336650) and CNPq (304192/2016-3).

Abstract

Several diseases and accidents can lead to motor impairments, preventing humans from normal daily life activities. In order to diagnose and treat the population suffering from walking disabilities, clinicians and physical therapists need tools that help to assess and analyze gait patterns. Nowadays, the gold standard in motion assessment are systems comprised by infrared high speed cameras and reflective markers. However, such systems are expensive and require a dedicated environment, limiting their use to indoors ambients and constrained spaces. Alternatively, new sensor approaches are now shifting the paradigm from the bulk and expensive systems to wearable and more affordable technologies. Among others, inertial measurement units (IMU) are being widely used to assess human movements with little interference to user activities. Moreover, recent studies have demonstrated the feasibility of using optical fiber based curvature sensors to measure joint angles. Their adaptability, low-cost, light-weight and electromagnetic immunity are features that make them an interesting alternative technology. As a first contribution of this Ph.D thesis, we present a novel calibration procedure as a method to align IMUs to body segments, which, compared to other methods in the literature, is a faster and simpler sensor placement method, with no need predefined movements at calibration nor any additional tools. The promising results demonstrate the potential of this IMU-to-body alignment method to become an alternative to high-cost camera-based systems, allowing the possibility of performing human gait analysis in external environments, and with clinical application in the near future. As a second contribution, we developed a novel IMU-POF sensor fusion system for knee angle monitoring, which consists of merging signals from two IMUs and a polymeric optical fiber (POF) curvature sensor. The fusion method relies more on IMUs or POF curvature sensor data depending on the gait cycle phase, generating a filtered output that is more accurate than any of the independent sensors. Our proposed system presented better performance (mean RMSE $< 3.3^\circ$, LFM coefficients $a_1 = 0.99 \pm 0.04$, $a_0 = 0.70 \pm 2.29$, $R^2 = 0.98 \pm 0.01$ and $\rho_C > 0.99$) when compared to other methods in the literature. In summary, this Ph.D. thesis contributes to the state-of-the-art about the use of wearable technologies for motion analysis by improving the accuracy and usability of new sensors towards in-home motion monitoring and clinical scenarios.

Keywords: Inertial sensor, polymeric optical fiber curvature sensor, IMU alignment, multiplicative extended Kalman filter, gait analysis.

Glossary

3CRTF Three Criteria Filter.

ACL Anterior Cruciate Ligament.

ALLOR Advanced Lower Limb Orthosis for Rehabilitation.

AMR Anisotropic Magneto Resistance.

CCC Concordance Correlation Coefficient.

CF Complementary Filter.

CP Cerebral Palsy.

DCM Direction Cosine Matrices.

DOF Degree of Freedom.

DPS Degrees per Second.

EKF Extended Kalman Filter.

FSR Force Sensitive Resistor.

GPS Global Positioning System.

HS Heel Strike.

I2C Inter-Integrated Circuit.

ICC Intra-Class Correlation.

IHA Instantaneous Helical Axis.

IMU Inertial Measurement Unit.

ISB International Society of Biomechanics.

JCS Joint Coordinate System.

KF Kalman Filter.

KPF Knitted Piezoresistive Fabric.

LFM Linear Fit Method.

MAP Maximum a Posteriori.

MEKF Multiplicative Extended Kalman Filter.

MEMS Microelectromechanical Systems.

NTA Nucleo de Tecnologia Assistiva.

NZC Noise Zero-Crossing.

OA Osteoarthritis.

PCA Principal Component Analysis.

PCB Printed Circuit Board.

PMMA Polymethyl Methacrylate.

POF Polymeric Optical Fiber.

RMSE Root Mean Square Error.

ROM Range of Motion.

SCI Spinal Cord Injury.

SD Standard Deviation.

TO Toe Off.

UKF Unscented Kalman Filters.

UWB ultrawideband.

WHO World Health Organization.

ZKA Zero Knee Angle.

List of Tables

3.1	Definition of technical-anatomical quaternions obtained during calibration posture (straight upright posture).	36
3.2	Body fixed, floating and references axes of each joint.	38
3.3	Rotations of the hip, knee and ankle joint of the right leg.	38
3.4	Joint rotations as functions of quaternions.	39
3.5	Representations of the J joint formed by S1 and S2 segments.	42
3.6	Joint angles parameters for gait analysis.	45
3.7	Test-Retest study on two days apart: Consistency of measures of the IMU system.	49
3.8	RMSE between the measurements from IMU system and the reference universal goniometer. Maximum RMSE values of each angular component are highlighted on orange color, and the acceptable values for angular components β and γ are highlighted on green color.	50
3.9	CCC between the measurements from IMU system and the reference universal goniometer. Minimum CCC values of each angular component are highlighted on orange color, and the acceptable values for angular components β and γ are highlighted on green color.	51
3.10	Mean (SD) of the discrete parameters reported for five volunteers.	53

4.1	Standard deviation values of gyroscopes, gyro biases, accelerometers and POF curvature sensor noise.	84
4.2	Methods vs. gold standard, accuracy expressed in terms of Root Mean Square Error (RMSE).	85
4.3	Methods vs. gold standard, repeatability and reproducibility expressed in terms of the Linear Fit Method (LFM).	87
4.4	Methods vs. gold standard, reproducibility expressed in terms of the Concordance Correlation Coefficient (CCC).	88
4.5	Comparing the proposed method to the literature. Accuracy expressed in terms of the Root Mean Square Error (RMSE).	93
4.6	Comparing the proposed method to the literature. Repeatability and reproducibility expressed in terms of the Linear Fit Method (LFM) coefficients. . . .	94
4.7	Comparing the proposed method to the literature. Reproducibility expressed in terms of the Concordance Correlation Coefficient (CCC).	95

List of Figures

2.1	Gait phases and events (Source: Adapted from WHITTLE, 2007).	17
2.2	Human anatomy planes (Source: Adapted from AnatomyNote, 2019).	18
2.3	Hip, knee and ankle joint motion. (Source: Adapted from WHITTLE, 2007). . .	19
3.1	Technical-anatomical frames (B) of the pelvis, thigh, shank and foot. Axes X, Y and Z in color red, green and blue, respectively.	37
3.2	Scheme of a simplified joint comprising two semi-spheres. (a) Adjacent segments $S1$ and $S2$, and a universal goniometer (a controlled joint J); (b) representations of the joint J and (c) rigid plastic piece (green) to fit the sensors in a fixed position on the semi-sphere.	41
3.3	Sensor placement on the human lower limb.	44
3.4	Simulation of the simplified joint. Scale models of the rigid-body joint and IMUs in MATLAB.	47
3.5	Comparison between the joint angles without applying the proposed procedure (a–c) and applying the procedure (d). Angular components α , β and γ are significant in the first case (a–c), which are different of the expected values. In the last case, only α is significant and equal to the expected values. β and γ are both equal to zero throughout the entire simulation, as expected. J_1 and J_4 are two representations of the simulated joint J represented by the goniometer. . . .	48

3.6	Discrete angular parameters on joint angles of Subject 2.	53
3.7	Joint angular kinematics in stride percentage (from HS to HS) of five able-body subjects. Fifteen gait cycles were summarized by black curve (MEAN) and orange stripe (\pm SD).	54
4.1	IMU-POF based knee sleeve system. (a) Knee sleeve system placed on a participant. Instrumented part: (b) main hardware unit and (c) second unit	61
4.2	Human knee as a single degree of freedom (1-DOF) hinge joint. \mathbf{j} is the knee main axis in a global coordinate system, and \mathbf{j}_1 and \mathbf{j}_2 are the same axis in the local coordinate systems of the thigh's and shank's sensors, respectively.	65
4.3	Reliability intervals of the accelerometers and POF curvature sensor for each gait cycle. (a) Angular velocity of the shank's gyroscope medio-lateral axis, $\omega_{2_{ML}}$ (blue curve), knee angular velocity, KAV (orange curve), absolute value of the difference of the acceleration magnitudes (yellow curve), heel strike (HS) events (green dot mark), toe off (TO) events (blue dot mark), toe strike (aTS) events (red square mark), heel off (aHO) events (purple square mark), the end of the mid-swing (eMSw) phase (orange triangle mark), points where the difference of the acceleration magnitudes is below a threshold η_a (black dot mark). (b) Accelerometers-based joint angle (light blue curve), reference (Vicon) angle (blue curve), RI-ACC (blue stripe). (c) POF curvature sensor-based joint angle (light blue curve), RI-POF (blue stripe).	68
4.4	Experimental setup for POF curvature sensor characterization	70
4.5	Marker set (Plug-in Gait lower body model), additional marker clusters and IMU-POF system placed on a participant.	79

4.6	POF curvature sensor characterization. (a) Estimated angle by POF curvature sensor in three sequential flexion/extension cycles compared to the reference potentiometer. (b) POF curvature sensor-based knee joint angle compared with the reference camera-based system during walking. POF sensor response before (c) and after (d) applying the compensation technique using the experimental setup.	83
4.7	The worst case among 12 subjects (S1-S12) for each method when comparing with the reference system. (a) S9, (b) S3, (c) S10, (d) S12 and (e) S11.	86
4.8	Performance of single-sensor and multi-sensor fusion methods. Mean and standard deviation of (a) RMSE, and LFM coefficients (b) a_1 and (c) a_0 . n.s, non-significant p-value > 0.05 , *p < 0.05 , **p < 0.01 , ***p < 0.001	86
4.9	Repeatability and reproducibility of (a) Gyro-based method, (b) Accelerometer-based method, (c) POF-based method, (d) Gyro+Acc fusion (MEKF) method and (e) IMU+POF fusion (MEKF) method. Mean R^2 and ρ_C for all participants. Specific Method versus reference system.	89
4.10	The worst case among 12 subjects (S1-S12) for each method when comparing to the reference system. (a) S11 (b) S9 (c) S9 (d) S11.	92
4.11	Performance of CF, PCA-based, GO+ZKA and our IM+POF (MEK) methods. Mean and standard deviation of (a) RMSE, and LFM coefficients (b) a_1 and (c) a_0 . n.s, non-significant p-value > 0.05 , **p < 0.01 , ***p < 0.001	96
4.12	Repeatability and reproducibility of (a) Complementary Filter (CF), (b) PCA-based, (c) GO+ZKA based and (d) Our IMU+POF based MEKF method. Mean R^2 and ρ_C for all participants. Specific Method versus Reference system.	97

Contents

Acknowledgements	v
List of Tables	xi
List of Figures	xiii
1 Introduction	1
1.1 Motivation	2
1.2 Objectives	5
1.3 Justification	6
1.4 Organization	14
2 Theoretical Background	16
2.1 Human Gait	16
2.1.1 Gait Cycle	17
2.1.2 Planes and Axes of Human Motion	18
2.1.3 Movement Description	19

2.2	Fundamentals of Inertial Sensors and Intensity Variation-based POF Curvature	
	Sensors	20
2.2.1	Gyroscopes	20
2.2.2	Accelerometers	21
2.2.3	Magnetometers	22
2.2.4	Intensity Variation-based POF Curvature Sensors	23
2.3	Attitude and Motion Dynamics: Mathematical Representation	25
2.3.1	Euler Angles	25
2.3.2	Direction Cosine Matrices (DCM)	26
2.3.3	Quaternions	26
2.4	Human Gait Multi-sensor Fusion Methods	29
2.4.1	Variations of Non-linear Kalman Filters	29
2.4.2	Other Fusion Methods	30
2.5	Preliminary Conclusions	31
3	An IMU-to-Body Alignment Method Applied to Human Gait Analysis	32
3.1	IMU-to-Body Alignment Method	34
3.1.1	Calibration Algorithm and Definition of Technical-Anatomical Frames . .	34
3.1.2	Joint Angles Calculation	37
3.2	Validation Protocol of Calibration Procedure Using a Simplified Rigid-Body Joint	40
3.2.1	Motion Acquisition System	40
3.2.2	Experimental Procedure	40

3.2.3	Data Reduction and Statistical Analysis	42
3.3	Application of the Calibration Procedure on Able-Bodied Subjects	43
3.3.1	Sensor Placement on Human Lower Limb	43
3.3.2	Discrete Parameters of the Joint Angles	44
3.3.3	Experimental Protocol for Gait Analysis	45
3.4	Results and Discussion	46
3.4.1	Simulation of the Proposed Method Applied to a Simplified Rigid-Body Joint	46
3.4.2	Practical Validation of the Proposed Method Applied to a Simplified Rigid-Body Joint	49
3.4.3	Experimental Validation for Gait Analysis	53
3.5	Preliminary Conclusions	55
4	Sleeve for Knee Angle Monitoring: A Novel IMU-POF Sensor Fusion System	56
4.1	Introduction	56
4.2	A Novel IMU-POF Based Knee Sleeve System	60
4.3	Methods for IMU-POF based Knee Joint Angle Measurement	62
4.3.1	Estimation of Knee Flexion-Extension Axis and Position Using IMUs	62
4.3.2	Gait Detection Phases Using IMUs	67
4.3.3	POF Curvature Sensor	69
4.3.4	IMU-POF Based Multiplicative Extended Kalman Filter (MEKF)	71
4.4	Experiments	77

4.4.1	Participants	78
4.4.2	Protocol	78
4.4.3	Data Analysis	80
4.4.4	Statistical Analyses	80
4.5	Results and Discussion	82
4.5.1	POF Curvature Sensor Characterization	82
4.5.2	Comparison of Single-sensor and Multi-sensor Fusion Methods	84
4.5.3	Comparison of the IMU-POF Based MEKF with Other Methods in the Literature	91
4.6	Preliminary Conclusions	100
5	Conclusion	102
5.1	Publications	105
	Appendix A	108
A.1	Flowchart: IMU-to-Body Alignment Method	109
A.2	Three Criteria Filter (3CRTF)	110
A.3	Estimation of Knee Main Axis of Motion	111
A.4	Estimation of Knee Joint Position	111
A.5	RI-ACC and RI-POF Intervals Definition	112
A.6	IMU-POF based MEKF	113
A.7	Flowchart: IMU-POF based MEKF	114

Chapter 1

Introduction

This Ph.D. thesis introduces a set of novel methods to perform human motion analysis using wearable technologies. Lower limb motion analysis plays a fundamental role in the diagnosis and treatment of walking impairment. The use of Inertial Measurement Units (IMUs) for this purpose represents an ambulatory and ease-to-handle motion capture solution. Several challenges and limitations regarding human motion analysis continue latent in the current state of the art, and through the proposed methods in this thesis some of these drawbacks are overcome.

In this thesis we present a novel IMU-to-body alignment method, with fast and simple sensor placement, using an inertial sensor network with no need of complex calibration movements. Additionally, we developed a novel wearable system for joint angle estimation based on two IMUs and a polymeric optical fiber (POF). With the data from the IMUs and POF we elaborated a sensor fusion method based on Multiplicative Extended Kalman Filter, in order to reach a reliable knee joint angle estimation.

This introductory chapter presents the background and rationale of this work. It gives some statements concerning to the motivation of this research, the justification and the objectives of the developed work.

1.1 Motivation

About 15% of the world population live with some disability condition, of which 2% to 4% suffer significant functional problems (WHO, 2011). Different conditions may alter biomechanical characteristics that define a healthy walking pattern. Frequently, these motor impairments significantly impact a person's ability to function independently in daily life. For instance, stroke is the third leading cause of disability in the world (JOHNSON et al., 2016). Stroke is a brain dysfunction that occurs due to a disturbance in the blood supply flowing to the brain, that may cause irreversible damages (SIMS; MUYDERMAN, 2010). According to the World Health Organization (WHO), 15 million people experience stroke annually worldwide, and of these, 5 million are permanently incapacitated. Stroke consequences depend on which part of the brain is damaged and how seriously it is affected (WHO, 2014). Some post-stroke motor-related symptoms include gait and balance disturbance, coordination problems, functional limb weakness, muscle spasticity and total or partial inability to move the limbs on one side of the body (GARGANO; WEHNER; REEVES, 2011).

Moreover, road traffic crashes, sport accidents, falls, infections, cancer and tumors can cause complete or incomplete damage to the spinal cord, disturbing the normal autonomic and sensory-motor function. Every year, between 250 and 500 thousand persons suffer a spinal cord injury (SCI) worldwide (WHO, 2013a, 2013b). Paralysis, muscle function deficit, weakness, numbness and sensation loss below the level of the injury are some of the symptoms that these people may experience (THOMAS; ZIJDEWIND, 2006).

Furthermore, mobility impairments can often be associated with the elderly population. Till 2050, the projection of people aged over 60 years is expected to grow to 2.1 billion (NATIONS; AFFAIRS, 2017). Diseases are a frequent cause for motor disability in people aged between 65 and 84 years old, such as Alzheimer's dementia and Parkinson's disease. Also, stroke, joint injury, musculoskeletal deformations, and impairments after an orthopedic surgery frequently result in motor impairments in elderly persons (ALEXANDER; GOLDBERG, 2005). Moreover,

age is one of the main risk factors for falls, which is a major public health problem (ORGANIZATION; AGEING; UNIT, 2008). In fact, an estimation of 646 thousands individuals' death due to falls occurs worldwide each year, of which over 80% are in low- and middle-income countries.

Although bones, connective tissues and joints may begin to deteriorate in population over the age of 60, young individuals are also susceptible to conditions such as osteoarthritis and ligament injuries (AMOAKO; PUJALTE, 2014). Overuse of the joints during very active jobs or high-impact/contact sports, and obesity are also risk factors (FOUNDATION, 2018). Osteoarthritis (OA) is one of the most frequent joint diseases, which ranks fifth between all disability conditions worldwide (FOUNDATION, 2018). Joint cartilage wear-and-tear (with eventual loss), surrounding tissue degeneration and bones rubbing together characterize osteoarthritis. Its symptoms include pain, tenderness, loss of flexibility and stiffness, which decrease range of motion (SANTOS et al., 2011; NAKAMURA et al., 2016). Regarding ligament injuries, anterior cruciate ligament (ACL) injury is the most common trauma to the knee, affecting elderly population and especially young athletes. Complete or near complete tearing of the ACL may occur with or without contact, producing deep pain, loss of range of motion with difficulty to straight the affected knee, and instability.

Additionally, motor dysfunction can arise during pregnancy, at birth or after birth up to about age of three. Cerebral palsy (CP) is the most common motor disability in childhood, which affects about 1 in 500 neonates, with an estimated prevalence of 17 million people worldwide (GRAHAM et al., 2016). CP may affect the normal development of infant brain and cause physical disability mainly in the areas motion-related. The most common symptoms of this disorder are involuntary movements, spasticity, balance and posture disturbance, and unsteady gait (ROSENBAUM et al., 2007).

The pervasive presence of the aforementioned prevalent disorders that cause neuromotor impairment demonstrate the need for efficient and objective gait analysis, which plays a fundamental role in the diagnosis and treatment. Usually, gait performance assessment allows measuring ob-

jectively the patients' degree of impairment and health status, evaluate the outcome following a period of physical therapy, and identify indicators which may lead to further injuries (WRISLEY et al., 2004).

Nowadays, technologies used to analyze lower limb motion are migrating from bulky-fixed, dedicated and high cost devices to light, compact, wearable and relatively low-cost sensors. Other issues such as occlusion, controlled environment restrictions, and reduced assessment volume of the optical motion capture systems are also overcome with the use of these new sensors. Furthermore, with the rising healthcare revolution, in-home monitoring (ONDER et al., 2012), telemedicine (ORGANIZATION et al., 2010) and telerehabilitation (HAILEY et al., 2011) are already a reality. Thus, as traditional 3D camera systems are expensive and need time consuming procedures for public and even private health systems, in our Center for Assistive Technology (from Portuguese, Núcleo de Tecnologia Assistiva - NTA), one of the researches fields is dedicated to develop ambulatory and low-cost wearable technologies for human motion analysis, including IMU-based as well as optical fiber-based systems.

In addition, some assistive and rehabilitation technologies are also developed in NTA. For instance, smart walkers (VALADÃO et al., 2016; JIMÉNEZ et al., 2018) and an active knee exoskeleton called ALLOR (Advanced Lower Limb Orthosis for Rehabilitation) (BOTELHO, 2017; VILLA-PARRA et al., 2017) are technologies conceived for gait assistance and rehabilitation of patients with cognitive and motor deficits. As a result, it is evident the need of wireless technologies to measure and estimate human lower-limb motion in order to assess the patient's performance and apply corrective measures when needed, offering better solutions in gait assistance and/or rehabilitation.

In such context, in this Ph.D. thesis we present the development of an inertial motion capture system devoted to assess ambulatory methods for estimating gait kinematics. Moreover, we propose a sensory fusion algorithm that combines data from IMUs with a polymeric optical fiber (POF) curvature sensor, in order to overcome some drawbacks that arise when using only inertial technologies. Such new methods allow implementing more robust and reliable systems

to assess gait kinematics. Accordingly, the two main contributions of this Ph.D. thesis are

1. A method based on a correction with the gravity-vector and a known posture to align the IMU coordinate systems to the anatomically-defined coordinate systems, which may be used to improve the joint angle estimation in gait kinematic analysis.
2. A sensory fusion algorithm that combines data from two IMUs with data from an intensity variation-based POF curvature sensor, which may be used to estimate with higher accuracy the knee joint angle, improving its performance when compared to both systems separately.

1.2 Objectives

This Ph.D. thesis aims mainly to design, implement and validate novel methods for gait analysis using wearable technologies, in order to provide a reliable system to assess the functional performance of people with motor impairment. Around this main objective, the following specific objectives and scientific challenges are proposed and addressed here:

1. To perform a literature study regarding methods and techniques for gait assessment using IMUs and polymeric optical fiber (POF), as well as data fusion approaches.
2. To develop an IMU-to-body alignment method in order to improve estimation of hip, knee and ankle joint angles. This method aims to be a new approach to approximate sensor coordinate systems to anatomically-defined coordinate systems.
3. To develop a novel wearable system based on two IMUs and a polymeric optical fiber (POF) curvature sensor for knee joint angle estimation. This system should be a portable, adaptable and flexible device to assess gait towards an in-home mobile motion monitor.
4. To develop a sensor fusion technique to merge inertial data provided by accelerometers and gyroscopes with data from an intensity variation-based POF curvature sensor in order to estimate joint angle in an improved way.

5. To assess and validate the proposed wearable system against a gold standard system used as a reference. This validation will be a proof of concept of all designed and implemented systems and algorithms developed in this thesis.

1.3 Justification

Lower-limb motion systematic study is essential for several applications and disciplines, such as neuro-rehabilitation and physical therapy. The gold standard method for gait analysis is the optical motion tracking based on infrared multi-camera systems and reflective markers. Although optical instruments are widely used, these systems present some disadvantages, such as being bulky, dedicated, volume-limited and high-cost. In addition to these disadvantages, these optical systems perhaps are not suitable to real-time ambulatory applications, making them impractical for telerehabilitation (KONG et al., 2013).

For this reason, several research groups currently invest efforts in the development and validation of mobile motion capture systems to provide reliable tools for therapists and clinicians to conduct gait assessment either during diagnosis and/or rehabilitation phases. In this context, IMUs are an in-rising alternative as wearable systems for motion tracking. For gait analysis, each body segment intended to be tracked should have at least one IMU placed on it. And each IMU should provide measurements, usually in three dimensions, of the angular velocity, acceleration, and magnetic field vector in its local sensor frame.

However, the use of inertial sensors for motion analysis still yields many challenges. For instance, some studies have questioned their accuracy (PICERNO; CEREATTI; CAPPOZZO, 2011; BERGAMINI et al., 2014; PASCUTO et al., 2015; LEBEL et al., 2013; BRENNAN et al., 2011). Regarding to this matter, when using IMU-based motion capture systems, errors that compromise data quality and, consequently, kinematic analysis accuracy, can be classified as follow:

1. Instrumental errors, which include accelerometers, gyroscopes and magnetometers perfor-

mance, as well as sensory fusion techniques.

2. Misalignment errors, which refer to the alignment between the IMU coordinate system (or axes) and the anatomically-defined coordinate system (or joint motion axes).
3. Soft-tissue artifacts, which point to the relative motion between the IMU and the underlying body-segment.

Concerning to the instrumental errors, researches state that appropriate calibration of the individual sensors need to be carried out in the manufacturing processes as well as in the applications conducted by the end-user (BERNOULLI et al., 2010; MARTIN; GROVES; NEWMAN, 2016). Since the manufacturing process of the sensors are technologically improving, it is expected that some manufacturing errors will be compensated before commercialization. Such errors include scale factors, bias offsets, non-linearity and axis misalignment. Some of these errors are sensitive, but not only, to temperature variations. Consequently, internal temperature sensors are included on-chip by most manufacturers to compensate drifts. An extended explanation of the aspects and parameters to be considered during characterization of these sensors can be found in (GREWAL; WEILL; ANDREWS, 2007; MARTIN; GROVES; NEWMAN, 2016). Perhaps, a pervasive problem is to find commercially available IMUs without these initial compensations or without informed parameters in their datasheets. For this reason, a proper calibration is a complex task to be performed before using IMUs.

Moreover, to describe Earth's magnetic field distortions that lead to magnetometer errors, hard-iron and soft-iron concepts should also be introduced. Hard-iron distortions occur when an external component, on the magnetometer board or platform, generates a constant magnetic field causing superposition of magnetic fields. Soft-iron effects are associated with materials that do not generate a magnetic field, but affect the magnetic field around themselves. These effects are highly complex and cannot be easily modeled during in-run unrestrained movements (GEBRE-EGZIABHER et al., 2006). In our research group, a recent work presented a magnetometer calibration algorithm based on a method of least squares using the algebraic

distance metric (MUCCIACCIA, 2017).

Additionally, most manufacturers supply sensor fusion algorithms to estimate IMUs orientation. Some others are available online. For example, a set of them was presented in a recent work (SCHNEIDER, 2018). In other cases, if a specific algorithm is needed, the end-user should implement it. A critical factor is that the most modern filters, apparently more robust, do not have open code access (SCHNEIDER, 2018). This limitation may lead other researchers to mathematical misinterpretation and long time code development, even prone to make code mistakes.

In essence, sensor fusion techniques comprise merging information from different sensors. This data combination goes beyond the potential of each sensor individually, looking for reliability and higher accuracy. Furthermore, sensor fusion aims to provide a system less susceptible to fault conditions and can yield new information, that none of the sensors alone can measure directly (WALTZ; LLINAS et al., 1990).

Regarding IMU motion capture systems, data fusion algorithms aim to minimize the drift of orientation data, due to the angular velocity integration, by using accelerometers and magnetometers measurements (ZHU; ZHOU, 2004). Thus, assuming that gravitational acceleration dominates the accelerometer measurements, tilt drift minimization is possible. Likewise, azimuth (or heading) drift decreases using the magnetometer measurements (ZHU; ZHOU, 2004). Hence, it remains in evidence that significant dynamic accelerations and magnetic disturbances affect the orientation accuracy (NOGUEIRA et al., 2017; LUINGE; VELTINK, 2005; ROETENBERG et al., 2005). In cases of significant dynamic accelerations, some researchers propose a fixed threshold to calculate reliable acceleration time intervals (NOGUEIRA et al., 2017; VITALI et al., 2017).

Sometimes, other aiding sensors are used to overcome the mentioned drawbacks. On the one hand, inertial sensors can be used in combination with Global Positioning System (GPS) for step-length estimation (KAO; CHEN; LIN, 2011) and pedestrian navigation systems (BAN-

CROFT; LACHAPELLE, 2011). As an example, recently, the integration of IMU and an ultrasonic sensor was presented in (XIA et al., 2019). On the other hand, IMUs in combination with a single 3D depth sensor (i.e. Microsoft Kinect) using linear Kalman Filter (KF) and a complementary filter were presented in (KALKBRENNER et al., 2014) and (GLONEK; WOJCIECHOWSKI, 2017), respectively. In (MARCARD et al., 2018), a fusion between a moving camera (i.e. smartphone camera) and IMUs to recover 3D human pose was proposed, with the authors solving the fusion problem by optimizing the weighted-variables of an equation that related IMUs and camera measurements through the gradient-based Levenberg-Marquardt.

Alternatively, Kok, Hol and Schön (2015) presented an indoor 6D position and orientation pose system using a combination of accelerometers, gyroscopes and time-of-arrival measurements from an ultrawideband (UWB) system. The authors formulated the position-orientation problem as a maximum a posteriori (MAP) problem, which was solved using an optimization approach. Similarly, a magnetometer-free algorithm for lower-limb motion capture by fusing signals from accelerometers and gyroscopes with an UWB location system was presented in (ZIHAJEZHDEH; PARK, 2017), in which the authors proposed a novel Kalman Filter-based fusion algorithm to track 3D location and posture.

In another research, Lim et al. (2008) used accelerometer and magnetometer measurements to calibrate a gyroscope and a miniature optical linear encoder through a complementary-approach data fusion algorithm. The proposed system was used to estimate a single Degree of Freedom (DOF) elbow joint angle. In a like manner, an arm movement capture system integrating an optical linear encoder and accelerometer was proposed in (NGUYEN et al., 2011), in which accelerometer measurements give the link's orientations, and the encoder provides the joint angles. Also, some rotations are tracked using the accelerometer. However, it is not clear if a compensation between measurements exist, so it seems that a properly-said data fusion is not completed. Otherwise, Tognetti et al. (2015) proposed to combine signals from accelerometers with a piezoresistive goniometer for knee joint angle measurement. The authors implemented an indirect Kalman Filter to estimate the calibration parameter errors in order to correct the

measured angle by the goniometer.

Nevertheless, the aforementioned systems using alternative aiding sensors present some limitations for ambulatory motion capture applications. On the one hand, those GPS-aided systems (KAO; CHEN; LIN, 2011; BANCROFT; LACHAPELLE, 2011) are mainly used to navigation, as their performance is widely affected in indoor environments. In contrast, the effective range of ultrasonic-based systems (XIA et al., 2019) makes them not suitable for use in open areas. Other systems with fixed sensors such as Microsoft Kinect (KALKBRENNER et al., 2014; GLONEK; WOJCIECHOWSKI, 2017) are limited to specific closed and controlled environments. Similarly, UWB-aided systems (KOK; HOL; SCHÖN, 2015; ZIHAEHZADEH; PARK, 2017) are more appropriated to localization problems. Even though these two latter can improve lower-limb motion capture, both systems require fixed instrumentation and closed spaces.

On the other hand, the systems presented in (LIM et al., 2008; NGUYEN et al., 2011; TOGNETTI et al., 2015) are suitable for ambulatory applications. Among these systems, lightweight, portable, and apparently low-cost and low-power consuming, the assessment and characterization of the systems in (LIM et al., 2008; NGUYEN et al., 2011) were limited to upper-limb motion, presenting good correlation when compared to a commercial electrogoniometer. Only Tognetti et al. (2015) presented lower-limb motion capture, nevertheless, one difficulty highlighted by the authors was to evaluate their system against the same IMU system that provide accelerometers data. Another limitation of these three previous studies is that they can monitor only one degree of freedom per joint.

Alternatively, optical fiber sensors, as an emerging technology, present some advantages that make them attractive to develop wearable systems. They are lightweight, flexible, compact, and, unlike some microelectromechanical systems, immune to electromagnetic field. For instance, POF-based systems have demonstrated its adaptability and accuracy to measure joint angle in exoskeleton applications (LEAL-JUNIOR et al., 2017, 2018). In addition, this technology presents multiplexing features, which allow to measure different parameters with a single sen-

sensor (PETERS, 2010), for example angle and temperature (LEAL-JUNIOR et al., 2018a). The aforementioned advantages make optical fiber sensors an interesting option to be embedded in textiles for sensor applications (KREHEL et al., 2014), enabling the fabrication of monitoring systems with better appearance. Moreover, these promising technologies, when are made of malleable materials, such polymeric optical fibers, are successfully applied in soft robotics (LI et al., 2019).

Regarding data fusion methods used to estimate orientation, the state-of-the-art techniques are based mainly on Kalman Filters (KF). These filters are the most popular probabilistic fusion algorithm, representing an optimal solution to minimize the mean squared error between the actual and estimated data (FARAGHER et al., 2012). For non-linear systems and eventually non-Gaussian noise, several variations of the standard linear KF are presented in the literature. Many of these algorithms comprise mathematical complex tasks, and some of them are not clearly described to be replicated by others, as mentioned in (SCHNEIDER, 2018; RANA; HALIM, 2018; PARISI, 2017; POSTOLACHE et al., 2014). The Extended Kalman Filter (EKF) is a direct solution mainly implemented in non-linear approaches, e.g. (YUAN et al., 2019; BAGHDADI; CAVUOTO; CRASSIDIS, 2018; KORTIER et al., 2015; BERGAMINI et al., 2014). Otherwise, Unscented Kalman Filters (UKF) are used in (KANG; JANG; PARK, 2019; TIAN et al., 2015). A characteristic of these filters is that they allow a more accurate estimation of probability density functions under nonlinear transformations. Further comparisons between EKF and UKF, and additional comments about other filters can be found in (FILIPPESCHI et al., 2017). Moreover, the Multiplicative Extended Kalman Filter (MEKF), frequently used in aeronautics, including NASA spacecraft (MARKLEY, 2003), and its variations, e.g. (GHOBADI; SINGLA; ESFAHANI, 2018), have demonstrated superior performance when compared to standard EKFs. Also, it is attractive by its lower computational cost.

Open-access-code data fusion methods widely used in the literature are based on Mahony's and Madgwick's algorithms (MAHONY; HAMEL; PFLIMLIN, 2008; MADGWICK; HARRISON; VAIDYANATHAN, 2011). Other alternative include complementary (SEEL; RAISCH; SCHAUER, 2014; ALAM; ZHAIHE; JIA, 2014) or particle filters (PELTOLA; HILL; MOORE,

2016; ASCHER et al., 2010), fuzzy processing (HONG, 2003), bootstrap attitude, and optimization framework filters (KOK; HOL; SCHÖN, 2014, 2015). However, most of these filters are computationally expensive and of complex implementation.

Concerning misalignment errors, a fundamental problem of IMU-based gait analysis is to provide a sensor-to-body calibration procedure (SEEL; RAISCH; SCHAUER, 2014). Different approaches in the literature attempt to estimate the IMU frame's orientation with respect to the underlying body segment frame (FAVRE et al., 2009; CUTTI et al., 2010; PALERMO et al., 2014; O'DONOVAN et al., 2007). For instance, a protocol named "Outwalk" was presented in (CUTTI et al., 2010), where the authors propose a functional calibration based on pure knee flexion-extension movement to compute distal thigh frame, with pelvis and shank sensors located in a certain position. In another research (BRENNAN et al., 2011), the authors used IMUs (accelerometers and gyroscopes) to quantify 3D joint angle accuracy using an instrumented gimbal as reference. To align the axes, they followed a functional calibration where a predefined movement of a joint in a specific plane is required. Other alignment method was presented in (TADANO; TAKEDA; MIYAGAWA, 2013), where the authors used accelerometers and gyroscopes to analyze 3D joint angle using quaternions, and camera images with markers were used during two static posture to compute the sensor-to-body segment calibration.

Alternatively, Palermo et al. (2014) proposed a two-phases functional calibration procedure, where the subject was asked to remain initially in a standing upright posture and then sitting with legs stretched or lying on a table. Using the gravity vector measurements (from all IMUs) during both postures, they computed the body-to-sensor orientation matrices. In another study, an optimization method to identify the main joint axis was proposed by Seel, Raisch and Schauer (2014). Exploring kinematic constraints of the joints, the authors estimated the joint axis and the position vectors from the joint center to sensor frame origin by minimizing a set of equations through least square method, and using Gauss-Newton algorithm to solve the optimization problem.

In (LEE et al., 2015), a calibration process to calculate the rotation matrix between the sensor

frames and the limb body frames was addressed. The authors used accelerometer and gyroscope measurements during standing posture in combination with movements (i.e. lift up leg without bending the knee, assuming rotations only around one axis) to compute roll, pitch and yaw angles in an initial position.

Nevertheless, these mentioned approaches suffer from some limitations, as most of the alignment methods rely on precise-predefined user movements in specific planes to define the axis of joint motion (CUTTI et al., 2010; BRENNAN et al., 2011; TADANO; TAKEDA; MIYAGAWA, 2013; PALERMO et al., 2014; LEE et al., 2015), present analysis limited only to sagittal plane (SEEL; RAISCH; SCHAUER, 2014; LEE et al., 2015), or use supplementary devices as additional tools (FAVRE et al., 2009; TADANO; TAKEDA; MIYAGAWA, 2013). The need for these additional tools also increases the experiment duration and requires experienced personnel, which may be impractical in daily clinical routine. Also, the difficulty of predefined movements may be hard to execute in daily life and complex to perform for motor impaired subjects.

It is worth mentioning that soft-tissue artifacts, caused by skin and soft-tissue vibrations, are a common problem to IMU-based and optical active-marker motion capture systems. These artifacts are highly variable between subjects and difficult to minimize through modeling (FIORENTINO et al., 2017). This error source was not addressed in this thesis because it is out of the scope of this work.

In addition to these aforementioned error sources that affect human motion capture accuracy, the lack of standard protocols still restricts the usability of IMU-based motion capture systems in many clinical applications, as mentioned in recent studies (AL-AMRI et al., 2018; CHO et al., 2018; CEREATTI; TROJANIELLO; CROCE, 2015).

To conclude, the development and validation of wearable systems that provide a reliable assessment of human motion are still open issues. Thereby, in this work, we propose and validate an alignment method to perform human motion analysis using wearable technologies based on

gravity correction. The advantages of the proposed method, in comparison with other methods described in the literature, include the fast and easy sensor placement, with no need of special movements performed by the user nor any additional tools, which may decrease setup time. Additionally, we present a novel sensor fusion system based on IMUs in combination with a an interesting alternative sensor, namely optical fiber-based curvature sensor, which, as aforementioned, present characteristics such a compactness, portability and mainly immunity to magnetic disturbances. In this way, we contribute to the current state-of-the-art, tackling two error sources when using IMUs for gait analysis.

1.4 Organization

This Ph.D. thesis is organized in five chapters. Chapters 1 is compounded by the motivation that leaded to the developed work, as well as the scientific issues and justification of this Ph.D. proposal, including main objectives.

Chapter 2 describes the theoretical background, presenting a literature study regarding methods and techniques related to inertial measurement sensors, polymer optical fiber curvature sensor and data fusion algorithms. The chapter presents the state-of-the-art review, including available approaches towards gait analysis using wearable technology and sensor data fusion.

Chapter 3 presents a novel calibration procedure as a method to align IMU sensors to body segments, which compared to current state-of-the-art systems, relies on a faster and simpler sensor placement procedure, with no need for any additional tools. The chapter starts with the method that includes the calibration algorithm, definition of technical-anatomical frames and calculation of joint angles. Following, it shows an application of the method on five able-bodied subjects performing a gait test. Finally, the kinematic data of the lower limb joints are presented descriptively.

Chapter 4 describes a novel IMU-POF sensor fusion system that merges data from two different sources: gyroscopes and accelerometers from two IMUs and a polymer optical fiber (POF)

sensor. The chapter begins with the hardware concept of the sleeve system for knee angle monitoring. Then, the mathematical concept of the Multiplicative Extended Kalman Filter (MEKF) fusion algorithm is detailed. Subsequently, the wearable system is evaluated with 12 subjects during a walk experiment, serving as a proof-of-concept for the proposed method. Next, the collected data is merged offline using the fusion method and validated against a gold standard optical camera system.

Chapter 5 concludes this thesis, gathering together the main results and conclusions. Publications originated from this thesis are also summarized. Finally, future research and development activities originated in this thesis are proposed to improve the work presented.

Chapter 2

Theoretical Background

This chapter presents an introduction to the concepts about gait cycle and how this is subdivided in phases and events, followed by the description of planes and axes of motion, are presented in Section 2.1. Then, the fundamentals of inertial sensors and intensity variation-based Polymer Optical Fiber (POF) curvature sensors are presented in Section 2.2. Next, we briefly review the mathematical representation of attitude and motion dynamics in Section 2.3, with more focus given to the quaternions, which are the orientation representation mainly used in this research. Finally, principles for some multi-sensor fusion methods are presented in Section 2.4.

2.1 Human Gait

From biomechanics, human gait is the forward displacement of the center of gravity, and in non-disability conditions, consists of keeping balance by moving harmonically the trunk and lower limbs (WHITTLE, 2007). Biomechanical analysis can be accomplished from two perspectives: kinetics and kinematics (HAMILL; KNUTZEN, 2015). The former refers to the study of accelerations, forces and moments, but without considering the detailed position and orientation of the bodies involved. Contrary, human body kinematics defines the motion of the body segments without any detailed knowledge of the forces that cause such motion (WHITTLE,

2007). In the following subsections, we present some basic concepts of kinematics used in gait analysis.

2.1.1 Gait Cycle

Gait is a chain of successive events that creates a cyclic pattern of movement repeated over time (VAUGHAN et al., 1999). A gait cycle is the basic unit to characterize the way of walking, assuming that successive cycles will be reasonably similar, if not the same. This cycle is subdivided in two main phases, according to Figure 2.1 (WHITTLE, 2007): 1) Stance phase, approximately 60% of the gait cycle, when the foot is in contact with the ground; and 2) Swing phase, approximately 40% of the gait cycle, when the same foot is not in contact with the ground and the leg is moving forward, preparing the next contact. Also, each phase can be subdivided in periods, including loading response, terminal stance, pre-swing and terminal

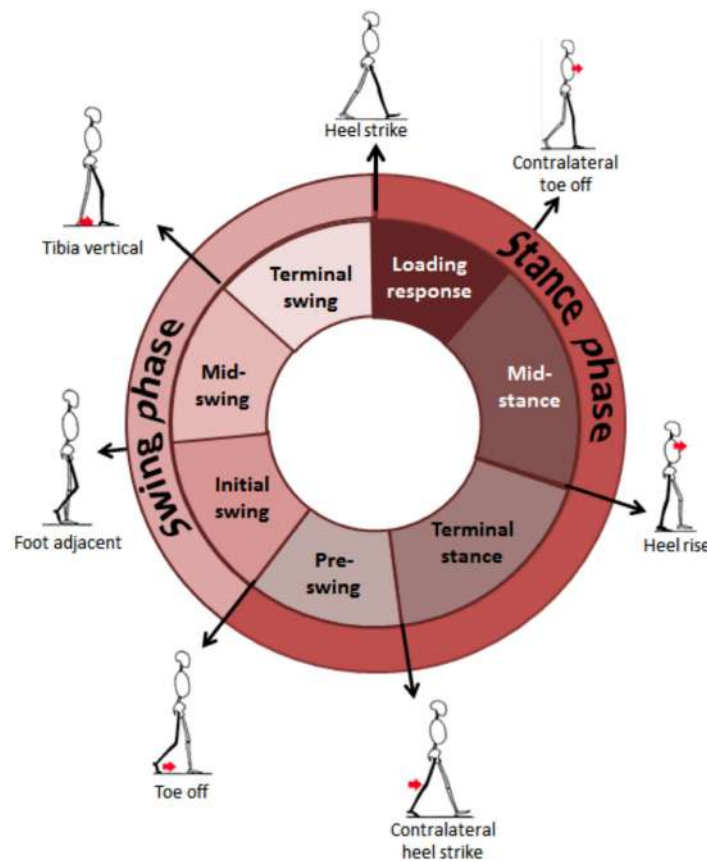


Figure 2.1: Gait phases and events (Source: Adapted from WHITTLE, 2007).

swing (see also Figure 2.1). Details of these periods can be found in (WHITTLE, 2007; TAO et al., 2012). Additionally, seven events subdivide the gait cycle in these periods, which are indicated by arrows in Figure 2.1. For instance, the initial contact or heel strike (HS) is the instant when the heel contacts with the ground, this event represents the beginning of the stance phase and the end of the swing phase. Moreover, toe off (TO) is the instant when the foot leaves the floor, and represents the end of the stance phase and the beginning of swing phase (WHITTLE, 2007).

2.1.2 Planes and Axes of Human Motion

The description of human movement is based on a system of planes and axes (HAMILL; KNUTZEN, 2015). Three imaginary planes are positioned at right angles to each other intersecting at the center of mass of the human body, as represented in Figure 2.2. Any movement can be defined in a specific plane, if it actually occurs along that plane or parallel to it. Also, the movement can be defined about an axis of rotation perpendicular to the plane (see Figure 2.2) (ANATOMYNOTE, 2019). The sagittal plane divides symmetrically the body through the vertical, into right and left sides. The frontal plane (or coronal plane) divides the body

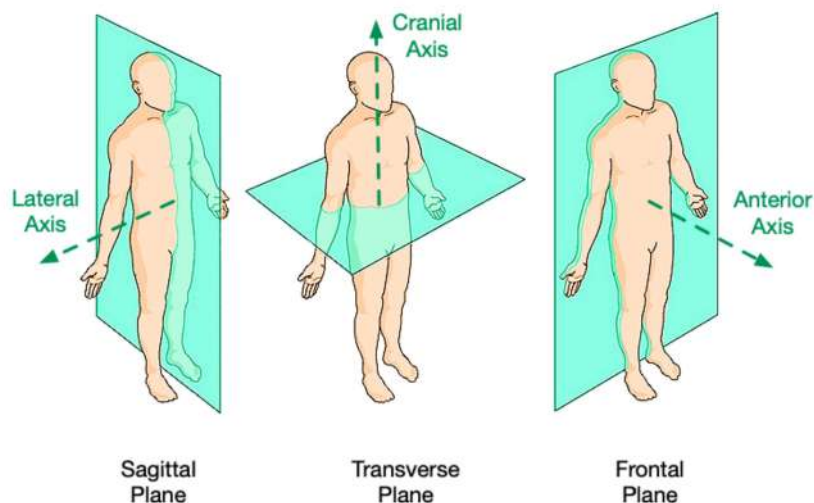


Figure 2.2: Human anatomy planes (Source: Adapted from AnatomyNote, 2019).

into front (anterior) and back (posterior) portions. Finally, the transverse plane (or horizontal plane) divides the body into superior (cranial) and inferior (caudal) portions. The axes of rotation perpendicular to these planes are: mediolateral, anteroposterior and longitudinal (cranial) axis, respectively.

2.1.3 Movement Description

Three-dimensional kinematic quantities can be either linear (position, linear velocity, and linear acceleration) or angular (orientation, angular velocity, and angular acceleration). In gait analysis, angular displacements of hip, knee and ankle joints are some of the kinematic parameters of greatest clinical interest (FAISAL et al., 2019). The directions of the lower limb joint movements in the three planes are shown in Figure 2.3 (WHITTLE, 2007).

Indices such as joint Range of Motion (ROM), maximum joint flexion or extension in a specific gait phase are quite required (SOUCIE et al., 2011; MCCLELLAND et al., 2011). In addition, spatiotemporal parameters are widely used in gait analysis. These parameters can include gait speed, step-length, stride-length, cadence and temporal parameters such as stance and swing time. A measurement summary for clinical gait analysis can be found in (CIMOLIN; GALLI, 2014).

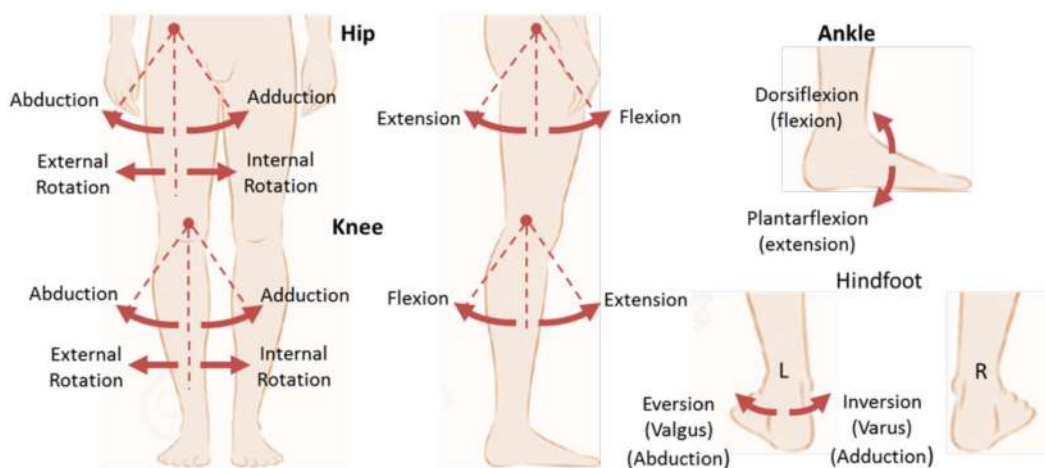


Figure 2.3: Hip, knee and ankle joint motion. (Source: Adapted from WHITTLE, 2007).

2.2 Fundamentals of Inertial Sensors and Intensity Variation-based POF Curvature Sensors

Inertial measurement units (IMUs), also called inertial sensors, provide angular velocity, acceleration and the magnetic field vector in their own three-dimensional local coordinate system. With suitable calibration, the local frame axes describe an orthonormal base normally well aligned with the housing of the sensor. When an IMU is placed on an object, the measurements can be used to estimate the orientation of that object with respect to a fixed (inertial) coordinate system. In the following, we will review the basic principles of MEMS (Microelectromechanical Systems), such as gyroscopes, accelerometers and magnetometers. Additionally, we will introduce an overview of the intensity variation-based POF curvature sensor, which is used in this research as a different aiding sensor to improve accuracy when using inertial sensors for human gait analysis.

2.2.1 Gyroscopes

Gyroscopes measure the angular rate of rotation with respect to a reference inertial coordinate system. MEMS gyroscopes are developed using silicon micro-machining techniques. MEMS inertial sensors are manufactured in bulk, incorporated in miniature chip packages, have low power consumption and low-cost compared to navigation, industrial, automotive and tactical grade sensors (ACAR; SHKEL, 2008). MEMS gyroscopes are based on vibrating mass, which are used to measure angular velocities. A general configuration is composed of two masses oscillating and moving in opposite directions. If an angular velocity occurs, the Coriolis force acts on each mass also in opposite directions, changing the capacitance of the sensing element. This capacitance change is proportional to the angular velocity (XIA; YU; KONG, 2014).

When using gyroscopes to estimate orientation, a parameter that greatly affects the accuracy is the bias. Gyroscope bias is characterized by the average output when the device is sitting still, expressed in degrees per second (DPS) or radians per second. In practice, the orientation of

an IMU with respect to a reference inertial frame is defined by integrating the angular velocity over time. However, during the integration, small errors accumulate and result in signal drift, which is mainly due to the bias and its stability.

A typical linear sensor model for gyroscope is given by Equation 2.1,

$$\mathbf{y}_g = \boldsymbol{\omega} + \mathbf{b}_g + \mathbf{v}_g \quad (2.1)$$

where \mathbf{y}_g is the gyroscope output, $\boldsymbol{\omega}$ is the angular velocity and \mathbf{b}_g is the gyro bias, which is modeled as a random walk process. \mathbf{v}_g is the measurement noise, modeled as a zero-mean white Gaussian noise process with standard deviation σ_g , i.e., $\mathbf{v}_g \sim \mathcal{N}(0, \sigma_g^2)$.

2.2.2 Accelerometers

In its simplest representation, a single-axis MEMS accelerometer can be considered as a spring-mass system. When the mass is displaced, it means that the device is accelerated. MEMS accelerometers are based on different technologies, the most common are capacitive accelerometers which comprise two capacitors built by a mobile silicon mass between two fixed electrodes. Changes in the force lead the mobile mass to moves closer to one of the fixed electrodes, increasing the capacitance in one side and reducing it in the other. The difference in capacitance is proportional to the acceleration (MAENAKA, 2008).

Concerning error characteristics associated with the accelerometers, the bias is also quite critical. The bias of MEMS accelerometers, as that of gyroscopes, changes over time even at a constant temperature. Thus, the results by integrating the accelerometer measurements to estimate velocity and position suffer cumulative errors as well. Any bias introduced causes an error in position which grows quadratically with time (WOODMAN, 2007). In practice, accelerometers measure the local vertical axis by sensing the gravitational acceleration at rest. Thus, they are used to compensate the orientation drift at least on the vertical axis. However, during motion, accelerometers measure the sum of this gravitational acceleration, and the ac-

celeration that is associated with velocity changes.

An accelerometer can be modeled by Equation 2.2,

$$\mathbf{y}_a = \mathbf{M}^{-1}(q)(\mathbf{a}_N - \mathbf{g}_N) + \mathbf{b}_a + \mathbf{v}_a \quad (2.2)$$

where \mathbf{a}_N is the body acceleration and \mathbf{g}_N is the Earth's gravitational field, both expressed in the global (reference) coordinate system. \mathbf{b}_a is the accelerometer bias and \mathbf{v}_a is the measurement noise, modeled as a zero-mean white Gaussian noise process with standard deviation σ_a , $\mathbf{v}_a \sim \mathcal{N}(0, \sigma_a^2)$. $\mathbf{M}(q)$ is the rotation matrix calculated using the quaternion q as indicated in Section 2.3.3.

2.2.3 Magnetometers

MEMS magnetometers measure the local magnetic field, which consists of the earth magnetic field along with any induced field by a magnetic source in the environment. Most of magnetometers operate based on Hall effect, Lorentz force and Anisotropic Magneto Resistance (AMR) (LANGFELDER et al., 2013). Lorentz force magnetometers rely on the mechanical motion of the MEMS structure caused by a force being exerted on the current conductor in the magnetic field. Output signals from Hall effect sensors are proportional to the magnetic field density around the device. A typical magneto resistive sensor is a Wheatstone bridge of four AMR thin-film elements. The differential output voltage is function of both the supply voltage and the component of the local magnetic field along a given direction (BERTOLDI et al., 2005).

Currently, 3D Hall effect and magnetoresistive sensors are widely available because of manufacturing conveniences by integrating magnetoresistive material or hall plates in silicon (CAI et al., 2012). If two magnetometers are positioned orthogonally and both are tangential to the Earth's surface, the sensor can be used as a compass. Magnetometers may contribute to the stability in the horizontal plane avoiding heading drifts, however, magnetic disturbances highly

affect their performance (ROETENBERG et al., 2005).

A magnetometer can be modeled by Equation 2.3, where \mathbf{m}_N is the total magnetic field, which comprises the Earth magnetic field and any superimposed field, and \mathbf{b}_m is the bias. \mathbf{v}_m is the measurement noise, with standard deviation σ_m , i.e., $\mathbf{v}_m \sim \mathcal{N}(0, \sigma_m^2)$.

$$\mathbf{y}_m = \mathbf{M}^{-1}(q)(\mathbf{m}_N) + \mathbf{b}_m + \mathbf{v}_m \quad (2.3)$$

2.2.4 Intensity Variation-based POF Curvature Sensors

Polymeric Optical Fibers (POFs) are greatly flexible plastic waveguides built with dielectric materials. POF technology has the potential for economic bulk manufacturing. Also, they provide advantages over optical glass, being lightweight, low cost, highly flexible, ease of handling and with relatively high mechanical resistance. Their circular cross-section generally comprises of three layers: the core, cladding, and jacket, the last one a mechanical protective cover usually made of polyethylene. Most of the optical signal propagates through the core, as a result of surrounding the core with a cladding of a lower refractive index (ZUBIA; ARRUE, 2001).

In (ZUBIA; ARRUE, 2001), a complete explanation about loss mechanisms that contribute to signal attenuation is presented. Basically, these mechanisms are classified in intrinsic and extrinsic. For instance, within the intrinsic, are those due to vibration modes and within the extrinsic, are those due to micro and macrobends among others. Light intensity variation-based sensors measure the attenuation on a bending fiber. In sensing applications, both micro and macrobending attenuation are applied (BILRO et al., 2012).

The functional principle consists of putting the fiber to bending, what results in a variation of power output proportional to the curvature angle. In order to improve sensitivity to macrobending, commonly, the side polished technique is applied (BILRO et al., 2012). This technique consists of removing a section of the cladding by polishing the fiber laterally. This lateral section is called sensitive zone. Thus, under bending, more light rays escape through the sensitive

zone, where output signal presents attenuation if compared to the straight fiber. A recent research (LEAL-JUNIOR; FRIZERA; PONTES, 2018b) presented how the sensitive zone length, deep and surface roughness influence the sensor sensitivity, linearity and hysteresis.

Polymethyl methacrylate (PMMA) is the most common material used in the manufacturing of POF (BILRO et al., 2012). In this research, a PMMA-POF is used as a curvature sensor. The main disadvantages of this kind of sensors is the high attenuation when compared to glass fibers, so, consequently, they do not have long lengths. Moreover, polymers are viscoelastic materials, what leads to a non constant response under stress or strain. Thus, hysteresis and non-linearity are other drawbacks of this technology. Added to these limitations, there are errors due to undesired curvatures and variations of optical power.

A dynamic compensation technique based on the angular velocity of the sensor was proposed in our research group (LEAL-JUNIOR; FRIZERA; PONTES, 2018a). The authors state that it is difficult to obtain a single calibration equation that reduces both error and hysteresis in a wide range of angular velocities. Also, the technique performance is compromised in cases of hysteresis variability. Another technique was presented in (LEAL-JUNIOR et al., 2018c), which requires less number of tests and, consequently, is less time-consuming.

In our research, the latter compensation technique is used. Equation 2.4 shows the compensated definition for estimating the curvature angle α , after applying the Prony series with order 2 on the sensor response. Two expressions are required: one for flexion and other for extension motion. y_1 and y_2 are the weights of each exponential of the addition, τ_1 and τ_2 are time constants, $\frac{P}{P_0}$ is the power attenuation and c_0 is the linear offset.

$$\alpha = y_1 \cdot \exp\left(\tau_1 \left(\frac{P}{P_0}\right)\right) + y_2 \cdot \exp\left(\tau_2 \left(\frac{P}{P_0}\right)\right) + c_0 \quad (2.4)$$

It is worth to mention that the POF sensor in this configuration can only measure the angle in one plane. In this research, an application to estimate knee joint angle will be presented, however, similar configurations can be applied to assess other human joints.

2.3 Attitude and Motion Dynamics: Mathematical Representation

There are several mathematical representations of the object's attitude in three-dimensional space. We will review the three main mathematical constructs in the following subsections.

2.3.1 Euler Angles

Perhaps, the most common and intuitive way to represent rotations and orientations in three-dimensional space is Euler angles, three coordinate rotations in sequence can describe any rotation. Also, successive rotations cannot be made about the same axis. For notation, angles α , β and γ can be arranged in a three dimensional vector called the Euler angle vector \mathbf{u} , defined as shown in Equation 2.5.

$$\mathbf{u} = \begin{bmatrix} \alpha & \beta & \gamma \end{bmatrix}^T \quad (2.5)$$

There are twelve possible sequences that satisfy the constraint that no two consecutive numbers in a valid sequence may be equal (DIEBEL, 2006). For notational brevity, rotations around x-, y- and z-axis are numbered 1, 2 and 3, respectively. Thus, the set of possible sequences is shown in Equation 2.6.

$$(\mathbf{i}, \mathbf{j}, \mathbf{k}) \in \left\{ \begin{array}{ccc} (1, 2, 3) & (2, 3, 1) & (3, 1, 2) \\ (1, 3, 2) & (2, 1, 3) & (3, 2, 1) \\ (1, 2, 1) & (2, 3, 2) & (3, 1, 3) \\ (1, 3, 1) & (2, 1, 2) & (3, 2, 3) \end{array} \right\} \quad (2.6)$$

Due to the fact that an orientation can be obtained using different sequences of Euler angles, this representation is subject to ambiguities. Thus, a rotation sequence must be explicitly known. Also, for any set of Euler angles where the second rotation aligns the axes of the first and third rotations there is a singularity, what leads to loose one degree of freedom. This singularity is known as gimbal lock. Because of these drawbacks, we chose not to use this representation through this research.

2.3.2 Direction Cosine Matrices (DCM)

A rotation matrix is an entity that when multiplied by a vector, rotates such vector without changing its length. The special orthogonal group of all rotation matrices is denoted by $SO(3)$ (DIEBEL, 2006). Thus, a proper matrix \mathbf{M} has the properties as shown in Equation 2.7.

$$\det(\mathbf{M}) = 1, \quad \mathbf{M}^{-1} = \mathbf{M}^T \quad (2.7)$$

Consider an orthogonal reference frame (or global frame), $O - xyz$, where x , y and z are the unit vectors of the frame axes. Also, consider an orthogonal frame, called local, attached to a body $O - x'y'z'$, where x' , y' and z' are the unit vectors of the frame axes. Also, consider that both frames have the same origin. The rotation matrix that express the orientation of the local frame with respect to the reference frame is shown in Equation 2.8.

$$\mathbf{M} = \begin{bmatrix} x'_x & y'_x & z'_x \\ x'_y & y'_y & z'_y \\ x'_z & y'_z & z'_z \end{bmatrix} = \begin{bmatrix} \cos(\theta_{x',x}) & \cos(\theta_{y',x}) & \cos(\theta_{z',x}) \\ \cos(\theta_{x',y}) & \cos(\theta_{y',y}) & \cos(\theta_{z',y}) \\ \cos(\theta_{x',z}) & \cos(\theta_{y',z}) & \cos(\theta_{z',z}) \end{bmatrix} \quad (2.8)$$

The right side of the expression is called Direction Cosine Matrix (DCM). Another important construction of the rotation matrix is shown in Equation 2.9. This expression describes any rotation matrix defined by angle θ about a vector \mathbf{n} (HANSON, 2005), where n_1 , n_2 and n_3 are the vector \mathbf{n} 's elements, c and s denote the $\cos(\theta)$ and $\sin(\theta)$, respectively.

$$\mathbf{M}(\theta, \mathbf{n}) = \begin{bmatrix} c + (n_1)^2(1 - c) & n_1n_2(1 - c) - sn_3 & n_1n_3(1 - c) + sn_2 \\ n_2n_1(1 - c) + sn_3 & c + (n_2)^2(1 - c) & n_2n_3(1 - c) - sn_1 \\ n_3n_1(1 - c) - sn_2 & n_3n_2(1 - c) + sn_1 & c + (n_3)^2(1 - c) \end{bmatrix} \quad (2.9)$$

2.3.3 Quaternions

Rotations and orientations in a three dimensional space can be represented using quaternions. Quaternions are four-element vectors as shown in Equation 2.10, with the first element as the

scalar part and the remaining three as the vector part. The non-commutative multiplication rule is assigned to these vectors (HANSON, 2005). This representation has some advantages when compared to Euler angles and DCMs, such as not to be rotation-dependent, not presenting singularities or suffering from gimbal lock. Also, quaternion representation is more compressed than DCMs, which allows computationally more efficient transmissions and calculations. However, quaternions have not a clear physical meaning and are not very intuitive, for this reason, sometimes it is difficult to apply them (DIEBEL, 2006).

$$\mathbf{q} = \begin{bmatrix} q_0 & q_1 & q_2 & q_3 \end{bmatrix}^T = q_0 + q_1\mathbf{i} + q_2\mathbf{j} + q_3\mathbf{k} \quad (2.10)$$

The algebra of quaternions is often denoted by \mathbf{H} or \mathbb{H} . Unlike multiplication of real or complex numbers, multiplication of quaternions is not commutative. Quaternion multiplication (also called Hamilton product) is defined as shown in Equation 2.11 (HANSON, 2005).

$$\mathbf{p} \otimes \mathbf{q} = (p_0, p_1, p_2, p_3) \otimes (q_0, q_1, q_2, q_3), \quad (2.11a)$$

$$\mathbf{p} \otimes \mathbf{q} = \begin{bmatrix} p_0q_0 - p_1q_1 - p_2q_2 - p_3q_3 \\ p_1q_0 + p_0q_1 + p_2q_3 - p_3q_2 \\ p_2q_0 + p_0q_2 + p_3q_1 - p_1q_3 \\ p_3q_0 + p_0q_3 + p_1q_2 - p_2q_1 \end{bmatrix}, \quad (2.11b)$$

$$\mathbf{p} \otimes \mathbf{q} = (p_0q_0 - \mathbf{p} \cdot \mathbf{q}, p_0\mathbf{q} + q_0\mathbf{p} + \mathbf{p} \times \mathbf{q}), \quad (2.11c)$$

Only quaternions of unit length are used to represent orientations and rotations. These obey the proprieties expressed in Equation 2.12.

$$\mathbf{q} \cdot \mathbf{q} = (q_0)^2 + (q_1)^2 + (q_2)^2 + (q_3)^2 = (q_0)^2 + \mathbf{q} \cdot \mathbf{q} = 1, \quad (2.12a)$$

$$\mathbf{q}^{-1} = \mathbf{q}^*, \quad (2.12b)$$

According to the Euler's rotation theorem, any rotation can be described using a unit-vector \mathbf{n} (called also Euler axis) and an angle θ , which describes a rotation around the mentioned

vector (HANSON, 2005). Its corresponding quaternion is shown in Equation 2.13.

$$q(\theta, \mathbf{n}) = \left(\cos\left(\frac{\theta}{2}\right), \mathbf{n} \sin\left(\frac{\theta}{2}\right) \right) \quad (2.13)$$

Let $\mathbf{p}_N = \begin{bmatrix} p_x & p_y & p_z \end{bmatrix}^T$ be an arbitrary vector defined in a reference coordinate system XYZ , which results in a new vector $\mathbf{p}'_N = \begin{bmatrix} p'_x & p'_y & p'_z \end{bmatrix}^T$ after a rotation. This operation is expressed using quaternion as described by Equation 2.14. Also, Equation 2.14 can be rewritten in the matrix form as shown in Equation 2.15, where $\mathbf{M}(q)$ is the rotation matrix, which is function of the quaternion q and can be expressed by Equation 2.16.

$$\mathbf{p}'_N = q \otimes \mathbf{p}_N \otimes q^{-1} \quad (2.14)$$

$$\mathbf{p}'_N = \mathbf{M}(q)\mathbf{p}_N \quad (2.15)$$

$$\mathbf{M}(q) = 2 \begin{bmatrix} q_0^2 + q_1^2 + \frac{1}{2} & q_1q_2 - q_0q_3 & q_1q_3 + q_0q_2 \\ q_1q_2 + q_0q_3 & q_0^2 + q_2^2 - \frac{1}{2} & q_2q_3 - q_0q_1 \\ q_1q_3 - q_0q_2 & q_2q_3 + q_0q_1 & q_0^2 + q_3^2 - \frac{1}{2} \end{bmatrix} \quad (2.16)$$

The time derivative of the unit quaternion is the vector of quaternion rates. The rate of change \dot{q} is related to the angular velocity $\boldsymbol{\omega}$ as shown in Equation 2.17, where $\boldsymbol{\omega} = \begin{bmatrix} \omega_1 & \omega_2 & \omega_3 \end{bmatrix}^T$ is the instantaneous angular velocity expressed in the body frame. The matrix-form expression equivalent is shown in Equation 2.18, where $[\boldsymbol{\omega} \times]$ is outer product tensor of the vector $\boldsymbol{\omega}$, which is defined by Equation 2.19.

$$\dot{q} = \frac{1}{2}q \otimes \boldsymbol{\omega}, \quad (2.17)$$

$$\dot{q} = \frac{1}{2}\Omega(\boldsymbol{\omega})q, \quad \Omega(\boldsymbol{\omega}) = \begin{bmatrix} 0 & -\boldsymbol{\omega}^T \\ \boldsymbol{\omega} & -[\boldsymbol{\omega} \times] \end{bmatrix}, \quad (2.18)$$

$$[\boldsymbol{\omega} \times] = \begin{bmatrix} 0 & -\omega_3 & \omega_2 \\ \omega_3 & 0 & -\omega_1 \\ -\omega_2 & \omega_1 & 0 \end{bmatrix}, \quad (2.19)$$

2.4 Human Gait Multi-sensor Fusion Methods

Assessment of human's performance based on functional activity monitoring is of great interest in pervasive healthcare (MARSCHOLLEK et al., 2012). Currently, IMUs are very used for motion monitoring, although these technologies have some limitations as previously mentioned. For overcoming the sensing device limitations, researchers follow the strategy of combining data provided by multiple sensors through sensor fusion approaches.

The use of inertial sensors to estimate the attitude of an object, i.e., position and orientation, is very common in robotics, automotive and aerial vehicles industry, navigation applications and aerospace research. Many methods have been proposed with regards to multi-sensor fusion in these areas. In this section, we briefly outline some of these approaches that have been used specifically for gait analysis.

2.4.1 Variations of Non-linear Kalman Filters

Kalman Filter (KF) and its non-linear variation, Extended Kalman Filter (EKF), are the most widespread filter used to estimate orientation in IMU-based gait analysis, see e.g. (NOGUEIRA et al., 2017; BAGHDADI; CAVUOTO; CRASSIDIS, 2018; BERGAMINI et al., 2014; YUAN et al., 2019; SABATINI, 2011). Unscented Kalman Filter (UKF), other of its variations, seems to be less used (KANG; JANG; PARK, 2019; OKITA; SOMMER, 2012), maybe because EKF has demonstrated to be greatly (about $10\times$) more computationally efficient than UKF (WAEGLI; SKALLOUD, 2009; GROSS et al., 2012; RHUDY et al., 2013).

KF addresses the multi-sensor fusion with a probabilistic approach. Knowledge about the system dynamics (i.e. the model) is needed in order to correctly estimate the internal states. The relation between the measurements (or observations) and the system states (i.e. the measurement model) is also required. Since the state representation is described as a stochastic model, additive noise with known covariance matrix, for both process and measurement models are

also needed. Initial state values, process, and measurement noise covariance are critical parameters for the correct filter performance (SCHNEIDER; GEORGAKIS, 2013). EKF handles the nonlinearity by using an analytical linearization around the best current estimation, which is done using Jacobian matrices (SABATINI, 2011).

EKF is described for nonlinear systems with additive noise by Equation 2.20, where \mathbf{w}_{k-1} and \mathbf{v}_k are the additive noises, modeled as a zero-mean white Gaussian noise process with known covariance matrices \mathbf{Q}_{k-1} and \mathbf{R}_k , respectively.

$$\begin{aligned}\mathbf{x}_k &= f_{k-1}(\mathbf{x}_{k-1}) + \mathbf{w}_{k-1} \\ \mathbf{z}_k &= h_k(\mathbf{x}_k) + \mathbf{v}_k\end{aligned}\tag{2.20}$$

The local linearization requires the computation of the Jacobians of $f_{k-1}(\mathbf{x}_{k-1})$ (i.e. dynamic model) and $h_k(\mathbf{x}_k)$ (i.e. measurement model) with current predicted states (SABATINI, 2011).

The Multiplicative Extended Kalman Filter (MEKF) is an indirect KF frequently used in aeronautics (MARKLEY, 2003), and recently applied for motion analysis (GHOBADI; ESFAHANI, 2017a; KORTIER et al., 2015). Basically, the unconstrained and non-singular error in MEKF (δq) is defined as the multiplication of the (actual best) estimated quaternion inverse (\hat{q}^{-1}) and the true quaternion (q) as shown in Equation 2.21, where δq is parametrized by a three-element vector \mathbf{a} . The resulting filter obeys the quaternion norm constraint (MARKLEY, 2003).

$$\delta q(\mathbf{a}) = \hat{q}^{-1} \otimes q\tag{2.21}$$

2.4.2 Other Fusion Methods

Methods with open-access code presented by Madgwick et al. (2011) and Mahony et al. (2008) have been used for gait analysis, see e.g. (KIM; KIM; KIM, 2015; TO; MAHFOUZ, 2013). These methods are limited to solve the orientation problem for each IMU and do not take into account joint kinematics. Other filters with similar approaches are complementary (BERGAMINI et al., 2014) and particle filters (PELTOLA; HILL; MOORE, 2016). Alternatively, filters based

on optimization (KOK; HOL; SCHÖN, 2014) can also include information from biomechanical constraints, however, they are computationally expensive.

2.5 Preliminary Conclusions

In this chapter, a description about the main concepts of human gait and some parameters for its analysis were presented. Such parameters are of great importance in clinical scenarios and can be useful from diagnosis to assessing recovery process. In this Ph.D. thesis, we analyzed the joint angles in different approaches.

Moreover, a variety of methods to align IMUs coordinate system to the anatomically-defined have been presented in the literature, however, most of them require additional tools or performing movements which can be difficult for people with some motor disability. Thus, an alignment method based on fast and easy sensor placement, without the need of predefined-motion is addressed in this Ph.D. thesis.

In addition, the most common IMUs models were introduced, that along with a recent POF curvature sensor model, allow designing a novel multi-sensor fusion method. So far, several methods in the literature for gait analysis using IMUs and polymer optical fiber (POF) sensors were presented. Regarding the IMU-based joint angle estimation methods, few researches use aiding sensors other than magnetometers, such as electrogoniometers, aiming to improve the accuracy of the systems in different environments. This has determined the fact of addressing a novel IMU-POF sensor fusion system in this Ph.D. thesis to assess knee joint angle in ambulatory applications.

Chapter 3

An IMU-to-Body Alignment Method Applied to Human Gait Analysis¹

A fundamental problem of the IMU-based gait analysis is how to define an appropriate measurement protocol and provide a sensor-to-body calibration procedure (SEEL; RAISCH; SCHAUER, 2014). Because IMUs' local frames are not aligned with anatomically defined frames, different approaches in the literature have presented different methods to determine the sensor frame's orientation with respect to the body segment frame (FAVRE et al., 2009; CUTTI et al., 2010; PALERMO et al., 2014; O'DONOVAN et al., 2007). However, those approaches suffer from some limitations. One main problem with algorithms based only on data from accelerometers and gyroscopes (LUINGE; VELTINK; BATEN, 2007; FAVRE et al., 2009; KAVANAGH et al., 2006; TADANO; TAKEDA; MIYAGAWA, 2013) is the difficulty to define a common reference frame and, consequently, measure 3D angles. To accurately measure 3D angles, a second global reference axis is necessary along with the gravity vector. This second reference axis is commonly the magnetic field vector, measured by sensor units that include magnetometers. Since heading drift remains a problem within systems that involve only accelerometers and gyroscopes, the anatomical calibration techniques that use such systems rely on predefined user movements

¹This chapter is mainly based on the following manuscript:
L. Vargas-Valencia, A. Elias, E. Rocon, T. Bastos-Filho, and A. Frizera (2016). **An IMU-to-body alignment method applied to human gait analysis**. *Sensors*, 16(12), 2090.

to define the axis of joint motion (LUINGE; VELTINK; BATEN, 2007), or use supplementary devices such as cameras (TADANO; TAKEDA; MIYAGAWA, 2013), anatomical landmark pointers (PICERNO; CEREATTI; CAPPOZZO, 2008) or exoskeleton harnesses (FAVRE et al., 2009). The need for these additional tools also increases the experiment duration and requires experienced personnel, which may be impractical in daily clinical routine.

Other works are based on performing complex movements while keeping some specific postures (FAVRE et al., 2009; CUTTI et al., 2010; O'DONOVAN et al., 2007), or maintaining the same orientation or joint angle between two postures (PALERMO et al., 2014; TADANO; TAKEDA; MIYAGAWA, 2013), which may not be simple tasks to be performed by subjects with motor disabilities. Even for subjects without disability, performing these tasks requires the assistance of examiners. Hence, these mentioned methods may be more prone to calibration errors.

The objective of this chapter is to present a novel calibration procedure as a method to align IMU sensors to body segments, which compared to the aforementioned methods, is based on fast and simple sensor placement procedures, with no need for movements performed by the user nor any additional tools. Initially, we propose a validation protocol of the procedure using a simplified rigid-body joint that comprises two semi-spheres. A universal goniometer is used as the gold standard measure in order to ensure controlled angular movements. Additionally, we present an application of the method on five able-bodied subjects performing a gait test. The kinematic data of the lower limb joints is presented descriptively.

This chapter is organized as follows. Section 3.1 describes the proposed IMU-to-body alignment method that includes the calibration algorithm, definition of technical-anatomical frames and calculation of joint angles. Then, in Section 3.2 we present the motion acquisition system and the validation protocol using the simplified joint, along with an evaluation procedure to quantify the accuracy and repeatability of the technique. Following, a sensor placement protocol and an estimation of kinematic data on subjects without functional disability are introduced in Section 3.3. Finally, we provide the results and discussion of the experiments that validate

the proposed method (Section 3.4), followed by preliminary conclusions (Section 3.5).

3.1 IMU-to-Body Alignment Method

To estimate the lower limb joint angles, it is necessary to measure the orientation of two adjacent body segments forming the joint. We propose a method to estimate hip, knee and ankle joint angles. To simplify the mathematical explanation, here we only present the data for the right leg, although the same concept may be obviously applied to both legs. In this method, four IMUs sensors are used: one is placed on the pelvis (body segment named *PV*), one on the right thigh (*TH*), one on the right shank (*SH*), and another on the right foot (*FT*). Each body segment also has an associated coordinate system (*B*), which is called, in this work, a technical-anatomical frame. Note that the technical-anatomical frame is an estimate and it is also different from the anatomical bone-embedded frame as defined by the International Society of Biomechanics (ISB) recommendations (GROOD; SUNTAY, 1983; WU et al., 2002). The reason is that the axes of body segments' Cartesian coordinate systems, within ISB recommendations, are defined based on bony landmarks that are palpable or identifiable from X-rays.

3.1.1 Calibration Algorithm and Definition of Technical-Anatomical Frames

During five seconds of static acquisition (initial upright posture), the orientation data is used to define the sensor-to-body alignment. The first stage consists of correcting the sensor frame placed on the pelvis (called *IMU – PV* coordinate system). This correction procedure aims to align the x-axis of *IMU – PV* with the gravity. Let ${}^G\mathbf{q}_{IMU-PV_0}$ be the quaternion of the IMU placed on the pelvis, in the initial posture computed by averaging the orientation data (as in (PRENTICE, 1986)) acquired over 5 s interval, where *G* is the global reference frame. Since the orientation data is obtained in quaternion format, the operations to align the sensor quaternion ${}^G\mathbf{q}_{IMU-PV_0}$ with the gravity are performed as follows:

1. Obtain x-axis (\mathbf{x}_{IMU-PV_0}) of the coordinate system referred to the IMU orientation measured by the quaternion ${}^G\mathbf{q}_{IMU-PV_0}$ associated with the initial posture, and using Equation 3.1 to convert from unit quaternions to direction cosine matrix, \mathbf{x}_{IMU-PV_0} defined as shown in Equation 3.2:

$$M(\mathbf{q}) = \begin{bmatrix} q_0^2 + q_1^2 - q_2^2 - q_3^2 & 2(q_1q_2 - q_0q_3) & 2(q_1q_3 + q_0q_2) \\ 2(q_1q_2 + q_0q_3) & q_0^2 - q_1^2 + q_2^2 - q_3^2 & 2(q_2q_3 - q_0q_1) \\ 2(q_1q_3 - q_0q_2) & 2(q_2q_3 + q_0q_1) & q_0^2 - q_1^2 - q_2^2 + q_3^2 \end{bmatrix}, \quad (3.1)$$

$$\mathbf{x}_{IMU-PV_0} = M({}^G\mathbf{q}_{IMU-PV_0}) \mathbf{i}, \quad (3.2)$$

where \mathbf{i} is the unit vector in direction of the x-axis.

2. Define the angle θ between \mathbf{x}_{IMU-PV_0} and the gravity vector \mathbf{ZG} . The angle θ is calculated using Equation 3.3:

$$\theta = \arccos 2(q_1q_3 - q_0q_2), \quad (3.3)$$

where q_0, q_1, q_2 and q_3 are the components of the quaternion ${}^G\mathbf{q}_{IMU-PV_0}$.

3. Define the vector \mathbf{n}_1 orthonormal to the mentioned vectors \mathbf{x}_{IMU-PV_0} and \mathbf{ZG} . Around this vector a rotation θ is made according to Euler's rotation theorem. The orthonormal and unit vector \mathbf{n}_1 is defined as shown in Equation 3.4. The correction quaternion $\mathbf{q}_C(\theta, \mathbf{n}_1)$ is calculated using Equation 3.5:

$$\mathbf{n}_1 = \begin{bmatrix} 2(q_1q_2 + q_0q_3) & q_2^2 + q_3^2 - q_0^2 - q_1^2 & 0 \end{bmatrix}^T, \quad (3.4a)$$

$$\mathbf{n}_1 = \frac{\mathbf{n}_1}{\|\mathbf{n}_1\|_2}, \quad (3.4b)$$

$$\mathbf{q}_C(\theta, \mathbf{n}_1) = \left(\cos \frac{\theta}{2}, \mathbf{n}_1 \sin \frac{\theta}{2} \right), \quad (3.5)$$

The technical-anatomical frame of the pelvis ($B - PV_0$) calculated with respect to the global frame (G), during the initial posture, is defined as shown in Equation 3.6:

$${}^G\mathbf{q}_{B-PV_0} = \mathbf{q}_C(\theta, \mathbf{n}_1) \otimes {}^G\mathbf{q}_{IMU-PV_0}, \quad (3.6)$$

Other initial technical-anatomical frames (B) using quaternions are defined during the calibration procedure as shown in Table 3.1. Once the initial technical-anatomical quaternions are defined, the sensor-to-body orientation ${}^B\mathbf{q}_{IMU-B}$ is determined for each sensor using Equation 3.7. Please note that subscript 0 was omitted, because the sensor-to-body orientation is supposed to be constant once each sensor does not change its orientation with respect to the body segment.

$${}^{B-X}\mathbf{q}_{IMU-X} = {}^G\mathbf{q}_{B-X_0}^* \otimes {}^G\mathbf{q}_{IMU-X_0}, \quad (3.7)$$

where X denotes the body segment, namely PV , TH , SH and FT , and $*$ denotes the complex conjugate of the quaternion. Once we have the relative orientation of the sensor to the body segment, the orientation of each segment at any instant of time can be determined, using Equation 3.8, as ${}^G\mathbf{q}_{B-PV}$, ${}^G\mathbf{q}_{B-TH}$, ${}^G\mathbf{q}_{B-SH}$ and ${}^G\mathbf{q}_{B-FT}$, for the pelvis, thigh, shank and foot, respectively.

$${}^G\mathbf{q}_{B-X} = {}^G\mathbf{q}_{IMU-X} \otimes {}^{B-X}\mathbf{q}_{IMU-X}^* \quad (3.8)$$

Then, the hip, knee and ankle joint rotations are defined by relating the orientation of the distal body segment with respect to the proximal body segment. The technical-anatomical frames are presented in Figure 3.1 for each body segment. During the initial posture the joint angles are assumed to be zero, since the corresponding body segments are aligned. The proposed algorithm is also conceived in such a way that the IMUs can be placed in any arbitrary position

Table 3.1: Definition of technical-anatomical quaternions obtained during calibration posture (straight upright posture).

Segment	Initial Quaternion Definition
Pelvis (PV)	${}^G\mathbf{q}_{B-PV_0}$
Thigh (TH)	${}^G\mathbf{q}_{B-TH_0} = {}^G\mathbf{q}_{B-PV_0} \otimes \mathbf{q}_{\text{ROT}}(90^\circ, \mathbf{i})^1$
Shank (SH)	${}^G\mathbf{q}_{B-SH_0} = {}^G\mathbf{q}_{B-TH_0}$
Foot (FT)	${}^G\mathbf{q}_{B-FT_0} = {}^G\mathbf{q}_{B-PV_0} \otimes \mathbf{q}_{\text{ROT}}(180^\circ, \mathbf{n}_2)^2$

¹ $\mathbf{i} = [1 \ 0 \ 0]^T$, ² $\mathbf{n}_2 = [\sqrt{2} \ 0 \ \sqrt{2}]^T$. Let $\mathbf{q}_{\text{ROT}}(\theta, \mathbf{n})$ be the quaternion of rotation calculated using Equation 3.5 for $\theta = 90^\circ$ or 180° and $\mathbf{n} = \mathbf{i}$ or \mathbf{n}_2 . B refers to body-frame and G refers to global frame.

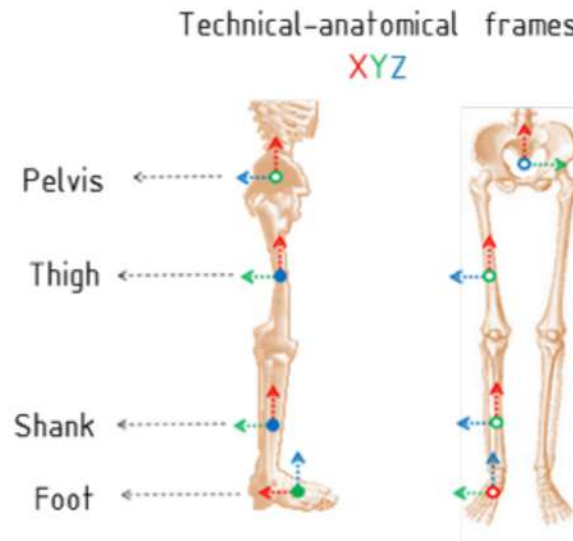


Figure 3.1: Technical-anatomical frames (B) of the pelvis, thigh, shank and foot. Axes X, Y and Z in color red, green and blue, respectively.

on the body segments. This means that the user does not have to be concerned about placing the IMUs in an exact position. The algorithm to extract the joint angles is presented in detail in the next section. A flowchart that summarizes the IMU-to-Body alignment method is presented in Appendix A.1.

3.1.2 Joint Angles Calculation

The last general reporting standard for joint kinematics based on Joint Coordinate System (JCS) was presented by the International Society of Biomechanics (ISB) (WU et al., 2002). The concept of JCS was first presented by Grood and Suntay (1983) only for the knee joint, but this approach has been adopted to define the kinematics of other human joints. This concept uses the description of Cartesian coordinate systems and vector algebra to define the knee joint. In this work, we present the equivalent algebra using quaternions to define hip, knee and ankle joints. Following the method proposed by Grood and Suntay (1983), we compute the body fixed axes and the reference axes of the JCS in Table 3.2 according to the frames shown in Figure 3.1. Table 3.3 summarizes the sign convention used on defining the clinical rotations, where flexion, abduction and internal rotation movements are positives. Now, let ${}^G\mathbf{q}_{B-PV}$,

Table 3.2: Body fixed, floating and references axes of each joint.

Joint	Joint Coordinate System	Body Fixed and Floating Axes	References Axes
HIP ¹	Pelvis axis (flexion-extension)	$\mathbf{e}_1 = -\mathbf{y}_{PV}$	$\mathbf{e}_1^r = -\mathbf{z}_{PV}$
	Femoral axis (internal-external rotation)	$\mathbf{e}_3 = \mathbf{x}_{TH}$	$\mathbf{e}_3^r = -\mathbf{y}_{TH}$
	Floating axis (abduction-adduction)	$\mathbf{e}_2 = \frac{\mathbf{x}_{TH} \times (-\mathbf{y}_{PV})}{ \mathbf{x}_{TH} \times (-\mathbf{y}_{PV}) }$	
KNEE ²	Femoral axis (flexion-extension)	$\mathbf{e}_1 = -\mathbf{z}_{TH}$	$\mathbf{e}_1^r = -\mathbf{y}_{TH}$
	Tibial axis (internal-external rotation)	$\mathbf{e}_3 = \mathbf{x}_{SH}$	$\mathbf{e}_3^r = -\mathbf{y}_{SH}$
	Floating axis (abduction-adduction)	$\mathbf{e}_2 = \frac{\mathbf{x}_{SH} \times \mathbf{z}_{TH}}{ \mathbf{x}_{SH} \times \mathbf{z}_{TH} }$	
ANKLE ¹	Tibial axis (dorsiflexion-plantar-flexion)	$\mathbf{e}_1 = \mathbf{z}_{SH}$	$\mathbf{e}_1^r = -\mathbf{y}_{SH}$
	Calcaneal (internal-external rotation)	$\mathbf{e}_3 = \mathbf{z}_{FT}$	$\mathbf{e}_3^r = -\mathbf{x}_{FT}$
	Floating axis (inversion-eversion)	$\mathbf{e}_2 = \frac{\mathbf{z}_{FT} \times \mathbf{z}_{SH}}{ \mathbf{z}_{FT} \times \mathbf{z}_{SH} }$	

¹ JCS proposed by Wu et al. (2002) and ² JCS proposed by Grood and Suntay (1983). *PV* pelvis, *TH* thigh, *SH* shank, *FT* foot.

Table 3.3: Rotations of the hip, knee and ankle joint of the right leg.

Joint	Flexion-Extension	Abduction-Adduction	Internal-External Rot
HIP	$\alpha = \text{asin}(e_{2-H} \cdot x_{PV})$	$\beta = \text{acos}(-y_{PV} \cdot x_{TH}) - \frac{\pi}{2}$	$\gamma = \text{asin}(e_{2-H} \cdot z_{TH})$
KNEE	$\alpha = -\text{asin}(e_{2-K} \cdot x_{TH})$	$\beta = \text{acos}(z_{TH} \cdot x_{SH}) - \frac{\pi}{2}$	$\gamma = \text{asin}(e_{2-K} \cdot z_{SH})$
ANKLE ¹	$\alpha = \text{asin}(e_{2-A} \cdot x_{SH})$	$\beta = \text{acos}(z_{SH} \cdot z_{FT}) - \frac{\pi}{2}$	

¹ Ankle rotations are dorsiflexion-plantar flexion and inversion-eversion. α , β and γ are the joint angles on sagittal, frontal and transverse planes, respectively. *PV* pelvis, *TH* thigh, *SH* shank, *FT* foot.

${}^G\mathbf{q}_{B-TH}$, ${}^G\mathbf{q}_{B-SH}$, and ${}^G\mathbf{q}_{B-FT}$, be the orientation quaternions that represent the frames fixed in each bone. Each body fixed, floating and reference axes, in Table 3.2, is computed as function of quaternions. Let \mathbf{e}_{2-H} , \mathbf{e}_{2-K} , and \mathbf{e}_{2-A} , be the floating axis of the hip, knee and ankle joint, respectively. The corresponding equations are shown in Equation 3.9, where $|\cdot|$ indicates that the vector must be normalized, and \mathbf{i} , \mathbf{j} , and \mathbf{k} denote the unit vectors in direction of the x, y and z axes, respectively. Then, the equivalent equations in quaternions for calculating the joint

rotations are presented in Table 3.4.

$$\mathbf{e}_{2-H} = \frac{(M({}^G\mathbf{q}_{B-TH})\mathbf{i}) \times (-M({}^G\mathbf{q}_{B-PV})\mathbf{j})}{|\cdot|}, \quad (3.9a)$$

$$\mathbf{e}_{2-K} = \frac{(M({}^G\mathbf{q}_{B-SH})\mathbf{i}) \times (-M({}^G\mathbf{q}_{B-TH})\mathbf{k})}{|\cdot|}, \quad (3.9b)$$

$$\mathbf{e}_{2-A} = \frac{(M({}^G\mathbf{q}_{B-FT})\mathbf{k}) \times (-M({}^G\mathbf{q}_{B-SH})\mathbf{k})}{|\cdot|}, \quad (3.9c)$$

Table 3.4: Joint rotations as functions of quaternions.

Joint	Angles
HIP	$\alpha = \text{asin}(\mathbf{e}_{2-H} \cdot M({}^G\mathbf{q}_{B-PV})\mathbf{i})$
	$\beta = \text{acos}(-M({}^G\mathbf{q}_{B-PV})\mathbf{j} \cdot M({}^G\mathbf{q}_{B-TH})\mathbf{i}) - \frac{\pi}{2}$
	$\gamma = \text{asin}(\mathbf{e}_{2-H} \cdot M({}^G\mathbf{q}_{B-TH})\mathbf{k})$
KNEE	$\alpha = -\text{asin}(\mathbf{e}_{2-K} \cdot M({}^G\mathbf{q}_{B-TH})\mathbf{i})$
	$\beta = \text{acos}(M({}^G\mathbf{q}_{B-TH})\mathbf{k} \cdot M({}^G\mathbf{q}_{B-SH})\mathbf{i})$
	$\gamma = \text{asin}(\mathbf{e}_{2-K} \cdot M({}^G\mathbf{q}_{B-SH})\mathbf{k})$
ANKLE	$\alpha = \text{asin}(\mathbf{e}_{2-A} \cdot M({}^G\mathbf{q}_{B-SH})\mathbf{i})$
	$\beta = \text{acos}(M({}^G\mathbf{q}_{B-SH})\mathbf{k} \cdot M({}^G\mathbf{q}_{B-FT})\mathbf{k})$

α , β and γ are the joint angles on sagittal, frontal and transverse planes, respectively. \mathbf{e}_{2-H} , \mathbf{e}_{2-K} and \mathbf{e}_{2-A} are the floating axes of the hip, knee and ankle, respectively. $M({}^G\mathbf{q}_{B-X})$ is the equivalent direction-cosine matrix of the ${}^G\mathbf{q}_{B-X}$ quaternion of X body-segment. Body segments: PV pelvis, TH thigh, SH shank, FT foot.

3.2 Validation Protocol of Calibration Procedure Using a Simplified Rigid-Body Joint

3.2.1 Motion Acquisition System

The motion capture system Tech MCS (Technaid, Madrid, Spain) was used in the experimental procedure. The device was connected via Bluetooth to a laptop. In this study four Tech-IMU V 3.0 sensors were used to obtain orientation data in real-time. Each IMU integrates three different types of three-axial sensors: accelerometers, gyroscopes and magnetometers. Data were acquired using Tech MCS Studio software, which provides orientation (based on Kalman filtering) in quaternion format at 50 Hz. MATLAB software (The MathWorks Inc., Natick, MA, USA) was used to analyze and process the orientation data.

3.2.2 Experimental Procedure

A set-up (Figure 3.2a) was built with two semi-spheres and the joint angles were measured by an expert physiotherapist using a universal goniometer (360°, 20 cm clear plastic goniometer). Each semi-sphere is used to represent body segments, and the universal goniometer is used to represent an articulation with one degree of freedom.

Using the universal goniometer as reference for measurements, angular movements can be performed in a controlled approach. The rigid semi-spheres are named as S1 and S2 (upper and bottom respectively, see Figure 3.2a). The joint represented by the goniometer is denoted as J . Rotations from 0° to $\pm 80^\circ$ with steps of $\pm 20^\circ$ about z-axis of J were performed. These angles correspond to rotations of S2 with respect to S1, which was kept static. The rotation range reaches (or even exceeds) a complete range of motion in lower limbs during walking.

One sensor (IMU 1) was placed on the goniometer, and the three others (IMUs 2, 3 and 4) were placed on two semi-spheres. The IMU 1 is used as the reference, in the same way as the

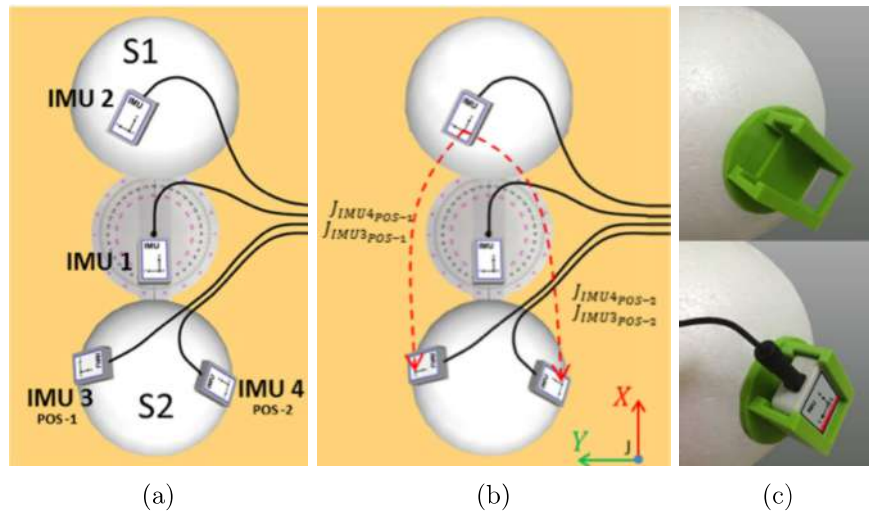


Figure 3.2: Scheme of a simplified joint comprising two semi-spheres. (a) Adjacent segments $S1$ and $S2$, and a universal goniometer (a controlled joint J); (b) representations of the joint J and (c) rigid plastic piece (green) to fit the sensors in a fixed position on the semi-sphere.

sensor placed on the pelvis for the experiments with human subjects. This sensor also remained static. For each semi-sphere, technical frames were defined as described in Section 3.1.1 and the equations applied are analogous to those for calculating knee joint angles as described in Section 3.1.2. Observe that the segment $S2$ has two sensors (IMUs 3 and 4), that means the technical frame of $S2$ can be determined using both sensors. Also, these sensors were fixed to the semi-sphere using a rigid plastic pieces manufactured using the 3D printer model S3 (Sethi3D, Brazil) as shown in Figure 3.2c, which were glued fitting on the semi-sphere surface. These pieces ensure that the sensors have the same posture when they are exchanged.

The proposed procedure is conceived in such way that there is no concern about placing the sensors in an exact position. Moreover, considering that significant differences may be presented between any pair of IMU sensors, this setup allows the analysis of two different approaches when estimating the joint angles: (a) using the same sensor (IMU 3 or IMU 4) in different postures; and (b) using different sensors in the same posture.

The orientation of each semi-sphere frame at any instant of time can be determined as ${}^G\mathbf{q}_{S1}$, ${}^G\mathbf{q}_{S2_{IMU3}}$ and ${}^G\mathbf{q}_{S2_{IMU4}}$. The joint J (Figure 3.2b) can be represented in a total of four different ways, as shown in Table 3.5. A simulation run in MATLAB under ideal conditions (IMU

Table 3.5: Representations of the J joint formed by S1 and S2 segments.

Joint	S1	S2	Posture
\mathbf{J}_1	IMU 2	IMU 3	POS-1
\mathbf{J}_2	IMU 2	IMU 3	POS-2
\mathbf{J}_3	IMU 2	IMU 4	POS-1
\mathbf{J}_4	IMU 2	IMU 4	POS-2

POS-1 and POS-2 are the S2 positions on the left and right side of the semi-sphere, respectively, as shown in Fig 3.2a

misalignment error, bias and noise equal to zero) is also presented to demonstrate that, theoretically, different orientations of IMUs do not affect the angle measures using the proposed method (assuming that IMUs 3 and 4 are ideally equal devices). In simulation, the initial orientation of the sensors was set to the initial values obtained during experimental validation.

3.2.3 Data Reduction and Statistical Analysis

A 20 min warm-up of the IMU sensors was carried out before the experiments, in an attempt to stabilize the gyroscope measurements (PICERNO; CEREATTI; CAPPOZZO, 2011). After each rotation, the semi-sphere S2 was kept stationary approximately for 15 s. Only the last 10 s of collected data, for each orientation, were used. Quaternion for each rotation is resulted from averaging quaternion data over the 10 s intervals. Once data were reduced for each sensor and orientation, the IMU-to-body alignment method was applied to estimate the joint angles. Data were collected on two occasions, one day apart, and a total of twenty trials were acquired for each session. From trial to trial, IMUs 3 and 4 were exchanged of posture. These following approaches were statistically analyzed:

1. In order to evaluate repeatability, understood as the consistency of measures of the IMU system under stated conditions on two days apart, a test-retest (intra-rater) study was

performed. The angles α , β and γ were calculated for each representation of the joint and Intra-Class Correlation (ICC) was calculated. ICC (ICC(2,1), absolute agreement) was calculated using the software IBM SPSS Statistics 20 ($\alpha = 0.05$).

2. In order to evaluate validity, Root Mean Square Error (RMSE) and Concordance Correlation Coefficient (CCC, 95% IC) (LAWRENCE; LIN, 1989) between first-day measured joint angles (using IMU system) and reference values (using the gold-standard universal goniometer) were computed. Two scenarios were analyzed: (a) the differences of joint angles measures changing the postures (POS-1 and POS-2) of the sensors and (b) the differences of joint angles measures using different groups of sensors, i.e., IMU 3 relative to IMU 2 or IMU 4 relative to IMU 2, where IMUs 3 and 4 having the same posture in different occasions.

3.3 Application of the Calibration Procedure on Able-Bodied Subjects

3.3.1 Sensor Placement on Human Lower Limb

Four sensors were positioned from the pelvis through the right lower limb (thigh, shank and foot segments, see Figure 3.3). The pelvis sensor was placed on the sacrum at the S2 spinous process in the middle point between two posterior superior iliac spines. The IMU describes a coordinate system defined as x-axis pointing cranially and z-axis pointing posteriorly. The thigh sensor was placed on the iliotibial tract approximately 5 cm above the patella. The shank sensor was positioned on the lower one-third of lateral shank 5 cm above of the lateral malleolus of the fibula.

The sensors on thigh and shank were positioned with x-axis pointing cranially and z-axis pointing laterally. The foot sensor was fixed with double sided tape on the dorsal region of the foot over the 3rd and 4th metatarsal bones, 3 cm above to the corresponding metatarsophalangeal joints, with z-axis pointing cranially and x-axis pointing posteriorly. These sensors



Figure 3.3: Sensor placement on the human lower limb.

were attached with double-sided tape on an acrylic plate, which was glued to elastic band with Velcro®. Similar positions have been suggested by different authors (TAO et al., 2012; CUTTI et al., 2010; FERRARI et al., 2010).

3.3.2 Discrete Parameters of the Joint Angles

Discrete angular kinematic parameters shown in Table 3.6 were estimated. Discrete parameters allow making a parametric analysis, which is demonstrated to be a reliable and practical method analyzing gait data, and it is a useful tool to assess data reliability (BENEDETTI et al., 1998). These kinematic parameters were computed for each gait cycle. To determine them, there is a need to identify the two main phases of gait, stance and swing. This procedure of segmentation consists of determining the two events that indicate the start of each phase, which are heel strike (HS) and toe off (TO). Sabatini et al. (2005) propose to determine HS and TO using the angular velocity sensed by a gyroscope on the foot. In our work, the orientation data of the foot were collected using quaternions. Each trial is divided in gait cycles to extract the kinematics parameters posteriorly. To determine the HS and TO, the angular velocity, as a

Table 3.6: Joint angles parameters for gait analysis.

Hip		Knee		Ankle	
Name	Variable	Name	Variable	Name	Variable
HFE1	Maximum hip flexion angle stance	KFE1	Maximum knee flexion angle stance	AFE1	Maximum ankle plantarflexion angle stance
HFE2	Maximum hip extension angle stance	KFE2	Maximum knee extension angle stance	AFE2	Maximum ankle dorsiflexion angle stance
HFE3	Maximum hip flexion angle swing	KFE3	Maximum knee flexion angle swing	AFE3	Maximum ankle plantarflexion angle swing

function on quaternion, is computed as shown in Equation 3.10:

$$\mathbf{\Omega}_t = 2^{GS} \mathbf{q}_{BF-FT}^* \otimes^{GS} \dot{\mathbf{q}}_{BF-FT}, \quad (3.10)$$

where $^{GS}\dot{\mathbf{q}}_{BF-FT}$ is the vector of quaternion rates (or the time derivate of the unit quaternion) of the foot, $\mathbf{\Omega}_t = (0, \omega_x, \omega_y, \omega_z)^T$ is the quaternion representation of the angular velocity ω_t . Using the component of the angular velocity on the sagittal plane (ω_y for IMU placed on the foot), the HS and TO events are determined using a minimum detection algorithm. In addition, with these two estimated events, the gait cycle is divided in the two main phases. Thus, it is possible to estimate the mentioned discrete kinematic parameters using maximum and minimum detection algorithm.

3.3.3 Experimental Protocol for Gait Analysis

Five volunteers without gait disabilities (two male and three female, 25 ± 4 years old) were enrolled in the validation procedure of this study. The IMU sensors were placed on pelvis and on right lower limb (thigh, shank and foot segments) by a trained physiotherapist as previously described in Section 3.3.1. The sensor placed on the pelvis was aligned with the walking direction. The subjects were asked to keep a straight upright posture during 5 s, and then walk 10 m in a straight line. Each subject performed three trials and five middle gait cycles were extracted for analysis. This methodology was applied to ensure that only complete gait cycles were selected, excluding motion at the beginning and at the end of the walking process.

Therefore, fifteen gait cycles were acquired for each subject. This research was approved by the Ethical Committee of UFES (Research Project 214/10).

3.4 Results and Discussion

This section presents the results of three approaches applying the proposed method: (1) a simulation that evidences the method performance regardless of drift errors and other perturbations associated with the IMU sensors (considering the limitations of the systems and applications that involve IMU sensors (PICERNO; CEREATTI; CAPPOZZO, 2008; FAVRE et al., 2009; CUTTI et al., 2010; PALERMO et al., 2014; PICERNO; CEREATTI; CAPPOZZO, 2011; O'DONOVAN et al., 2007; CUTTI et al., 2008)); (2) a practical validation using an experimental simplified rigid-body joint and four IMU sensors; and (3) an application in human gait analysis.

3.4.1 Simulation of the Proposed Method Applied to a Simplified Rigid-Body Joint

The IMUs' initial orientations were set to the initial values obtained during practical validation, in order to run the simulation as close as possible to the real experiment. The models of the joint and the IMUs are shown in Figure 3.4. Movements from 0° to $\pm 80^\circ$ with steps of $\pm 20^\circ$ (called Postures 1 to 9) about z-axis of J were performed. Note that the simplified joint is analogous to a two-dimensional knee joint with one degree of freedom.

Figures 3.5a to 3.5c show the angular components (α , β and γ) of the representations J_1 and J_4 (refer to Table 3.5) without applying the proposed method. Other representations of joint J present the same results. Because the proposed method was not yet applied, the angular components α , β and γ presented differences with the expected values. The maximum errors can be observed for J_1 : α (Posture 5) -67.26° , β (Posture 1) -48.96° , γ (Posture 1) 38.77° , and for J_4 : α (Posture 2) -11.69° , β (Posture 5) -57.09° , γ (Posture 9) -42.15° . After applying the

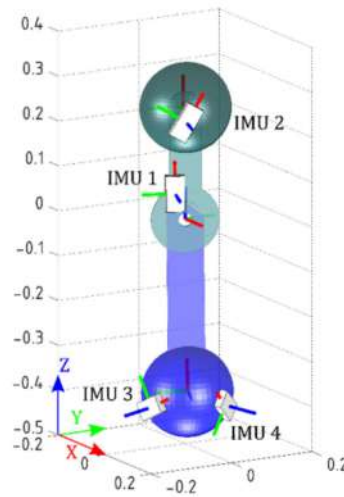
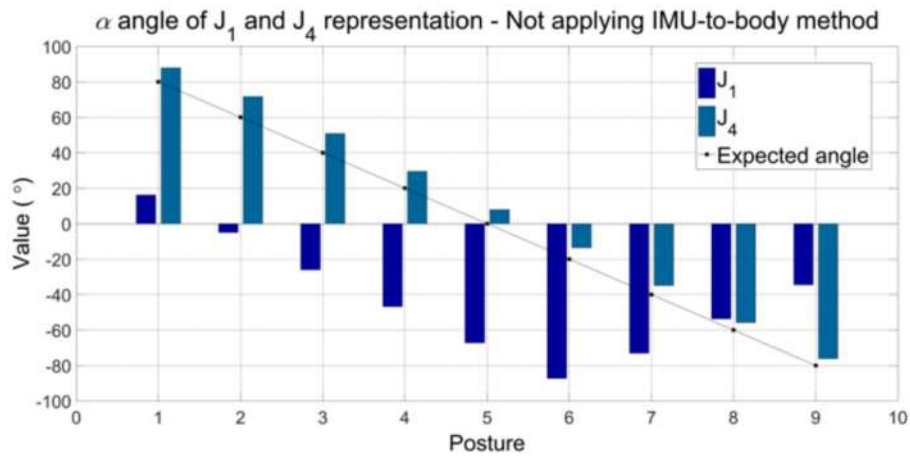
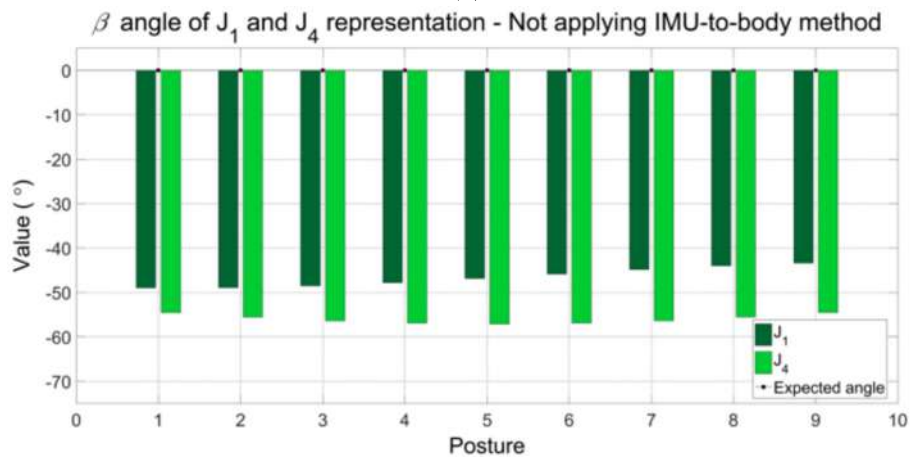


Figure 3.4: Simulation of the simplified joint. Scale models of the rigid-body joint and IMUs in MATLAB.



(a)



(b)

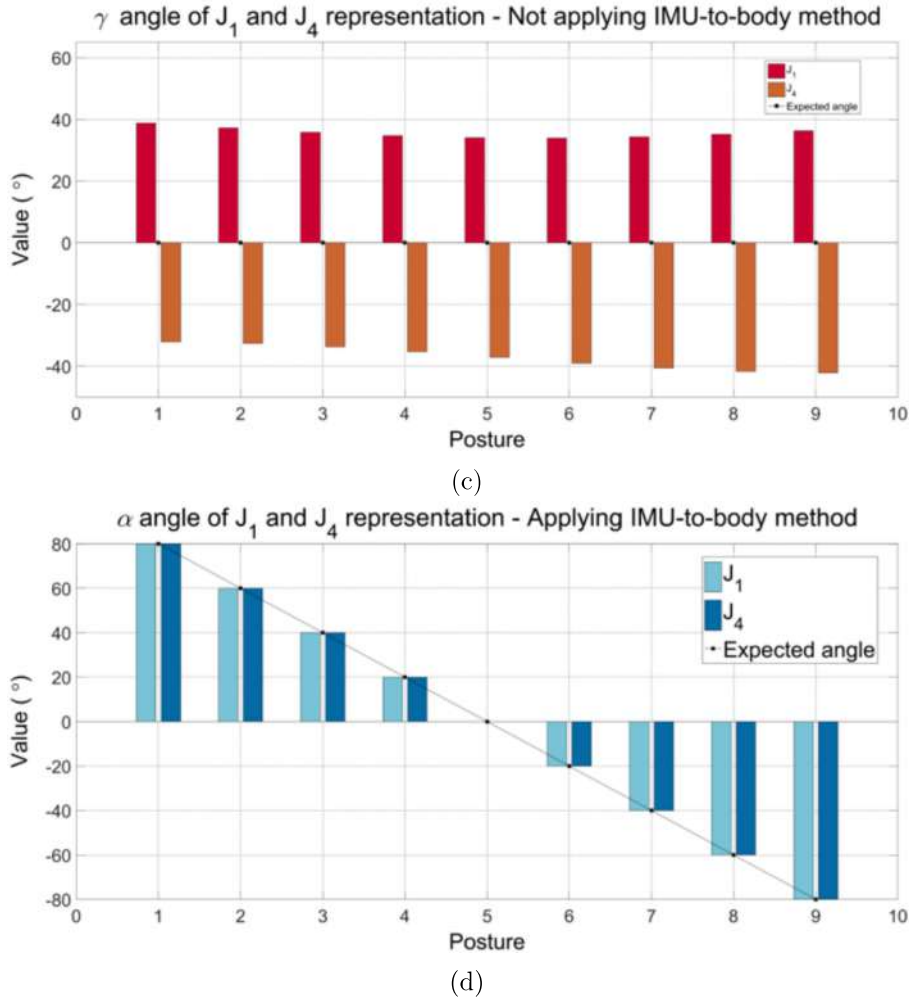


Figure 3.5: Comparison between the joint angles without applying the proposed procedure (a–c) and applying the procedure (d). Angular components α , β and γ are significant in the first case (a–c), which are different of the expected values. In the last case, only α is significant and equal to the expected values. β and γ are both equal to zero throughout the entire simulation, as expected. J_1 and J_4 are two representations of the simulated joint J represented by the goniometer.

proposed method, only α is significant under ideal conditions understanding that the rotations were applied exclusively around z-axis. Then, angular components β and γ are equal to zero. The angles α obtained by applying the IMU-to-body method are shown in Figure 3.5d. Notice that, as the angles β and γ are equal to zero, they are not graphically presented. Also, please observe that the values of α for J_1 and J_4 are equal to the expected values imposed by the simulation. In summary, through this simulation, we aim to demonstrate that applying the proposed method the estimated angles are equal to the expected values and consistent with the

rotations applied. In addition, we also show that the proposed method produces the correct and consistent values when the IMU sensors are placed in different positions on the body segments.

3.4.2 Practical Validation of the Proposed Method Applied to a Simplified Rigid-Body Joint

Table 3.7 shows the data from ICC coefficients and its respective confidence intervals (95% IC) to evaluate the consistency of repeated measures of the IMU system under stated condition on two different days. ICC values were greater than 0.90 for all angular components and the different representations of the joint J . Movements associated with angles α , which correspond to flexion-extension angles on sagittal plane, produced the highest ICC values of the joint (ICC = 1.00). Observe that the angular component γ presented the lowest ICC values and the confidence intervals were wider (e.g., 0.60–0.97). We believe that such values are caused by limitations of the current IMU technology and fusion algorithms. The movements associated with γ angles correspond to external-internal rotation angles, which are performed on transversal plane, perpendicular to the gravity vector. In accordance with the literature, these movements around to the gravity vector present heading drift, which cannot be corrected using the accelerometer data. Therefore, this drift error may be associated with the performance of the magnetometer, gyroscope, and data fusion algorithm. Also, it has been mentioned that the heading drift is mainly due to the accuracy of the IMU sensors and, on a lesser extent, to the

Table 3.7: Test-Retest study on two days apart: Consistency of measures of the IMU system.

Joint	Single Rater ICC Value					
	α		β		γ	
	Value	95% IC	Value	95% IC	Value	95% IC
J₁	1.00	1.00-1.00	0.99	0.98-0.99	0.95	0.83-0.99
J₂	1.00	1.00-1.00	0.99	0.99-0.99	0.96	0.88-0.95
J₃	1.00	1.00-1.00	0.98	0.96-0.99	0.90	0.60-0.97
J₄	1.00	1.00-1.00	0.99	0.98-0.99	0.99	0.98-0.99

complexity of the task (LUINGE; VELTINK, 2005).

Tables 3.8 and 3.9 report the Root Mean Square Error (RMSE) and Concordance Correlation Coefficient (CCC) obtained between first-day measured joint angles (using IMU system) and reference values (using the gold-standard universal goniometer) to evaluate validity, respectively.

The agreement between measures from IMU system and the universal goniometer applying the calibration procedure was excellent ($CCC \geq 0.98$) for the angular component α . Note that for this angular component the maximum RMSE was 1.70° for the J_4 representation on posture 2 (60°). Also, observe that the maximum RMSE (15.61°) is in correspondence with the angle γ . Again, these error drifts may be associated with the quality of the IMU data. In a previous validation study (VALENCIA, 2015), the IMU sensors used here presented errors approximately up to 7° across 12 explored orientations, following the self-IMU consistency (SC) test.

Table 3.8: RMSE between the measurements from IMU system and the reference universal goniometer. Maximum RMSE values of each angular component are highlighted on orange color, and the acceptable values for angular components β and γ are highlighted on green color.

Joint	Angle	RMSE ($^\circ$)									Max RMSE ($^\circ$)
		80	60	40	20	0	-20	-40	-60	-80	
J_1	α	0.67	0.64	0.49	0.30	0.07	0.48	0.74	0.90	0.93	0.93
	β	4.51	4.12	2.72	0.83	0.77	1.77	2.10	0.67	2.36	4.51
	γ	0.25	0.79	1.58	1.39	0.04	2.22	5.14	8.02	9.73	9.73
J_2	α	0.60	0.47	0.16	0.22	0.04	0.49	1.03	1.31	1.21	1.31
	β	1.96	0.09	0.96	0.84	0.04	0.57	1.00	1.50	2.38	2.38
	γ	8.36	6.21	3.81	1.60	0.01	1.02	1.78	2.81	4.44	8.36
J_3	α	1.41	1.13	0.68	0.43	0.02	0.24	0.38	0.39	0.23	1.41
	β	3.11	0.16	1.08	0.20	1.77	4.21	7.68	8.78	6.75	8.78
	γ	8.11	7.44	4.62	1.70	0.01	0.17	2.23	6.26	10.07	10.07
J_4	α	1.42	1.70	0.94	0.55	0.08	0.27	0.63	0.90	0.60	1.70
	β	0.36	3.83	5.00	3.34	0.12	3.63	5.82	6.12	5.00	6.12
	γ	15.61	13.04	7.53	2.69	0.04	0.09	1.74	3.96	5.50	15.61

Table 3.9: CCC between the measurements from IMU system and the reference universal goniometer. Minimum CCC values of each angular component are highlighted on orange color, and the acceptable values for angular components β and γ are highlighted on green color.

Joint	Angle	CCC (ρ_c)									Min. CCC
		80	60	40	20	0	-20	-40	-60	-80	
J_1	α					0.99					0.99
	β	0.25*	0.28*	0.49 [†]	0.94	0.90	0.67	0.67	0.99	0.49 [†]	0.25*
	γ	0.87	0.72	0.58	0.69	0.99	0.48 [†]	0.16*	0.07*	0.05*	0.05*
J_2	α					0.99					0.99
	β	0.53	0.88	0.66	0.77	0.99	0.87	0.67	0.51 [†]	0.40 [†]	0.30*
	γ	0.05*	0.09*	0.20*	0.60	0.99	0.81	0.61	0.40 [†]	0.24*	0.05*
J_3	α					0.99					0.99
	β	0.31*	0.99	0.97	0.99	0.97	0.28*	0.12*	0.10*	0.16*	0.10*
	γ	0.06*	0.08*	0.24*	0.99	0.99	0.99	0.48 [†]	0.17*	0.04*	0.04*
J_4	α					0.98					0.99
	β	0.97	0.30*	0.19*	0.35*	0.99	0.32*	0.16*	0.14*	0.18*	0.14*
	γ	0.02*	0.04*	0.11*	0.49 [†]	0.99	0.99	0.68	0.29*	0.17*	0.02*

* Less than 0.40: agreement between measure poor. [†] Between 0.40 and 0.59: agreement fair.

Errors were found up to 15° , following the Inter-IMU consistency (IC) test. These mentioned tests, with similar results, were proposed by Picerno et al. (2011).

Note that the representations of J associated with IMU 3 (J_1 and J_2) presented the lowest RMSE and the highest CCC values broadly. It is possible to observe that for the angular component α , the measurements are not significantly different when using IMU 3 or IMU 4. However, for the angular components β and γ , the measurements using IMU 3 are lower than those using IMU 4. Additionally, using IMU 3 (the best case), RMSE values of β and γ apparently have similar magnitudes. Nevertheless, note that the magnitudes are not correlated with the same sense of rotation, it means that, for J_1 representation (IMU 3: POS-1), errors are higher from 0 to -80° . On the other hand, for J_2 representation (IMU 3: POS-2), errors are higher from 0 to 80° . Contrary to that demonstrated in simulation, the RMSE data suggest that the position of real IMU sensors is an important factor to consider in analyzes that involve the secondary planes of motion (coronal and transverse planes).

Besides, it is worth noting that the RMSE values mostly increase and CCC values decrease as the angle increases. This can be observed for the angular components β and γ of the J_2 representation. The angular component γ presented the lowest CCC values ($0.02 \leq CCC \leq 0.05$), however, note that for punctual cases, the CCC values were presented into acceptable to excellent interval. For example, for J_1 representation between 80° to -20° (as highlighted in green color), the CCC values were from 0.48 to 0.99, corresponding with RMSE values smaller than 2.5° . This behavior may indicate that pairs of IMU sensors can be used on specific joints, according to their range of motion in gait analysis and, even in other applications that define limits of motion within the range of acceptable performance of the sensors. According to the results obtained using the simplified joint, we present in the next section the hip, knee and ankle joint angles in the sagittal plane through motion analysis using the proposed method.

3.4.3 Experimental Validation for Gait Analysis

Figure 3.6 reports the discrete angular parameters (see Table 3.6) proposed for gait analysis of Subject 2, as an example, over one cycle of gait, to show graphically the kinematic parameters selected in the angular series. Figure 3.7 reports the mean and standard deviation of the joint angles in sagittal plane of the five volunteers. Table 3.10 shows the discrete angular parameters calculated using the mean of fifteen gait cycles for the five volunteers.

Mean and standard deviation of the joint angles of the five volunteers are within the normal range during a gait cycle for free walking. Interestingly, the results obtained with the developed algorithm presented low standard deviations, which means that estimated measures were consistent across trials. The maximum values of standard deviation were presented for the ankle joint angles of the five volunteers (Maximum SD = 3.99, AFE3, Subject 5). According to the

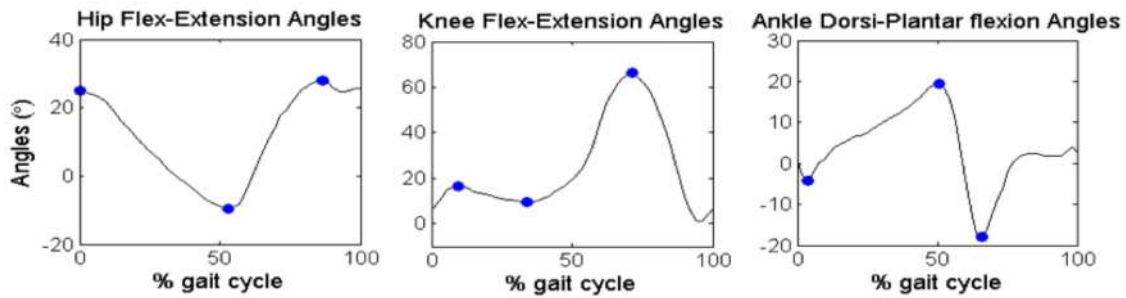


Figure 3.6: Discrete angular parameters on joint angles of Subject 2.

Table 3.10: Mean (SD) of the discrete parameters reported for five volunteers.

Parameter	MEAN (SD)(°)				
	Subject 1	Subject 2	Subject 3	Subject 4	Subject 5
HFE1	25.44 (2.62)	25.14 (2.78)	26.19 (2.18)	23.18 (2.54)	20.75 (2.73)
HFE2	-13.52 (3.97)	-9.62 (2.81)	-13.39 (2.00)	-9.39 (2.67)	-9.66 (2.86)
HFE3	28.87 (2.51)	27.96 (2.57)	29.38 (1.83)	24.63 (2.44)	20.28 (2.73)
KFE1	16.24 (3.10)	16.29 (2.75)	14.08 (3.12)	10.79 (2.65)	9.99 (0.63)
KFE2	4.63 (2.98)	9.62 (2.92)	7.58 (2.98)	2.98 (3.20)	5.23 (0.23)
KFE3	59.35 (1.70)	66.24 (2.82)	65.59 (2.88)	55.01 (2.80)	55.93 (1.55)
AFE1	-1.42 (3.93)	-4.16 (1.56)	-6.08 (2.51)	-6.76 (3.42)	-2.93 (3.98)
AFE2	16.95 (2.51)	19.43 (1.21)	10.55 (3.74)	9.53 (2.63)	8.48 (1.64)
AFE3	-10.32 (3.52)	-17.80 (3.46)	-21.52 (2.02)	-30.51 (2.49)	-25.15 (3.99)

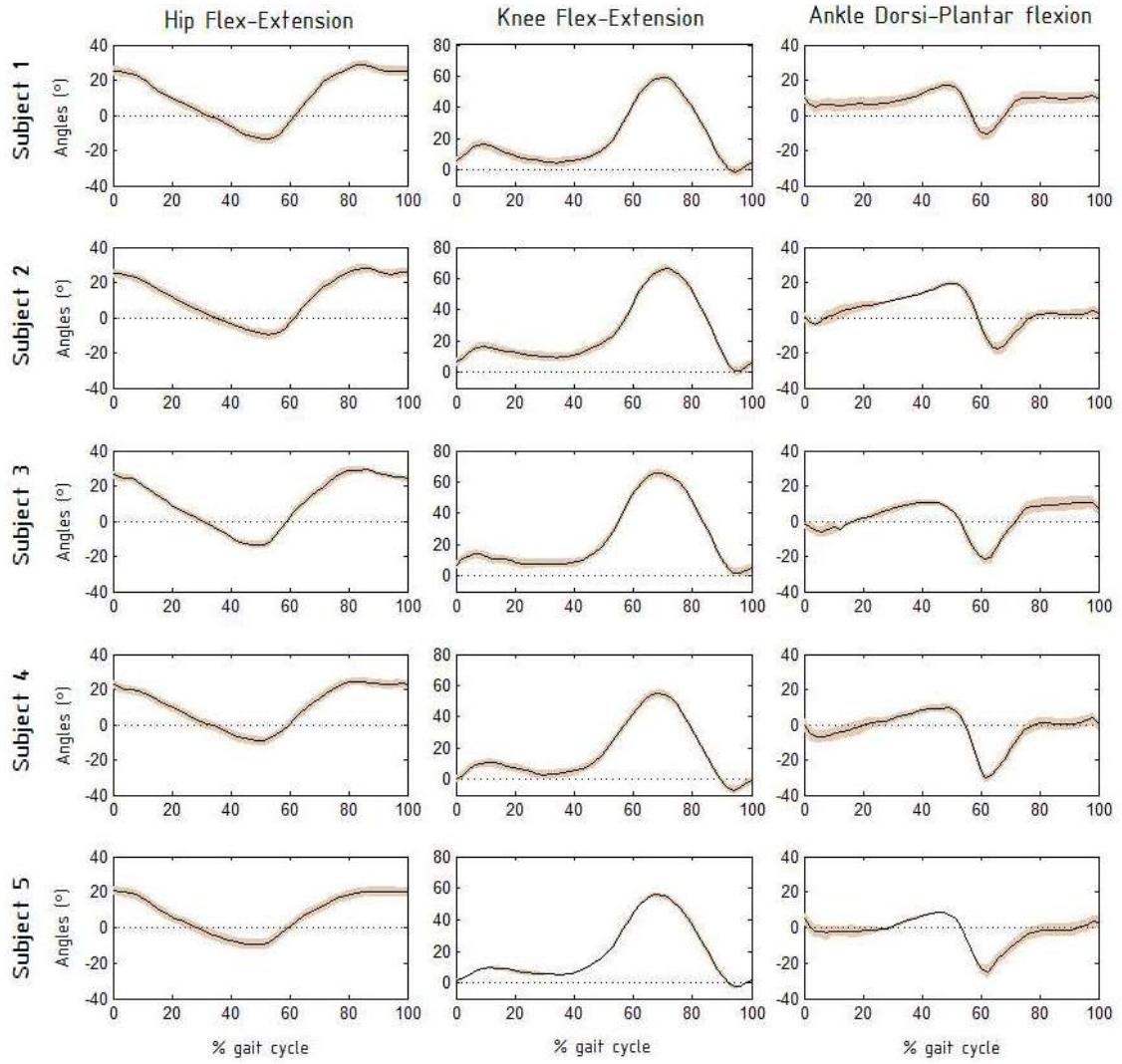


Figure 3.7: Joint angular kinematics in stride percentage (from HS to HS) of five able-body subjects. Fifteen gait cycles were summarized by black curve (MEAN) and orange stripe (\pm SD).

results of each subject, it is possible to identify characteristics of each individual. By comparing the results obtained using the proposed method with the literature (PICERNO; CEREATTI; CAPPOZZO, 2008; PALERMO et al., 2014; FERRARI et al., 2010; BENEDETTI et al., 1998) it is clear that the angular patterns are coherent and within the intervals established by mean and standard deviations. It is important to highlight that these experiments were performed with the intention of proving a practical application of the proposed method.

Notice that technical-anatomical frames, used to calculate the joint angles, are an estimate and may present a misalignment with the anatomical frame defined using bony landmarks. This

means that joint angle curves may present an offset from values estimated using stereophotogrammetry, preserving the same angular patterns and range of motion.

3.5 Preliminary Conclusions

In this work we have presented a novel calibration method to place and align inertial sensors with human body segments, with the goal of measuring joint angles. The advantages of the proposed method, in comparison with other methods described in the literature, include the fast and easy sensor placement, with no need of special movements performed by the user nor any additional tools, which may decrease setup time. The characteristics of this new method may make it more attractive for daily clinical routine.

The results from the computational simulation demonstrate that, when applying the proposed method, the estimated angles are equal to the expected values and consistent with the joint's rotations. Also, two real experiments have been carried out to evaluate the simulated procedure. Results indicate that the method is suitable to measure tridimensional angles of the hip, knee and ankle of the humans' joints during free walking. However, some limitations mainly associated with the accuracy of the sensors used in the real experiments for practical validation gave rise to some estimation errors, mainly in movements around the gravity vector.

In conclusion, the proposed method is an interesting option to solve the alignment problem of human gait analysis based on inertial sensors. The discussed method is especially attractive for its simplicity and easy donning and doffing of the sensors. In applications such as gait rehabilitation, that requires motion analysis of impaired persons, the method can be of great help for its simplicity and accurate results.

Chapter 4

Sleeve for Knee Angle Monitoring: A Novel IMU-POF Sensor Fusion System

The knee flexion-extension angle is an important variable to monitor rehabilitation progress, for instance, after a knee replacement. This chapter presents the development and evaluation of a novel IMU-POF sensor fusion system based on a knee sleeve for monitoring physical therapy. The system consists of merging data from two inertial measurement units (IMUs) and a Polymer Optical Fiber (POF) curvature sensor using a quaternion-based Multiplicative Extended Kalman Filter (MEKF). The proposed fusion method is magnetometer-free and deals with sensors uncertainties through reliability intervals defined during gait. We tested the developed system and methods on twelve healthy young adults in a number of comparison scenarios, when using single-sensor or multi-sensor-fusion methods and when using other methods recently presented in the literature. All measurements obtained by the proposed system were validated using an optical motion capture system.

4.1 Introduction

A pathological gait pattern may occur after an injury, illness or accident. Within non-pharmacological treatments to effectively manage a joint disease is the physical therapy. As well, in this context,

motion analysis is an essential field, which allows understanding the characteristics of different musculoskeletal disorders during the rehabilitation process. Therefore, developing smart wearable monitoring systems could be highly useful to frequently assess the mobility state. Also, such devices could record gait-related parameters and monitoring joint movements during activities of daily living (MURO-DE-LA-HERRAN; GARCIA-ZAPIRAIN; MENDEZ-ZORRILLA, 2014).

Recent studies in the literature (SEEL; RAISCH; SCHAUER, 2014; VITALI et al., 2017; MCGRATH; FINEMAN; STIRLING, 2018; ALLSEITS et al., 2018) have proposed devices and methods for knee motion monitoring by using IMUs, and even in combination with other sensors (TOGNETTI et al., 2015). Perhaps, IMUs have become the most popular wearable systems for motion tracking and are now being increasingly used to measure joint angles when compared to other technologies (FAISAL et al., 2019). In (SEEL; RAISCH; SCHAUER, 2014), the authors proposed a method to calculate the joint angles using gyroscopes and accelerometers merged by a complementary filter, and no-assumption about sensors orientations is made. Such method consists of estimating the 1-DOF joint angle by identifying the joint axis and positions. Therefore, the analyzed joints (knee and ankle) are assumed as hinge joint. For this, the authors used a Gauss-Newton method to solve the nonlinear problem of finding the joint axis and positions by means of least squares. RMSE about 3° was reported for knee flexion-extension angle, however, the method was evaluated with a single participant performing six walking trials.

In a recent research (MCGRATH; FINEMAN; STIRLING, 2018), the authors used Principal Component Analysis (PCA) to estimate the knee flexion-extension axis using the relative angular velocity between two IMUs. An Unscented Kalman Filter (UKF) implemented by the manufacturer provided the orientation measurements, and the knee joint is also assumed as a hinge joint. In addition, the authors presented results using simulated IMUs. Fifteen subjects performed the test, and a zero-mean RMSE of 9.4° was reported for data from real IMUs, being

the worst case a RMSE of 16.97° , when compared against an optical motion capture system.

Another recent study (ALLSEITS et al., 2018) presented a novel method for knee angle estimation using two leg-mounted gyroscopes. The authors used the method introduced by Seel, Raisch and Schauer (2014) to compute the knee joint axis. Then, they calculated the knee angle from integration of a gyroscope-derived knee angular velocity signal. In order to eliminate the drift due to integration, a zero-angle update deduced from a characteristic point in the knee angular velocity is applied every stride. Six subjects participated in the experiments and a comparison to a camera-based system (Vicon) was presented. A mean difference of 5° for peak knee angle at swing flexion was reported, but RMSE for whole gait cycle was not evaluated.

Unlike the previously mentioned researches, a fusion between signals from a wearable goniometer and accelerometers was presented by Tognetti et al. (2015). The electrogoniometer was developed by coupling two piezoresistive layers, made of knitted piezoresistive fabric (KPF), through an electrically-insulating layer. The fusion algorithm was a Kalman Filter where measurements were updated using the accelerometers data. The system was worn by five healthy subjects and trials of standing movements and walking, in four non-measured gait speed, were analyzed. The reference measurement was the knee angle estimated by the same IMU-based system using the procedure provided by Xsens (Xsens, Netherlands). Regarding walking trials, a mean RMSE of up to 2.5° was reported. Nevertheless, one limitation, highlighted by the authors, was to evaluate their system against an IMU-based system, since the gold standard in biomechanics are marker-based optical motion capture systems.

From the literature review and to the author's knowledge, few studies combine IMU measurements with other wearable aiding sensors different of magnetometers in order to improve the accuracy for joint angle estimation. As aforementioned, Tognetti et al. (2015) presented a fusion of accelerometer signals with signals from a piezoresistive-based electrogoniometer. However, unlike other works (PALERMO et al., 2014; SEEL; RAISCH; SCHAUER, 2014; MCGRATH; FINEMAN; STIRLING, 2018; ALLSEITS et al., 2018), the reference system was not an optical motion capture system, instead, an IMU motion capture system was used, the same that

provided the acceleration measurements, adding the fact that the description of the reference measurements processing was limited.

Furthermore, different works in the literature (PASCIUTO et al., 2015; BERGAMINI et al., 2014; PICERNO; CEREATTI; CAPPOZZO, 2011) have questioned the accuracy of IMU-based systems, since high errors, mainly associated with the use of magnetometers and the drift produced by integrating gyroscope measurements, are presented. In the literature, different algorithms have been proposed to decrease orientations errors due to magnetic distortion (LAIDIG; SCHAUER; SEEL, 2017; LIGORIO; SABATINI, 2016) and still use magnetometers to estimate heading movements. However, most of algorithms are based on the assumption of a homogeneous magnetic field (WITTMANN; LAMBERCY; GASSERT, 2019) in a calibration stage or at rest, but when the assumption is violated often in indoor environments and during movement, magnetometer measurements becomes unreliable (TEUFL et al., 2018; SEEL; RAISCH; SCHAUER, 2014). Also, although a magnetic distortion compensation technique is used, electromagnetic disturbances are not completely eliminated since magnetometer measurements are involved in the estimation process (LEE; JEON, 2018). Thus, methods that omit magnetometer data have been also developed and generally exploiting kinematic constraints (LEE; JEON, 2018; TEUFL et al., 2018; MOLNAR et al., 2018; FASEL et al., 2017). These findings show different issues and challenges related to the reliability of IMU-based systems used in ambulatory applications, which encourage to explore other wearable technologies. Also, further studies should be conducted aiming to evaluate the validity of such a wearable systems and considering, if possible, a greater number of participants.

Additionally, it was discussed that EKF takes time to recover from false measurements (SABATINI, 2011). In this way, different approaches seek to prevent the filter from processing data considered unreliable. Many EKF designs in the literature (GHOBADI; ESFAHANI, 2017a; SABATINI, 2011; SUH, 2010) propose different ways to deal with anomalous measurements. However, in these applications, the filters are conceived to improve accuracy of a single sensor unit. In (NOGUEIRA et al., 2013) the authors proposed to use Force Sensitive Resistor (FSR) and accelerometer to identify gait intervals of reliable accelerations. Then, in (NOGUEIRA et

al., 2017), the authors used only accelerometers and defined as many thresholds as used single sensor units in order to correct the estimation error in the update step of a matricial global Kalman Filter.

In this research, we evaluated the validity of knee flexion-extension angle measurements as being an important tool in clinical applications. Motivated by the still open challenges in the literature, we developed and evaluated a novel IMU-POF sensor fusion system based on a knee sleeve for monitoring physical therapy. The system consists of merging data from two IMUs and one POF curvature sensor using a quaternion-based Multiplicative Extended Kalman Filter (MEKF) exploiting kinematic constraints. In addition, the proposed fusion method is magnetometer-free seeking for avoiding inaccuracies related to electromagnetic disturbances.

Moreover, we proposed to deal with sensors uncertainties using reliability intervals defined during specific gait phases. For this purpose, a rule-based algorithm for gait phases identification was implemented. Finally, we analyzed and compared whole knee angle curves on the sagittal plane in two different scenarios: i) comparisons between single-sensor and multi-sensor fusion methods and ii) comparisons of the IMU-POF based MEKF to others methods in the literature.

This chapter is divided as follows. Section 4.2 introduces the novel IMU-POF based knee sleeve system. Section 4.3 describes the methods for computing the knee joint axis and positions, and the gait phases identification using IMUs, along with the procedure for POF sensor characterization and the IMU-POF based MEKF for estimating knee flexion-extension angle. The experimental protocol, data and statistical analyses are described in Section 4.4. Results and discussions about the performance of our system are presented in Section 4.5. Preliminary conclusions and final considerations are presented in Section 4.6.

4.2 A Novel IMU-POF Based Knee Sleeve System

The knee sleeve system depicted in Figure 4.1 (a) consists of two 3D printed sensor enclosures integrated into a commercial knee sleeve via velcro and elastic straps. The adjustable

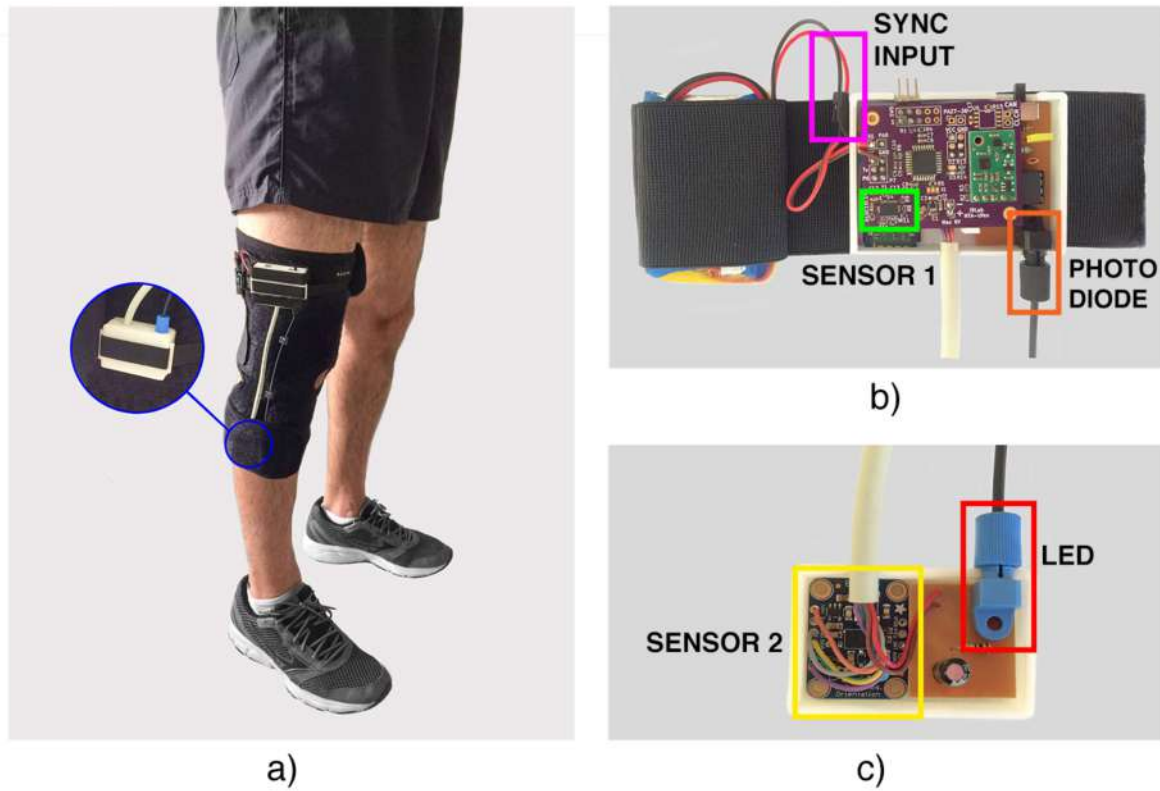


Figure 4.1: IMU-POF based knee sleeve system. (a) Knee sleeve system placed on a participant. Instrumented part: (b) main hardware unit and (c) second unit

knee sleeve is made of neoprene and has a reinforced hole that keeps the patella centralized and protected, and also has velcro closure (3 adjustments sizes) for greater compression. The instrumented part is shown in Figure 4.1 (b-c). In the main unit (Figure 4.1 (b)), one IMU BNO055 sensor (Bosh Sensortec, Germany) with 3D accelerometer, 3D gyroscope, 3D magnetometer, is embedded (SCHNEIDER, 2018), which is connected to a 32-bit Atmel Cortex M0+ SAMC21E18A microcontroller via Inter-Integrated Circuit (I2C) protocol. An optoelectronic receiver module, placed on an additional printed circuit board (PCB), comprises a photodiode IF-D91 (Industrial Fiber Optics, USA) and an operational amplifier (MCP6021) to deal with the signal provided by the POF sensor. An HC-05 Bluetooth module was used to communicate data wirelessly with a personal computer. A 3.7 V rechargeable lithium polymer battery supplies power to all units. In the second unit (Figure 4.1 (c)), another IMU BNO055 sensor was included along with the optoelectronic transmitter module, comprising a LED IF-E97 (Industrial Fiber Optics, USA). A sampling frequency of 100 Hz was used.

We used in this work a multimode HFBR-EUS100Z POF (Broadcom Limited, Singapore), with a Polymethyl Methacrylate (PMMA) core and a cladding of 980 μm and 10 μm of thickness, respectively. Additionally, it has a polyethylene coating for mechanical protection, which results in a total diameter of 2.2 mm for this fiber. The sensitive zone (as explained in Section 2.2.4) was made through abrasive removal of material, with a depth and length of about 14 mm and 0.6 mm, respectively. The orientation of the removed lateral section was chosen in order to have convex curvature during the knee flexion movement.

4.3 Methods for IMU-POF based Knee Joint Angle Measurement

As previously mentioned, a challenge related to the use of IMU systems in human joint tracking is that the alignment of sensor-to-body axes is unknown. In this chapter, we present a new system based on the fusion of signals from two IMUs and a POF curvature sensor to measure knee kinematics. Since there is not a sensor that could be used as reference (as in Chapter 3), another alignment method is introduced. Therefore, in order to align the IMU sensors to the joint, we first estimate the knee joint axis and position. Next, we present a method to identify gait phases, which allows defining time intervals of more reliable measurements provided by the accelerometers and POF sensors. Motivated by improving the accuracy of the system, we proposed a magnetometer-free multi-sensor fusion algorithm based on a MEKF with kinematics constraints.

4.3.1 Estimation of Knee Flexion-Extension Axis and Position Using IMUs

Because it is imperative that the POF sensor is aligned to the joint and the implemented system is fixed, the orientation of the IMU sensors on the thigh and shank may vary highly among users. Accordingly, no assumption about the IMU sensors mounting can be made. The method

presented here avoids this assumption and requires no predefined posture or movements.

Anatomically, the knee is the largest synovial joint in the body (SAAVEDRA et al., 2012). It is formed between four bones, the patella, fibula, femur and tibia, comprising three separate articulations, namely, patellofemoral, medial and lateral tibiofemoral (NETTER; THOMPSON, 2002), which together form a complex hinge joint. Similarly, some authors describe that the knee contains two joints: tibiofemoral and patellofemoral (YANG; JAIN, 2017; STARKEY; JOHNSON, 2006), where tibiofemoral consists of two compartments, medial and lateral. Thus, the tibiofemoral joint is commonly modeled as a hinge joint (DOOLEY et al., 2019; MCGRATH; FINEMAN; STIRLING, 2018), considering flexion-extension axis as the main axis of rotation. Nevertheless, external-internal rotation and abduction-adduction movements occur, although in minimal proportion, rarely exceeding a range of $\pm 10^\circ$ (FAVRE et al., 2008). Also, soft-tissue artifacts highly affect the movements in secondary planes (STAGNI et al., 2005). Knee kinematics is hard to be described unequivocally and mathematically correct, since this joint consists of rotation around different axes, in addition to translations (VICTOR, 2017). Nonetheless, the finite helical axis is an effective approach to describe knee joint motion (BISHOP et al., 2018; COLLE et al., 2016). Because of this, using a hinge joint model has been suitable in some kinematic applications (DOOLEY et al., 2019; MCGRATH; FINEMAN; STIRLING, 2018; ALLSEITS et al., 2018; TEAGUE et al., 2016; SEEL; RAISCH; SCHAUER, 2014). However, this assumption could provide inaccurate results, for instance, to estimate muscle forces (MAROUANE; SHIRAZI-ADL; ADOUNI, 2017). For practical purposes, in our research, the human knee is modeled as a single degree of freedom (1-DOF) hinge joint (MCGRATH; FINEMAN; STIRLING, 2018; ALLSEITS et al., 2018).

We implemented an algorithm based on a method initially introduced by Seel, Raisch and Schauer (2014). Some posterior researches (GRAUROCK; SCHAUER; SEEL, 2016) found that the method is highly influenced by soft-tissue effects. In order to reduce these effects, in our research three criteria were implemented in order to filter undesirable samples.

The method to estimate the knee main axis and position consists of three stages: (1) Apply the

three criteria filter (named here as 3CRTF) with the objective of rejecting mainly the samples of movements not associated with flexion-extension motion; (2) Use the thigh and shank filtered gyroscope measurements and kinematic constraints in order to estimate the joint axis during gait, and (3) Use the thigh and shank filtered accelerometer measurements to estimate the joint center position in the local coordinates of the sensors. Finally, the angular velocities and accelerations associated only with flexion-extension movements are estimated. These outcomes feed the multi-sensor fusion filter.

Stage 1: First, the angular velocities and accelerations collected during each trial of gait were low pass filtered using a 4th order Butterworth filter with a 10 Hz cutoff. Also, we removed the static gyroscope output (bias) by subtracting the average of 2 seconds static measurements. Next, we applied a filter 3CRTF to reject samples of both the gyroscopes and the accelerometers, which satisfy the three following criteria:

1. The sum of the magnitudes (Euclidean norm) of the angular velocities vectors is below a threshold ($< 30^\circ/s$).
2. The movements mainly around the longitudinal axis of the thigh sensor exceed a small threshold ($> \xi_g$).
3. The movements mainly around the longitudinal axis of the shank sensor exceed a small threshold ($> \xi_g$).

The threshold values in criteria 2 and 3 were chosen empirically by data examination to be equal to 0.2. According to the method presented by Woltring (1990) to define the joint instantaneous helical axis (IHA) in photogrammetry applications, the angular velocity must be sufficiently large to overcome the effect of noise. Therefore, rejecting angular velocities lower than 10% of the maximum velocity could be adopted (CUTTI et al., 2008; BESIER et al., 2003; STOKDIJK et al., 1999). The maximum relative angular velocities presented in this work are between 300 and 400 $^\circ/s$. Therefore, we chose a threshold value of 30 $^\circ/s$ for criteria 1.

The longitudinal axis is computed for each local coordinate sensor by averaging the 3D acceler-

ation measurements over 3 seconds during gait. To estimate the movement around longitudinal axis, the scalar product of the gyroscope measurements (normalized) and the calculated longitudinal axis is applied. This 3CRTF filter is summarized in the Algorithm 1 (Appendix A.1). Consider the 3D angular velocities and accelerations of thigh ($\boldsymbol{\omega}_1 = [\omega_x, \omega_y, \omega_z]$, $\mathbf{a}_1 = [a_x, a_y, a_z]$) and shank ($\boldsymbol{\omega}_2 = [\omega_x, \omega_y, \omega_z]$, $\mathbf{a}_2 = [a_x, a_y, a_z]$) sensors provided by the low pass filtering.

Stage 2: The knee main axis expressed with respect to the local coordinate system of the thigh sensor is denoted as \mathbf{j}_1 , and for shank sensor as \mathbf{j}_2 . Note that \mathbf{j}_1 and \mathbf{j}_2 are supposed to be the same vector in a global coordinate system (see Figure 4.2). Assuming a hinge joint, the projections of the angular velocities into the joint plane have the same length for each instant in time. Because of this fact, the non-linear problem to find the vectors \mathbf{j}_1 and \mathbf{j}_2 that fulfill Equation 4.1, in a least-squares sense, can be solved using a Gauss-Newton optimization algorithm (SEEL; RAISCH; SCHAUER, 2014). Since the joint axis estimates are expected to be unit length, the estimation problem is reduced to find four parameters using spherical coordinates.

$$\|\boldsymbol{\omega}_2(t) \times \mathbf{j}_2\|_2 - \|\boldsymbol{\omega}_1(t) \times \mathbf{j}_1\|_2 = 0, \quad \forall t \quad (4.1)$$

$\|\cdot\|_2$ denotes the Euclidean norm. The implementation of this method is presented in Algorithm 2 (Appendix A.2). To simplify the notation, the angular velocities resulting of the stage 1 are

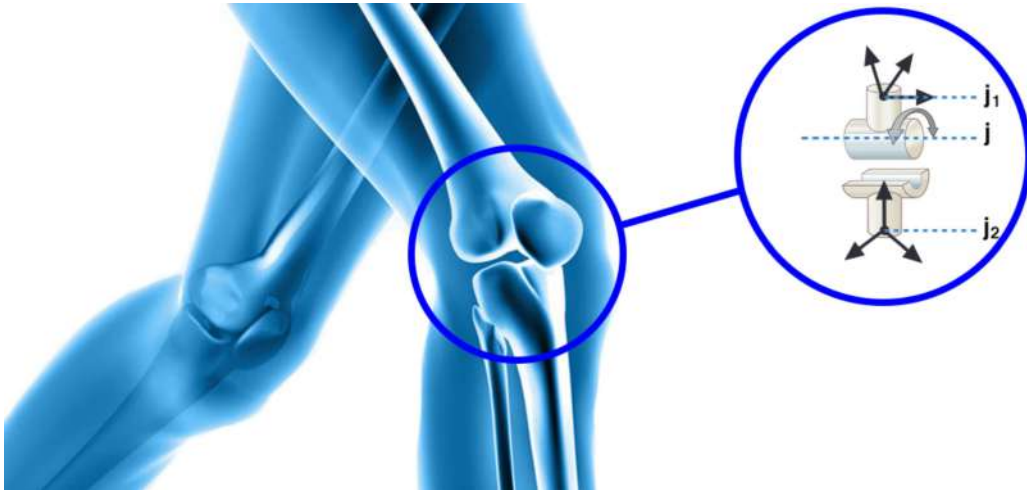


Figure 4.2: Human knee as a single degree of freedom (1-DOF) hinge joint. \mathbf{j} is the knee main axis in a global coordinate system, and \mathbf{j}_1 and \mathbf{j}_2 are the same axis in the local coordinate systems of the thigh's and shank's sensors, respectively.

denoted as $\boldsymbol{\omega}_1$ and $\boldsymbol{\omega}_2$. The initial value of $\boldsymbol{\eta}_{axis}$ can be any value (see Appendix A.2).

Stage 3: The center of knee joint position with respect to the local coordinate system of thigh and shank sensors is denoted as \boldsymbol{o}_1 and \boldsymbol{o}_2 , respectively. \boldsymbol{o}_1 and \boldsymbol{o}_2 are defined pointing from the origin of each sensor to the joint center. Exploiting the kinematic constraints of two links connected by a spheroidal joint, the accelerometer measurements are used to compute these vectors (SEEL; RAISCH; SCHAUER, 2014). Again, Gauss-Newton optimization procedure is applied in order to find the vectors \boldsymbol{o}_1 and \boldsymbol{o}_2 that fulfill Equation 4.2.

$$\|\boldsymbol{a}_1(t) - \boldsymbol{o}_1 \times \dot{\boldsymbol{\omega}}_1(t) - \boldsymbol{\omega}_1(t) \times \boldsymbol{o}_1 \times \boldsymbol{\omega}_1(t)\|_2 - \|\boldsymbol{a}_2(t) - \boldsymbol{o}_2 \times \dot{\boldsymbol{\omega}}_2(t) - \boldsymbol{\omega}_2(t) \times \boldsymbol{o}_2 \times \boldsymbol{\omega}_2(t)\|_2 = 0, \quad \forall t \quad (4.2)$$

where $\dot{\boldsymbol{\omega}}_1$ and $\dot{\boldsymbol{\omega}}_2$ are the first derivative of $\boldsymbol{\omega}_1$ and $\boldsymbol{\omega}_2$, respectively. When the relative motion between two segments is restrict to a single plane, which is the case of a hinge joint, Equation 4.2 is met for all points along the joint axis (SEEL; RAISCH; SCHAUER, 2014). Also, it is worth to point that $\boldsymbol{o}_i \times \dot{\boldsymbol{\omega}}_i(t) + \boldsymbol{\omega}_i(t) \times \boldsymbol{o}_i \times \boldsymbol{\omega}_i$ is typically small compared to the gravitational component. Thus, at normal and slow gait speed, almost the same accuracy is yielded when using $\boldsymbol{o}_1 = \boldsymbol{o}_2 = [0, 0, 0]^T$. The implementation of this method is presented in Algorithm 3 (Appendix A.3). To simplify the notation, the 3D angular velocities and accelerations outcomes of the stage 1 are denoted as $\boldsymbol{\omega}_1$, $\boldsymbol{\omega}_2$, \boldsymbol{a}_1 and \boldsymbol{a}_2 . The initial value of $\boldsymbol{\eta}_{pos}$ can be any value (see Appendix A.3). Next, by using the projection of the thigh and shank angular velocities about \boldsymbol{j}_1 and \boldsymbol{j}_2 , and calculating the accelerations using \boldsymbol{o}_1 and \boldsymbol{o}_2 , the joint angle calculation problem is reduced to a single plane. Therefore, without loss of generality, the knee angular velocity vector can be expressed in the local coordinate system of the shank sensor, as shown in Equation 4.3.

$$\begin{aligned} \boldsymbol{\omega}_{TS}^S(t) &= \boldsymbol{\omega}_S^S(t) - \boldsymbol{\omega}_T^S(t) \\ \boldsymbol{\omega}_{TS}^S(t) &= \frac{\boldsymbol{\omega}_2(t) \cdot \boldsymbol{j}_2}{\|\boldsymbol{j}_2\|} \frac{\boldsymbol{j}_2}{\|\boldsymbol{j}_2\|} - \frac{\boldsymbol{\omega}_1(t) \cdot \boldsymbol{j}_1}{\|\boldsymbol{j}_1\|} \frac{\boldsymbol{j}_2}{\|\boldsymbol{j}_2\|}, \end{aligned} \quad (4.3)$$

where $\boldsymbol{\omega}_T^S$ and $\boldsymbol{\omega}_S^S$ are the 3D angular velocity vectors of thigh and shank sensors expressed with respect to the shank sensor's coordinate frame, respectively. Note that $\boldsymbol{\omega}_{TS}^S$ is the vector projection of the relative angular velocity onto the joint axis. We should recall that \boldsymbol{j}_1 and \boldsymbol{j}_2 are supposed to be the same vector in a global coordinate system and that they are also

unit vectors. In practice, this remains true if just some (ideally small) errors due to soft-tissue artifacts and other perturbations of the IMUs occur. Now, in order to shift the acceleration measurements to the joint axis, Equations 4.4 and 4.5 are used.

$$\begin{aligned}\tilde{\mathbf{a}}_1(t) &= \mathbf{a}_1(t) - \mathbf{o}_1 \times \dot{\boldsymbol{\omega}}_T(t) - \boldsymbol{\omega}_T(t) \times \mathbf{o}_1 \times \boldsymbol{\omega}_T(t) \\ \tilde{\mathbf{a}}_2(t) &= \mathbf{a}_2(t) - \mathbf{o}_2 \times \dot{\boldsymbol{\omega}}_S(t) - \boldsymbol{\omega}_S(t) \times \mathbf{o}_2 \times \boldsymbol{\omega}_S(t)\end{aligned}\tag{4.4}$$

$$\begin{aligned}\mathbf{a}_T(t) &= \tilde{\mathbf{a}}_1(t) - \frac{\tilde{\mathbf{a}}_1(t) \cdot \mathbf{j}_1}{\|\mathbf{j}_1\|} \frac{\mathbf{j}_1}{\|\mathbf{j}_1\|} \\ \mathbf{a}_S(t) &= \tilde{\mathbf{a}}_2(t) - \frac{\tilde{\mathbf{a}}_2(t) \cdot \mathbf{j}_2}{\|\mathbf{j}_2\|} \frac{\mathbf{j}_2}{\|\mathbf{j}_2\|},\end{aligned}\tag{4.5}$$

where $\tilde{\mathbf{a}}_1(t)$ and $\tilde{\mathbf{a}}_2(t)$ are the same acceleration estimated in two different local frames, which rotate with respect to each other around the joint principal axis (SEEL; RAISCH; SCHAUER, 2014), and $\dot{\boldsymbol{\omega}}_T$ and $\dot{\boldsymbol{\omega}}_S$ are the first derivative of $\boldsymbol{\omega}_T$ and $\boldsymbol{\omega}_S$, respectively. Moreover, $\mathbf{a}_T(t)$ and $\mathbf{a}_S(t)$ are the projections of $\tilde{\mathbf{a}}_1(t)$ and $\tilde{\mathbf{a}}_2(t)$ into the joint plane. $\mathbf{a}_T(t)$ and $\mathbf{a}_S(t)$ were calculated based on kinematic constraints and feed the multi-sensor fusion filter.

4.3.2 Gait Detection Phases Using IMUs

In the MEKF presented in Section 4.3.4, we used time intervals where the accelerometers and POF sensor measurements are expected to be more reliable. This is done through of the identification of specific gait phases using a rule-based method. Generally, regarding acceleration, the more reliable instants are defined as those in which the measured acceleration vector is almost the gravity vector. We applied this fact for the relative acceleration, where the absolute value of the difference of the acceleration magnitudes should be below a threshold ξ_a , as shown in Equation 4.6.

$$||\|\mathbf{a}_2\|_2 - \|\mathbf{a}_1\|_2| < \xi_a,\tag{4.6}$$

where \mathbf{a}_1 and \mathbf{a}_2 are the low pass filtered accelerations. However, as can be observed in Figure 4.3 (a-b), this condition may be fulfilled close to impacts, between peaks of accelerations, as the initial contact and push off. Therefore, we propose to use this condition in static conditions and during the end of loading response and terminal-stance (TSt) phases (approximately around

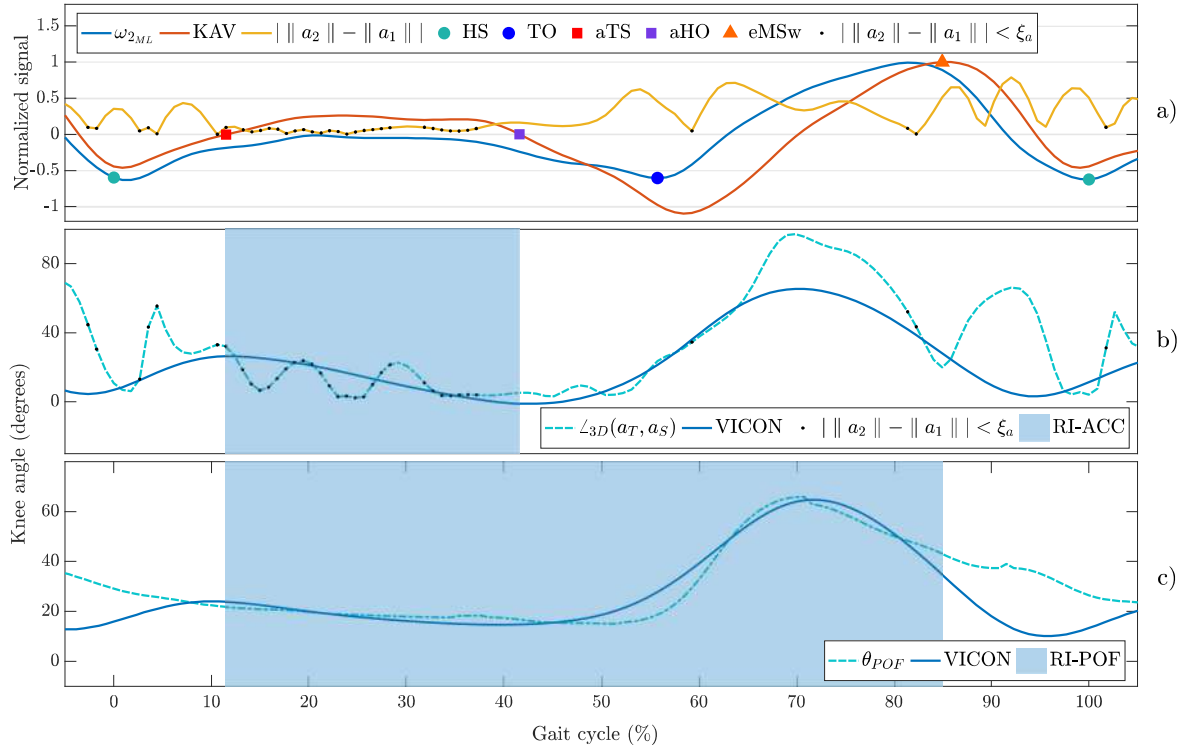


Figure 4.3: Reliability intervals of the accelerometers and POF curvature sensor for each gait cycle. (a) Angular velocity of the shank's gyroscope medio-lateral axis, $\omega_{2_{ML}}$ (blue curve), knee angular velocity, KAV (orange curve), absolute value of the difference of the acceleration magnitudes (yellow curve), heel strike (HS) events (green dot mark), toe off (TO) events (blue dot mark), toe strike (aTS) events (red square mark), heel off (aHO) events (purple square mark), the end of the mid-swing (eMSw) phase (orange triangle mark), points where the difference of the acceleration magnitudes is below a threshold η_a (black dot mark). (b) Accelerometers-based joint angle (light blue curve), reference (Vicon) angle (blue curve), RI-ACC (blue stripe). (c) POF curvature sensor-based joint angle (light blue curve), RI-POF (blue stripe).

10 - 40% of gait cycle), when the foot remains in full contact with the ground. We called this interval as RI-ACC.

As for POF curvature sensor measurements, the more reliable instants are defined after the maximum flexion at stance phase to the end of mid-swing phase. This interval was identified by previous examination of data. Basically, due to limitations related to the gait dynamics, attachment, and alignment of the experimental-setup with the joint, we observed that during terminal swing, close to the initial contact, the POF curvature sensor output does not track closely the knee movement. This fact will be further discussed in Section 4.5. Note that this interval comprises the gait phases from the end of loading response to complete mid-swing

phase (approximately around 10 - 85% of gait cycle, see Figure 4.3 (c)). We called this interval as RI-POF.

To detect the gait phases of interest, we first implemented a method to identify the two main gait's phases, i.e., stance and swing phases. The method consists of finding the events that indicate the start of each phase, which are heel strike (HS) and toe-off (TO), respectively. For this purpose, we used the angular velocity of the shank's gyroscope medio-lateral axis, and a dual minima method was implemented (LEE; PARK, 2011; KOTIADIS; HERMENS; VELTINK, 2010). Then, by using the knee angular velocity and identifying two zero-crossing (one ascending and other descending) between HS and TO instants of each gait cycle, the RI-ACC interval is defined. To identify approximately the end of the mid-swing (MSw) phase, we used the maximum peak in the knee angular velocity located after the TO instant. Therefore, the RI-POF interval is defined between the first zero-crossing, after HS instant, and the maximum peak, after TO instant, of the knee angular velocity signal. The RI-ACC and RI-POF intervals are graphically explained in Figure 4.3. The implementation of the rule-based method is presented in Algorithm 4 (Appendix A.4).

4.3.3 POF Curvature Sensor

In our research, the POF curvature sensor works based on the intensity variations principle as mentioned in Section 2.2.4. This principle consists of measuring the light power variation on the POF output when it undergoes curvature. Such power variation is proportional to the curvature angle. By removing a section of the fiber cladding and part of its core, a so-called sensitive zone is created (BILRO et al., 2012). This is done aiming to increase the sensor sensitivity and linearity as well as hysteresis reduction. Therefore, this zone is more sensitive to curvature variations. We performed a previous calibration stage of the POF curvature sensor as suggested in (LEAL-JUNIOR et al., 2018b). To fulfill this task, we positioned the POF sensor on the experimental setup shown in Figure 4.4. This setup comprises of a DC servomotor with angular position/velocity closed-loop control, a precision potentiometer and a 3D-printed mechanical structure. Using the control unit, flexion-extension movements were generated on a range of

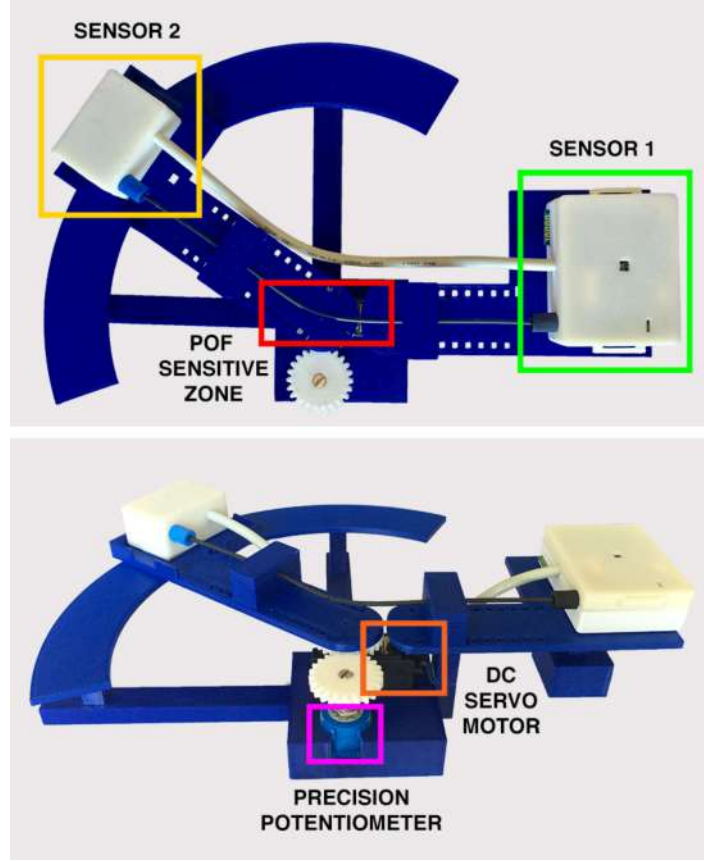


Figure 4.4: Experimental setup for POF curvature sensor characterization

motion of 0 - 90°. The POF curvature sensor output is then compared to the angle measured by the potentiometer. Afterwards, a regression is applied in order to obtain the coefficients y_1 , y_2 , τ_1 and τ_2 of Equation 4.7 as explained in Section 2.2.4.

$$\alpha = y_1 \cdot \exp\left(\tau_1 \left(\frac{P}{P_0}\right)\right) + y_2 \cdot \exp\left(\tau_2 \left(\frac{P}{P_0}\right)\right) + c_0 \quad (4.7)$$

It should be recalled that two equations are needed, one for flexion and one for extension. When the sensor is positioned on the user's knee joint, the new mounting conditions can influence the sensor response, as discussed in (LEAL-JUNIOR; FRIZERA; PONTES, 2018b). Therefore, a calibration movement was required to adjust the characterization parameters. In Section 4.5.1 the results of POF curvature sensor characterization are presented. Now, let θ_{POF} be the resulting angle of the POF curvature sensor. In order to express it in quaternion format, which

feeds the multi-sensor fusion filter in the observation model, Equation 4.8 is used.

$$q_{POF}(\theta_{POF}, \mathbf{j}_2) = \left(\cos\left(\frac{\theta_{POF}}{2}\right), \mathbf{j}_2 \sin\left(\frac{\theta_{POF}}{2}\right) \right), \quad (4.8)$$

where q_{POF} is the rotation quaternion around the joint main axis in the shank sensor's local coordinate frame. Here, we are assuming that the POF curvature sensor is aligned with the knee joint main axis.

4.3.4 IMU-POF Based Multiplicative Extended Kalman Filter (MEKF)

We propose a multi-sensor fusion filter based on MEKF, first introduced by Lefferts, Markley and Shuster (1982), as a method to estimate spacecraft attitude using quaternions. Recently, Ghobadi et al. (2017a) used this formulation to propose a single IMU-based gait monitoring system (GHOBADI; ESFAHANI, 2017b). A MEKF consists of estimating a non-singular and unconstrained orientation error ($\delta\theta$), which is the vector part of the multiplicative error quaternion, $\delta\mathbf{q}$, that is defined as the multiplication between the estimated quaternion conjugate, $\hat{\mathbf{q}}^{-1}$, and the true orientation quaternion, \mathbf{q} , as expressed in Equation 4.9.

$$\delta\mathbf{q} = \hat{\mathbf{q}}^{-1} \otimes \mathbf{q}, \quad (4.9)$$

where the multiplicative error quaternion can be approximated as $\delta\mathbf{q} \approx \begin{bmatrix} 1 & \delta\theta \end{bmatrix}^T$. The main advantage of MEKF with relation to the ordinary EKF is that the error, $\delta\mathbf{q}$, between the estimated and the true orientation, is supposed to be much smaller than the differences with the actual orientation, which eventually leads to a smaller linearization error. As the ordinary EKF, MEKF also works in a two step process: Prediction and Update step, which are explained below.

For nonlinear system, MEKF is described by a state space model for dynamics \mathbf{x}_{k+1} and mea-

surement \mathbf{z}_k as shown in Equation 4.10.

$$\begin{aligned}\mathbf{x}_{k+1} &= f(\mathbf{x}_k) + \mathbf{w} \\ \mathbf{z}_k &= h(\mathbf{x}_k) + \mathbf{v},\end{aligned}\tag{4.10}$$

where $f(\mathbf{x}_k)$ and $h(\mathbf{x}_k)$ are the state transition and measurement functions, respectively. And \mathbf{w} and \mathbf{v} are the additive noises, modeled as a zero-mean white Gaussian noise process with known covariance matrices \mathbf{Q} and \mathbf{R} , respectively.

Joint Kinematics

The relative orientation between the shank and thigh body segments can be obtained by integrating Equation 4.11.

$$\dot{\mathbf{q}}_{TS} = \frac{1}{2} \mathbf{q}_{TS} \otimes \boldsymbol{\omega}_{TS}^S, \tag{4.11}$$

where \mathbf{q}_{TS} is the unit quaternion expressing the orientation of the shank frame with respect to the thigh frame, and $\boldsymbol{\omega}_{TS}^S$ is the angular velocity of the shank with respect to the thigh coordinate system expressed in the shank coordinate system (KORTIER et al., 2015). Moreover, this relative angular velocity, $\boldsymbol{\omega}_{TS}^S$, is calculated by subtracting the angular velocities of two adjacent bodies forming a joint. Recall the angular velocity of a single body is measured by using a 3D gyroscope, whose sensor output, \mathbf{y}_{ω_i} , can be modeled as shown in Equation 4.12. For more details, refer to Section 2.2.1.

$$\mathbf{y}_{\omega_i} = \boldsymbol{\omega}_i + \mathbf{b}_{\omega_i} + \mathbf{w}_{\omega_i}, \tag{4.12}$$

where i refers to the shank (S) or thigh (T) body segments, $\boldsymbol{\omega}_i$ is the angular velocity of the i -th body with respect to a global coordinate system expressed in the body local coordinate system, \mathbf{b}_{ω_i} is the gyro sensor bias of the i -th body and \mathbf{w}_{ω_i} is a zero-mean white Gaussian noise process with standard deviation σ_{ω_i} . Then, the relative angular velocity $\boldsymbol{\omega}_{TS}^S$ can be modeled exploiting the kinematic constraints as shown in Equation 4.13.

$$\boldsymbol{\omega}_{TS}^S = [(\mathbf{y}_{\omega_S} - \mathbf{b}_{\omega_S} - \mathbf{w}_{\omega_S}) \cdot \mathbf{j}_2 - (\mathbf{y}_{\omega_T} - \mathbf{b}_{\omega_T} - \mathbf{w}_{\omega_T}) \cdot \mathbf{j}_1] \mathbf{j}_2, \tag{4.13}$$

where \mathbf{j}_1 and \mathbf{j}_2 are the knee joint axis computed in Section 4.3.1. For simplifying notation and because their values are unitary, the Euclidean norms of \mathbf{j}_1 and \mathbf{j}_2 were omitted in Equation 4.13.

State Space Model and Prediction Step

As already discussed, the filter computes the error state, therefore, the state vector is defined as shown in Equation 4.14.

$$\mathbf{x} = \begin{bmatrix} \delta\boldsymbol{\theta}_{TS} & \delta\mathbf{b}_{\omega_T} & \delta\mathbf{b}_{\omega_S} \end{bmatrix}, \quad (4.14)$$

where $\delta\boldsymbol{\theta}_{TS}$ is the orientation error of the shank with respect to thigh body segments, and $\delta\mathbf{b}_{\omega_T}$ and $\delta\mathbf{b}_{\omega_S}$ are the error bias estimates of the thigh and shank gyroscopes sensors, respectively. It is needed to estimate the gyroscopes bias due to the fact that these sensors have a low bias stability, as previously discussed in Section 2.2.1, which may lead to high inaccuracy orientation estimates by integrating the gyroscopes output over long periods.

Now, let $\hat{\mathbf{q}}_{TS}$ be the expected value of \mathbf{q}_{TS} , which can be also estimated by integrating Equation 4.15.

$$\dot{\hat{\mathbf{q}}}_{TS} = \frac{1}{2} \hat{\mathbf{q}}_{TS} \otimes \hat{\boldsymbol{\omega}}_{TS}^S, \quad (4.15)$$

where $\hat{\mathbf{q}}_{TS}$ and $\hat{\boldsymbol{\omega}}_{TS}^S$ are the estimated relative orientation quaternion and relative angular velocity between the shank and the thigh body segments, respectively. Assuming a zero-order-hold of $\hat{\boldsymbol{\omega}}_{TS}^S$ with a sampling time T , its discretization is shown in Equation 4.16.

$$\hat{\mathbf{q}}_{TS,k} = \exp\left(\frac{1}{2}\boldsymbol{\Omega}(\hat{\boldsymbol{\omega}}_{TS}^S)T\right) \otimes \hat{\mathbf{q}}_{TS,k-1} \quad (4.16)$$

where k is the actual sample and $\boldsymbol{\Omega}(\hat{\boldsymbol{\omega}}_{TS}^S)$ is a matrix as shown in Equation 4.17.

$$\boldsymbol{\Omega}(\boldsymbol{\omega}) = \begin{bmatrix} 0 & -\boldsymbol{\omega}^T \\ \boldsymbol{\omega} & -[\boldsymbol{\omega} \times] \end{bmatrix} \quad [\boldsymbol{\omega} \times] = \begin{bmatrix} 0 & -\omega_3 & \omega_2 \\ \omega_3 & 0 & -\omega_1 \\ -\omega_2 & \omega_1 & 0 \end{bmatrix} \quad (4.17)$$

Also, $\hat{\boldsymbol{\omega}}_{TS}^S$ can be expressed as shown in Equation 4.18 by using the single gyroscope model and the estimated knee joint axis.

$$\hat{\boldsymbol{\omega}}_{TS}^S = \left[\left(\mathbf{y}_{\omega_S} - \hat{\mathbf{b}}_{\omega_S} \right) \cdot \mathbf{j}_2 - \left(\mathbf{y}_{\omega_T} - \hat{\mathbf{b}}_{\omega_T} \right) \cdot \mathbf{j}_1 \right] \mathbf{j}_2. \quad (4.18)$$

Next, by taking the derivative of Equation 4.9 and replacing $\dot{\mathbf{q}}_{TS}$ and $\dot{\hat{\mathbf{q}}}_{TS}$ from Equations 4.11 and 4.15, we can deduce Equation 4.19 to describe the state transition equation. The gyro bias \mathbf{b}_{ω_i} (for $i = T$ or S) is modeled as a random walk process, $\dot{\mathbf{b}}_{\omega_i} = \mathbf{w}_{b_{\omega_i}}$, where $\mathbf{w}_{b_{\omega_i}}$ is a zero-mean white Gaussian noise process with standard deviation $\sigma_{b_{\omega_i}}$.

$$\begin{aligned} \delta \dot{\boldsymbol{\theta}}_{TS} &= - \left[\hat{\boldsymbol{\omega}}_{TS}^S \times \right] \delta \boldsymbol{\theta}_{TS} + \frac{1}{2} \delta \boldsymbol{\omega}_{TS}^S \\ \delta \dot{\mathbf{b}}_{\omega_S}^S &= \mathbf{w}_{b_{\omega_S}} \\ \delta \dot{\mathbf{b}}_{\omega_T}^S &= \mathbf{w}_{b_{\omega_T}} \end{aligned} \quad (4.19)$$

$[\cdot \times]$ is the skew symmetric matrix operator computed using the right side of Equation 4.17. By using Equations 4.13 and 4.18, the difference angular velocity, $\delta \boldsymbol{\omega}_{TS}^S$, is computed as shown in Equation 4.20. For $\|\delta \boldsymbol{\omega}_{TS}^S\| \ll \|\hat{\boldsymbol{\omega}}_{TS}^S\|$ and $\|\mathbf{b}_{\omega_i}\| \ll 1$, Equation 4.20 was simplified neglecting the projections of the biases and recalling that such biases are estimated in each iteration.

$$\begin{aligned} \delta \boldsymbol{\omega}_{TS}^S &= \boldsymbol{\omega}_{TS}^S - \hat{\boldsymbol{\omega}}_{TS}^S \\ \delta \boldsymbol{\omega}_{TS}^S &= \delta \mathbf{b}_{\omega_T}^S - \delta \mathbf{b}_{\omega_S}^S - \mathbf{w}_{\omega_{TS}}^S \\ \delta \mathbf{b}_{\omega_i}^S &= \mathbf{b}_{\omega_i}^S - \hat{\mathbf{b}}_{\omega_i}^S \\ \mathbf{w}_{\omega_{TS}}^S &= (\mathbf{w}_{\omega_S} \cdot \mathbf{j}_2 - \mathbf{w}_{\omega_T} \cdot \mathbf{j}_1) \mathbf{j}_2 \end{aligned} \quad (4.20)$$

Before measurement update, error states are set to zero (KORTIER et al., 2015; GHOBADI; ESFAHANI, 2017a) and the error covariance matrix, P , is propagated using the discretization process model, F_d , and process noise, Q_d , similar to those proposed in (GHOBADI; ESFAHANI, 2017a), as shown in Equation 4.21, where the minus sign indicates the a-priori estimate.

$$P_k^- = F_{d,k} P_{k-1} F_{d,k}^T + Q_d, \quad (4.21)$$

Observation Model and Update Step

During the update step, as proposed in (GHOBADI; ESFAHANI, 2017a), the error covariance, P , and filter states, \mathbf{x} , are corrected twice, first using the accelerometers' outputs and then the POF curvature sensor's. For the accelerometers, consider two vectors, \mathbf{a}_T and \mathbf{a}_S , which are the acceleration vectors computed in Section 4.3.1. Now, the estimate of \mathbf{a}_T in the local coordinate S is given by Equation 4.22. Note that the two vectors are related by \mathbf{q}_{TS} , which is the orientation quaternion that represents the knee joint angle.

$$\hat{\mathbf{a}}_S = (\hat{\mathbf{q}}_{TS})^{-1} \otimes \mathbf{a}_T \otimes \hat{\mathbf{q}}_{TS} \quad (4.22)$$

We can also express Equation 4.22 in matrix form using Equation 4.23.

$$\hat{\mathbf{a}}_S = M(\hat{\mathbf{q}}_{TS})\mathbf{a}_T, \quad (4.23)$$

where $M(\mathbf{q})$ is computed using Equation 4.24. In addition, note that $M(\mathbf{q})$ is the inverse rotation.

$$M(\mathbf{q}) = 2 \begin{bmatrix} q_0^2 + q_1^2 + \frac{1}{2} & q_1q_2 + q_0q_3 & q_1q_3 - q_0q_2 \\ q_1q_2 - q_0q_3 & q_0^2 + q_2^2 - \frac{1}{2} & q_2q_3 + q_0q_1 \\ q_1q_3 + q_0q_2 & q_2q_3 - q_0q_1 & q_0^2 + q_3^2 - \frac{1}{2} \end{bmatrix} \quad (4.24)$$

Moreover, Equation 4.9 can be expressed in matrix form by Equation 4.25. $M(\delta\mathbf{q})$ can be approximated as shown in Equation 4.26 (GHOBADI; ESFAHANI, 2017a), where I is the identity matrix.

$$M(\mathbf{q}) = M(\delta\mathbf{q})M(\hat{\mathbf{q}}) \quad (4.25)$$

$$M(\delta\mathbf{q}) = I - 2[\delta\boldsymbol{\theta} \times] \quad (4.26)$$

Then, the difference between the observed, \mathbf{a}_S , and the estimated vector, $\hat{\mathbf{a}}_S$, should be related to the error state, $\delta\boldsymbol{\theta}_{TS}$, as shown in Equation 4.27. Note that the observed vector is augmented by a measurement error, \mathbf{v}_a , which is a zero-mean white Gaussian noise process with standard

deviation σ_a .

$$\begin{aligned}\delta \mathbf{z}_a &= \mathbf{a}_S - \hat{\mathbf{a}}_S \\ \delta \mathbf{z}_a &= 2 [\hat{\mathbf{a}}_S \times] \delta \boldsymbol{\theta}_{TS} + \mathbf{v}_a\end{aligned}\tag{4.27}$$

Consequently, the observation model corresponding to the correction by the accelerometers is expressed in Equation 4.28.

$$H_{a_d,k} = \begin{bmatrix} 2 [\hat{\mathbf{a}}_S \times] & \mathbf{0}_{3 \times 3} & \mathbf{0}_{3 \times 3} \end{bmatrix}\tag{4.28}$$

Regarding the correction by the POF curvature sensor, we proposed to use Equation 4.9, where the orientation quaternion, \mathbf{q}_{POF} , computed in Section 4.3.3, is assumed to be the true orientation quaternion. Then, we can express the error quaternion as shown in Equation 4.29.

$$\delta \mathbf{q}_P = (\hat{\mathbf{q}}_{TS,k})^{-1} \otimes \mathbf{q}_{POF}\tag{4.29}$$

Because $\delta \mathbf{q}_P$ is supposed to be small, the difference between the observed quaternion, \mathbf{q}_{POF} , and the estimated quaternion $\hat{\mathbf{q}}_{TS,k}$ is the vector part of $\delta \mathbf{q}_P$, which is defined as $\delta \boldsymbol{\theta}_{POF}$. This should be related to the error state as shown in Equation 4.30.

$$\begin{aligned}\delta \mathbf{z}_{POF} &= \delta \boldsymbol{\theta}_{POF} \\ \delta \mathbf{z}_{POF} &= \delta \boldsymbol{\theta}_{TS} + \mathbf{v}_{POF},\end{aligned}\tag{4.30}$$

where \mathbf{v}_{POF} is the POF curvature sensor's measurement noise, which is modeled as a zero-mean white Gaussian noise process with standard deviation σ_{POF} . Subsequently, the observation model corresponding to the correction by POF curvature sensor is expressed in Equation 4.31.

$$H_{POF_d,k} = \begin{bmatrix} I_{3 \times 3} & \mathbf{0}_{3 \times 3} & \mathbf{0}_{3 \times 3} \end{bmatrix}\tag{4.31}$$

The update step is also applied twice using Kalman filter equations, in which the Kalman gain, K_k , is computed and the state \mathbf{x}_k along with its covariance P_k are also updated as shown in

Equation 4.32.

$$\begin{aligned} K_k &= P_k^- H_{i_d,k}^T \left[H_{i_d,k} P_k^- H_{i_d,k}^T + R_{i,k} \right] \\ P_k^+ &= \left[I - K_k H_{i_d,k} \right] P_k^- \\ \hat{\mathbf{x}}_k^+ &= \hat{\mathbf{x}}_k^- + K_k \left[\delta \mathbf{z}_i - H_{i_d,k} \hat{\mathbf{x}}_k^- \right], \end{aligned} \quad (4.32)$$

where i refer to a or POF . The plus and minus signs indicate the a-posteriori and a-priori estimate, respectively. Before each update step, the reliability of the accelerometers and POF curvature sensor signals is assessed as explained in Section 4.3.2. In this way, the measurement covariance matrices, $R_{i,k}$, are adapted such that their scale considering the intervals RI-ACC and RI-POF as previously defined. We considered to adapt these covariances matrices as suggested by Sabatini (2011), where measurement vectors are discarded by setting the variances to some large values.

Finally, the filter updates the orientation quaternion, $\hat{\mathbf{q}}_{TS,k}$, and the biases, $\hat{\mathbf{b}}_{\omega_i,k}$, by using Equation 4.33, where $\delta \mathbf{q}_{TS} = [1 \ \delta \boldsymbol{\theta}_{TS}]$.

$$\begin{aligned} \hat{\mathbf{q}}_{TS}^+ &= \hat{\mathbf{q}}_{TS}^- \otimes \delta \mathbf{q}_{TS}, \quad \hat{\mathbf{q}}_{TS} = \frac{\hat{\mathbf{q}}_{TS}}{\|\hat{\mathbf{q}}_{TS}\|} \\ \hat{\mathbf{b}}_{\omega_i,k} &= \hat{\mathbf{b}}_{\omega_i,k-1} + \delta \mathbf{b}_{\omega_i} \end{aligned} \quad (4.33)$$

Then, the knee angle is computed using Equation 4.34, with $s = \frac{\mathbf{q}_{TSz}}{\mathbf{j}_{2z}}$ and $c = \mathbf{q}_{TSw}$, where z and w refer to the element vector.

$$\theta_{knee} = 2 \cdot \text{atan} \left(\frac{s}{c} \right) \quad (4.34)$$

The implementation of the IMU-POF based MEKF is summarized in Algorithm 5 (Appendix A.5). A flowchart is also presented in Appendix A.7.

4.4 Experiments

This section presents the experimental evaluation and validation of the knee sleeve system. Ground truth data from experiments with healthy subjects was provided by an optical gait

analysis system, enabling the validation of the proposed system and algorithms. Experimental protocol, data and statistical analyzes are presented using different metrics in order to assess reliability and repeatability.

4.4.1 Participants

Twelve healthy young adults (males) without history of neuromuscular or physical disability participated in this study (23.08 ± 2.31 years old; 1.72 ± 0.05 m; 71.32 ± 9.91 kg). Prior to participating in this study, all subjects (S1 to S12) were informed about the study protocol and gave their informed consent. The ethics committee of the Colombian School of Engineering Julio Garavito approved all study procedures (02-2019).

4.4.2 Protocol

An 8-camera optical motion capture system (Vantage V5-Wide, Vicon, USA) was used as a gold-standard, with a sampling rate of 100 Hz. We placed a total of fifteen passive reflective markers on anatomical landmarks (pelvis, thigh, leg and foot for both sides) according to the Plug-in-Gait Lower Body specifications (VICON, 2016). A single sacral marker was used for the pelvis. Additionally, marker clusters were placed on pelvis, right thigh and leg, and both feet in order to improve tracking and estimates. Next, the instrumented part of the knee sleeve system was placed on the participant's joint (see Figure 4.5). This was done in such a way that the sensitive zone of the optical fiber was carefully aligned with the knee flexion rotation axis. Textile knee sleeve was not used seeking to avoid any marker misplacement errors by this fact. Two 3D-printed supports were used mimicking the seams on the knee sleeve. To synchronize the systems, a trigger signal was sent by the commercial system to the proposed system.

Before each test, anthropometric measurements (weight, height, inter-ASIS distance, leg length, knee width, and ankle width) were collected from each subject. A calibration trial was performed at the beginning of the test in order to verify if the optical system was working appropriately. This capture was also needed for data processing. Thus, participants were asked to



Figure 4.5: Marker set (Plug-in Gait lower body model), additional marker clusters and IMU-POF system placed on a participant.

keep a static upright posture for approximately 5 seconds in the middle of the room. Afterward, they were addressed to perform a passive knee flexion-extension movement in a standing posture in order to collect data to characterize the POF curvature sensor.

Participants performed eight walking trials at self-selected speed along an 8.5 meters walkway of which approximately 4 meters into the zone captured by the optical system. The number of trials was chosen in order to obtain at least 20 gait cycles for each participant.

The start and the end of the walkway was indicated through marks on the floor using crepe tape. In addition, all participants were asked to start walking with their right leg in each trial. We used Nexus 2.8 software (Vicon, USA) for data processing from the optical system. MATLAB software (version 2018a; The MathWorks Inc., USA) was used to develop the algorithms, analyze and process the orientation data from the knee sleeve system.

4.4.3 Data Analysis

We analyzed and compared whole knee flexion-extension angle curves. For each participant, 20 gait cycles were collected with each system. A total of 240 knee flexion-extension angle signals was processed for each system.

First, the Conventional Gait Model 1 (CGM1, Vicon) was adjusted to include the marker clusters. Next, marker trajectories' reconstruction and auto-labelling were carried out in Nexus software (Vicon). Then, each trial was visually examined in order to verify the consistency of the assigned labels. Gaps, due to markers occlusion, were interpolated according to the gap sizes: (i) gaps in trajectories not greater than 10 samples were estimated using a Woltring filter, (ii) gaps in trajectories of up to 25 samples were estimated by means of the rigid body property, and the not-occluded markers associated with the segment representing the rigid body under evaluation. Greater gaps were not allowed. Kinematics (joint angles and positions) were calculated using the Plug-in Gait pipeline and exported in a c3d file. The identification of the gait events, heel strike and toe off, were realized manually.

Data from the knee sleeve system were filtered with a 4th order Butterworth filter with a 10 Hz cutoff. Initial gyroscope offsets were removed by subtracting the average value of the static sensor outputs at the beginning of each trial. Accelerometer signals were also normalized during static posture. Then, all methods presented in Section 4.3 were applied to estimate the knee joint angles. Each gait cycle was extracted using two consecutive heel strike (HS) events, as explained in Section 4.3.2.

4.4.4 Statistical Analyses

We evaluated the proposed methods and system in two scenarios:

1. Comparing the knee angles estimated when (i) using the gyroscopes, accelerometers and POF curvature sensors separately, (ii) merging signals from gyroscopes and accelerometers, and

- (iii) using the proposed IMU-POF based MEKF. A 4th-order Runge-Kutta (RK4) algorithm was used for numerical time-integration when using only gyroscopes.
- 2. Comparing the obtained results with three methods in the literature (SEEL; RAISCH; SCHAUER, 2014; MCGRATH; FINEMAN; STIRLING, 2018; ALLSEITS et al., 2018).

In the first method (SEEL; RAISCH; SCHAUER, 2014), the authors used a complementary filter (CF) to fusion data from gyroscopes and accelerometer using the joint axis and positions, as explained in Section 4.3.1. The second method consists of estimating the knee flexion-extension axis using Principal Component Analysis (PCA) (MCGRATH; FINEMAN; STIRLING, 2018). In the third method, the authors proposed to estimate the knee angle using the integration of the knee angular velocity based on a gyroscope only (GO) algorithm, along with a zero angle update (Zero Knee Angle, ZKA) for eliminating the drift due to integration (ALLSEITS et al., 2018).

Three metrics were calculated aiming to describe the performance of the proposed methods and system when compared to the gold-standard system: (i) Root Mean Square Error (RMSE) (BERGAMINI et al., 2014), (ii) Linear Fit Method (LFM) coefficients (IOSA et al., 2014), and (iii) Concordance Correlation Coefficient (CCC) (LAWRENCE; LIN, 1989). They were used in order to express reliability and repeatability of the obtained patterns along whole gait cycles.

The LFM consists of three coefficients: a_1 represents the amplitude scaling factor between the comparing curves, greater similarity is presented when a_1 is closer to 1; a_0 predicts the scalar addition (shift) between curves, corresponding to the offset, when a_1 tends to 1, ideally a_0 is equal to zero; and R^2 measures the strength of the linear relationship between curves, and coincides with the square of the Pearson's correlation coefficient R . In addition, CCC (ρ_c) is the relation between C_b , the bias correction factor that measures how far the best-fit line deviates from the 45° line, which measures accuracy; and R , which measures precision.

Moreover, the normal distribution of the indices was verified using the Shapiro-Wilk test of

normality. The distribution of all indices was found to be normal. Then, we carried out a repeated measures one-way ANOVA for each dependent variable. The Maunchly test was used to check sphericity assumption, if this assumption was not confirmed, the Greenhouse-Geisser adjustment was used. If significant p -value was found, we used a pairwise comparison *post-hoc* test. We also computed the effect size, partial η squared (η^2) parameter, for each dependent variable. The level of significance was set at $\alpha < 0.05$. We used IBM SPSS Statistics software (IMB SPSS Statistics 20, SPSS IBM, New York, NY, USA) to perform statistical analysis.

4.5 Results and Discussion

4.5.1 POF Curvature Sensor Characterization

The average of twenty flexion-extension movements was used to characterize the POF curvature sensor with an angular velocity of approximately 1.5 rad/s. Figure 4.6 (a) depicts the angle estimated by the POF curvature sensor after a characterization using a compensation technique (Equation 4.7) and the experimental setup shown in Figure 4.4. The comparison between the compensated and uncompensated responses is presented in Figure 4.6 (c-d). The mean hysteresis, when the compensation technique is applied, decreased from 1.88% to 0.74%. In addition, note that the mean RMSE obtained when compared the POF response to the potentiometer output decreased from 4.36° to 2.57° . After the POF curvature sensor is positioned on the participants's knee joint, the characterization parameters are adjusted during the calibration trial. The results of one gait trial are presented in Figure 4.6 (b) for the participant S9. The mean RMSE obtained for these three gait cycles was 6.11° .

Additionally, it is possible to observe that the difference between the POF response and the reference system increased around the initial contact with a value of up to 18° . This response pattern of the POF curvature sensor was repeatable for all participants, in some cases more critical than others. After the maximum knee flexion, which also represents the maximum deformation of the POF sensor, the knee undergoes a rapid extension during mid and terminal

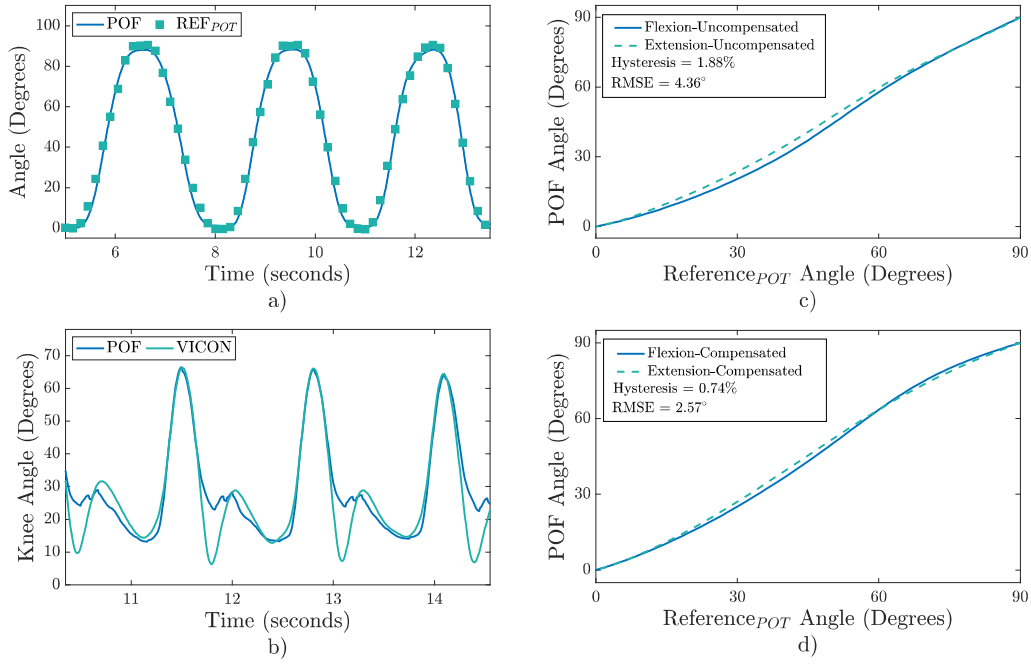


Figure 4.6: POF curvature sensor characterization. (a) Estimated angle by POF curvature sensor in three sequential flexion/extension cycles compared to the reference potentiometer. (b) POF curvature sensor-based knee joint angle compared with the reference camera-based system during walking. POF sensor response before (c) and after (d) applying the compensation technique using the experimental setup.

swing. The angular velocity in this interval is directly proportional to the gait velocity and can vary from 3 to 6.5 rad/s (MENTIPLAY et al., 2018). Thus, the POF sensor suffers a high angular variation in a reduced time interval, which influences the viscoelastic response of the polymer (LEAL-JUNIOR et al., 2018c), explaining one of the possible causes of why the POF sensor response does not track closely the knee movements after the maximum flexion. In addition, the experimental setup conditions, such as the bending radius and a misalignment between the POF sensor and knee joint, can also affect the sensor output (LEAL-JUNIOR; FRIZERA; PONTES, 2018b).

The results expose an evidence that the POF sensor performance decreases when used alone to assess knee joint movements without rigid structures. However, similar sensors have demonstrated high accuracy ($RMSE < 4^\circ$) as well as a good repeatability for robotic exoskeleton applications (LEAL-JUNIOR et al., 2017, 2018) and soft-robotics (LUNNI et al., 2018). More-

over, advantages such as low-cost, lightweight, multiplexing systems and electromagnetic field immunity make POF sensors attractive for these applications.

For wearable sensors, side rigid structures bounding the POF sensor should be used to prevent sideways stress, or include the sensor as part of the textile, which should ideally be adhered well to the skin. Moreover, an alternative to improve the system performance is to fusion the POF sensor output with IMU sensors data, benefiting from both technologies. This last approach is proposed and implemented in this work.

4.5.2 Comparison of Single-sensor and Multi-sensor Fusion Methods

This subsection aims to evaluate the repeatability and reproducibility of five methods based on single-sensor or multi-sensor-fusion measurements when used to estimate the knee joint angle. In addition, a statistical comparison between them is presented. Each knee flexion-extension angle estimated by the wearable system was compared with that obtained by the optical system. Parameters of process and measurement noise distributions are given in Table 4.1. These values were determined empirically and following suggestions from other studies (XING; GEBRE-EGZIABHER, 2008). Knee angle signals from twelve healthy young adults (S1 to S12) were processed and analyzed. The accuracy of each method was expressed using the Root Mean Square Error (RMSE) and the obtained results are shown in Table 4.2. The three first columns correspond to the single-sensor methods: gyroscope-based, accelerometer-based and POF-based methods. The fourth column refers to the gyroscopes and accelerometers fusion method using our MEKF, and the last one corresponds to the fusion of signals from IMUs and POF curvature sensor through MEKF. The smallest mean RMSE value for each subject is highlighted in bold.

Table 4.1: Standard deviation values of gyroscopes, gyro biases, accelerometers and POF curvature sensor noise.

σ	$\mathbf{v_a} \text{ (m/s}^2\text{)}$	$\mathbf{w_\omega} \text{ (rad/s)}$	$\mathbf{w_{b\omega}} \text{ (rad/s)}$	$\mathbf{v_{POF}} \text{ (degrees)}$
	5×10^{-1}	5×10^{-3}	1×10^{-3}	5×10^{-3}

These parameters were empirically found.

Table 4.2: Methods vs. gold standard, accuracy expressed in terms of Root Mean Square Error (RMSE).

RMSE: Mean (SD) (Degrees)					
Participant	RK4 INT Method (Gyroscope)	Accelerometer- based Method	POF-based Method	Gyro + Acc Fusion (MEKF Method)	Gyro + Acc + POF Fusion (MEKF Method)
S1	5.00 (1.20)	19.35 (0.98)	7.52 (1.15)	4.30 (0.72)	3.46 (0.62)
S2	9.98 (3.36)	14.14 (1.69)	7.62 (0.89)	4.12 (0.61)	3.56 (0.48)
S3	6.40 (2.27)	21.49 (1.61)	6.80 (0.67)	3.93 (1.15)	2.49 (0.75)
S4	7.19 (3.06)	13.46 (1.47)	6.19 (0.43)	3.80 (1.07)	1.89 (0.54)
S5	11.56 (2.18)	16.82 (0.94)	8.53 (1.49)	3.42 (1.45)	3.21 (1.53)
S6	8.74 (6.04)	16.80 (1.03)	8.19 (0.55)	4.17 (1.43)	2.94 (0.98)
S7	11.62 (4.00)	11.69 (1.25)	8.23 (0.73)	5.90 (0.99)	3.63 (0.98)
S8	6.01 (1.34)	15.40 (1.04)	6.17 (0.45)	4.02 (0.62)	2.98 (0.64)
S9	14.30 (4.49)	12.72 (0.92)	5.82 (0.71)	5.53 (1.17)	4.16 (0.68)
S10	4.46 (2.17)	12.53 (1.12)	9.48 (1.27)	3.84 (0.68)	1.83 (0.47)
S11	4.80 (1.20)	18.06 (1.86)	6.53 (0.41)	6.46 (1.04)	4.40 (0.90)
S12	6.61 (1.87)	14.53 (0.93)	8.71 (0.60)	9.92 (0.90)	3.80 (0.76)
Mean	8.87	15.45	7.59	5.12	3.28
SE	0.92	0.86	0.34	0.46	0.24

For each participant values are presented as Mean (SD); SD, standard deviation; SE, standard error; RK4 INT, Runge-Kutta 4th-Ord time-integration method; POF, polymeric optical fiber; Gyro, gyroscope; Acc, accelerometer; MEKF, multiplicative extended kalman filter.

In general, for our IMU+POF based system, a mean RMSE smaller than 4.5° was obtained for each participant. In Figure 4.7 the worst case for each method is shown. A significant difference between methods was observed for RMSE values ($F_{2,22} = 52.65$, $p < 0.0005$, $\eta^2 = 0.83$). *Post-hoc* tests revealed significant difference between accelerometer-based and the other single-sensor and multi-sensors fusion methods ($p < 0.0005$), whereas no difference was found between Gyro-based (RK4-INT) and POF-based methods. Also, mean RMSE of our IMU+POF based sensor fusion (mean RMSE $< 3.3^\circ$ for all participants) was significant smaller than the other methods ($p < 0.001$) (see Figure 4.8 (a)).

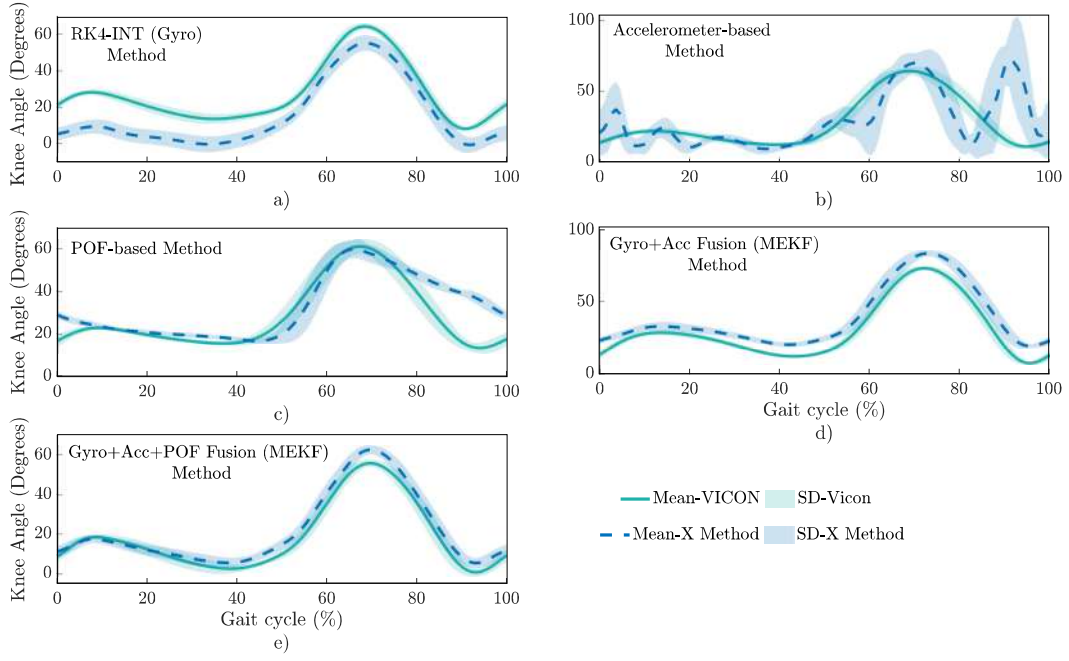


Figure 4.7: The worst case among 12 subjects (S1-S12) for each method when comparing with the reference system. (a) S9, (b) S3, (c) S10, (d) S12 and (e) S11.

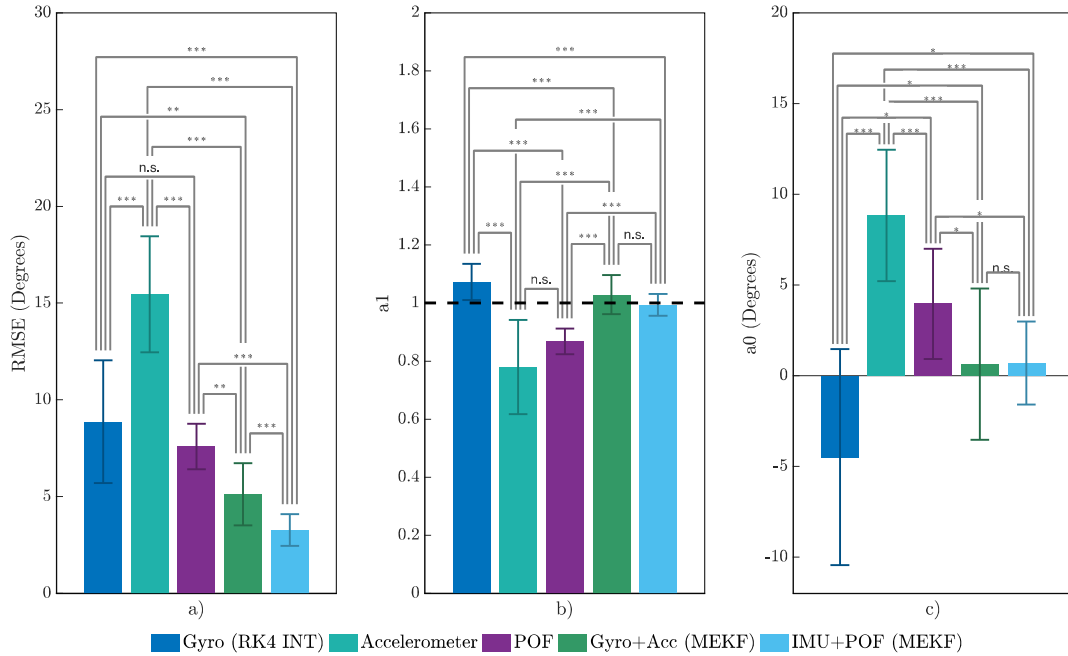


Figure 4.8: Performance of single-sensor and multi-sensor fusion methods. Mean and standard deviation of (a) RMSE, and LFM coefficients (b) a_1 and (c) a_0 . n.s, non-significant p-value > 0.05 , * $p < 0.05$, ** $p < 0.01$, *** $p < 0.001$.

The repeatability and reproducibility of each method were evaluated using the LFM and the CCC coefficients (see Table 4.3 and 4.4). For a_1 (LFM) coefficient, a significant difference between methods was found ($F_{1,16} = 26.09$, $p < 0.0005$, $\eta^2 = 0.70$). According to the *post-hoc* comparisons, non-significant difference was found for two pairwise: Accelerometer-based and POF-based; and Gyro+Acc and IMU+POF MEKF methods. For the others pairwise, significant difference was found ($p < 0.001$) (see Figure 4.8 (b)).

Table 4.3: Methods vs. gold standard, repeatability and reproducibility expressed in terms of the Linear Fit Method (LFM).

Linear Fit Method (LFM) coefficients: Mean (SD)															
Participant	RK4 INT Method (Gyroscope)			Accelerometer-based Method			POF-based Method			Gyro + Acc Fusion (MEKF Method)			Gyro + Acc + POF Fusion (MEKF Method)		
	a_1	$a_0(^{\circ})$	R^2	a_1	$a_0(^{\circ})$	R^2	a_1	$a_0(^{\circ})$	R^2	a_1	$a_0(^{\circ})$	R^2	a_1	$a_0(^{\circ})$	R^2
S1	0.99 (0.02)	-0.41 (3.04)	0.96 (0.01)	1.13 (0.04)	6.55 (1.51)	0.64 (0.04)	0.93 (0.04)	-0.54 (1.55)	0.87 (0.03)	0.98 (0.02)	4.41 (0.81)	0.99 (0.01)	0.97 (0.02)	3.63 (0.69)	0.99 (0.01)
S2	1.14 (0.03)	4.02 (3.66)	0.97 (0.01)	0.71 (0.08)	10.51 (2.62)	0.53 (0.09)	0.89 (0.09)	2.48 (4.73)	0.87 (0.02)	1.12 (0.03)	-1.95 (1.24)	0.98 (0.00)	1.05 (0.03)	-3.06 (1.27)	0.98 (0.00)
S3	1.10 (0.03)	-5.24 (4.77)	0.98 (0.01)	0.64 (0.07)	11.53 (2.32)	0.24 (0.06)	0.85 (0.03)	5.16 (2.04)	0.86 (0.02)	1.04 (0.03)	1.83 (1.84)	0.99 (0.00)	0.97 (0.04)	2.05 (2.08)	0.99 (0.00)
S4	1.03 (0.02)	4.78 (4.01)	0.99 (0.00)	0.65 (0.05)	12.05 (1.32)	0.49 (0.06)	0.89 (0.04)	4.12 (1.50)	0.88 (0.02)	0.97 (0.02)	4.03 (1.31)	0.99 (0.00)	0.99 (0.02)	-0.43 (1.21)	0.99 (0.00)
S5	1.07 (0.05)	-12.41 (2.96)	0.97 (0.05)	0.68 (0.08)	11.23 (1.90)	0.40 (0.05)	0.83 (0.05)	7.05 (2.15)	0.81 (0.05)	0.97 (0.04)	0.60 (2.07)	0.98 (0.03)	0.98 (0.04)	0.88 (1.87)	0.99 (0.04)
S6	1.05 (0.02)	-3.64 (7.99)	0.99 (0.01)	0.83 (0.09)	6.65 (1.12)	0.54 (0.07)	0.84 (0.04)	3.43 (2.08)	0.85 (0.02)	0.99 (0.02)	3.37 (1.79)	0.99 (0.01)	1.00 (0.02)	1.46 (1.66)	0.99 (0.01)
S7	1.00 (0.03)	-10.71 (4.08)	0.99 (0.01)	0.83 (0.04)	2.39 (1.08)	0.71 (0.06)	0.89 (0.05)	0.13 (1.91)	0.87 (0.04)	0.94 (0.03)	-3.77 (1.09)	0.99 (0.01)	0.98 (0.03)	-1.99 (1.21)	0.99 (0.01)
S8	1.21 (0.03)	-8.94 (2.81)	0.97 (0.01)	0.86 (0.09)	4.88 (3.15)	0.45 (0.08)	0.85 (0.04)	3.20 (2.49)	0.87 (0.02)	1.16 (0.03)	-3.82 (1.39)	0.98 (0.01)	1.03 (0.04)	-2.11 (1.42)	0.98 (0.01)
S9	1.04 (0.04)	-12.86 (4.93)	0.88 (0.02)	0.66 (0.08)	9.03 (2.20)	0.47 (0.06)	0.93 (0.06)	2.46 (2.91)	0.88 (0.03)	1.06 (0.04)	-5.38 (2.03)	0.95 (0.01)	0.93 (0.05)	2.64 (2.55)	0.95 (0.02)
S10	1.04 (0.02)	-4.13 (2.88)	0.99 (0.01)	0.55 (0.07)	14.61 (1.72)	0.42 (0.08)	0.78 (0.04)	10.15 (1.74)	0.71 (0.06)	0.99 (0.02)	-3.25 (1.03)	0.99 (0.00)	0.99 (0.02)	-0.50 (1.16)	0.99 (0.00)
S11	1.12 (0.02)	0.14 (2.30)	0.98 (0.01)	0.85 (0.06)	11.16 (0.95)	0.46 (0.05)	0.89 (0.03)	2.68 (1.74)	0.86 (0.01)	1.08 (0.02)	4.04 (1.56)	0.98 (0.00)	1.06 (0.02)	2.10 (1.68)	0.98 (0.00)
S12	1.07 (0.03)	-4.46 (5.01)	0.96 (0.02)	0.96 (0.05)	5.39 (1.40)	0.65 (0.04)	0.85 (0.03)	7.19 (1.87)	0.82 (0.02)	1.03 (0.04)	7.54 (1.83)	0.98 (0.01)	0.96 (0.02)	3.68 (1.78)	0.98 (0.00)
Mean	1.07	-4.49	0.97	0.78	8.83	0.52	0.87	3.96	0.85	1.03	0.64	0.98	0.99	0.70	0.98
SD	0.06	5.95	0.03	0.16	3.62	0.13	0.04	3.04	0.05	0.07	4.17	0.01	0.04	2.29	0.01
Mean (abs(a_0))	-	5.98	-	-	8.83	-	-	4.05	-	-	3.66	-	-	2.04	-
SD (abs(a_0))	-	4.28	-	-	3.62	-	-	2.91	-	-	1.78	-	-	1.10	-

For each participant values are presented as Mean (SD); SD, standard deviation; abs, absolute value; RK4 INT, Runge-Kutta 4th-Ord time-integration method; POF, polymeric optical fiber; Gyro, gyroscope; Acc, accelerometer; MEKF, multiplicative extended kalman filter; a_1 , angular coefficient, which represents the amplitude scaling factor; a_0 , intercept of the fitting line, which represents the scalar addition (shift); R^2 , coefficient of determination, which coincides with the square of the Pearson's correlation coefficient R . Ideal values of LFM parameters are $a_1 = 1$, $a_0 = 0$, $R^2 = 1$.

Table 4.4: Methods vs. gold standard, reproducibility expressed in terms of the Concordance Correlation Coefficient (CCC).

CCC (ρ_c): Mean (SD)					
Participant	RK4 INT Method (Gyroscope)	Accelerometer- based Method	POF-based Method	Gyro + Acc Fusion (MEKF Method)	Gyro + Acc + POF Fusion (MEKF Method)
S1	0.97 (0.02)	0.70 (0.03)	0.93 (0.02)	0.98 (0.01)	0.98 (0.00)
S2	0.89 (0.06)	0.72 (0.06)	0.91 (0.02)	0.98 (0.00)	0.98 (0.00)
S3	0.94 (0.04)	0.48 (0.06)	0.92 (0.01)	0.98 (0.01)	0.99 (0.01)
S4	0.93 (0.06)	0.64 (0.09)	0.93 (0.01)	0.97 (0.01)	0.99 (0.00)
S5	0.84 (0.05)	0.62 (0.04)	0.88 (0.04)	0.98 (0.02)	0.98 (0.02)
S6	0.91 (0.11)	0.71 (0.06)	0.92 (0.02)	0.98 (0.01)	0.99 (0.01)
S7	0.86 (0.07)	0.80 (0.09)	0.92 (0.02)	0.96 (0.02)	0.98 (0.01)
S8	0.92 (0.05)	0.64 (0.06)	0.92 (0.01)	0.97 (0.01)	0.98 (0.01)
S9	0.73 (0.12)	0.68 (0.05)	0.94 (0.02)	0.95 (0.02)	0.97 (0.01)
S10	0.96 (0.05)	0.64 (0.06)	0.81 (0.04)	0.97 (0.01)	0.99 (0.00)
S11	0.95 (0.05)	0.61 (0.04)	0.90 (0.06)	0.94 (0.02)	0.98 (0.02)
S12	0.94 (0.05)	0.77 (0.08)	0.88 (0.05)	0.92 (0.03)	0.98 (0.01)

For each participant, values are presented as Mean (SD); ρ_c , concordance correlation coefficient (Lin's index); SD, standard deviation; RK4 INT, Runge-Kutta 4th-Ord time-integration method; POF, polymeric optical fiber; Gyro, gyroscope; Acc, accelerometer; MEKF, multiplicative extended kalman filter.

Furthermore, for a_0 (LFM) coefficient, a significant difference between methods was found ($F_{2,26} = 22.18$, $p < 0.0005$, $\eta^2 = 0.67$). *Post-hoc* tests revealed non-significant difference between Gyro+Acc and IMU+POF methods, for the others pairwise, significant difference was found ($p < 0.05$) (see Figure 4.8 (c)).

The coefficient of determination, R^2 (LFM) and ρ_C (CCC), are summarized for all participants in Figure 4.9. Also, we used Z-transform for describing the confidence interval (95%) of ρ_C . Mean R^2 values were higher than 0.85 for almost all methods, except for accelerometer-based method ($R^2 = 0.52$), suggesting that 3D accelerometers presented poor performance when

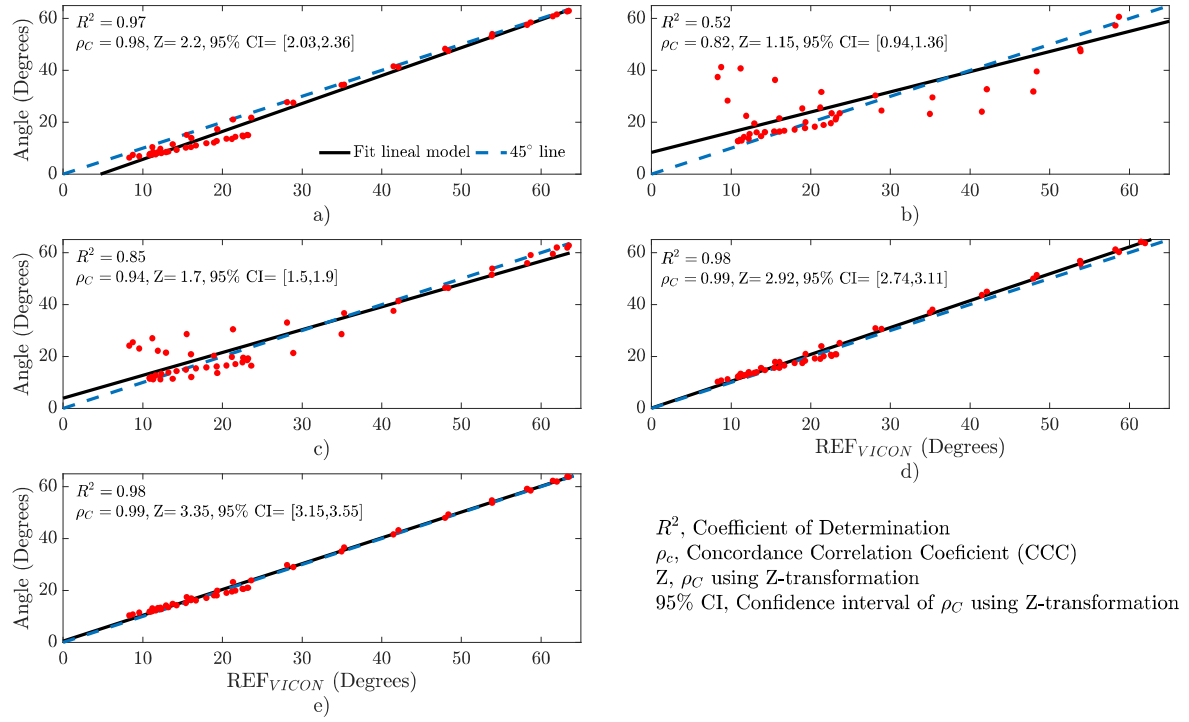


Figure 4.9: Repeatability and reproducibility of (a) Gyro-based method, (b) Accelerometer-based method, (c) POF-based method, (d) Gyro+Acc fusion (MEKF) method and (e) IMU+POF fusion (MEKF) method. Mean R^2 and ρ_C for all participants. Specific Method versus reference system.

used alone for assessing knee angle during walking in this research. Non-significant difference between multi-sensor fusion methods was found. Controversially, significant difference between Gyro-based and both multi-sensors methods was presented ($p < 0.05$). Moreover, ρ_C values were higher than 0.90 for almost all methods, except for accelerometer-based methods ($\rho_C = 0.82$). Values of this parameter are highly influenced by the number of samples of signals to compare (LAWRENCE; LIN, 1989). Excellent agreement between both multi-sensor fusion methods and the gold-standard was found ($\rho_C = 0.99$).

Methods Comparison

In this comparison scenario, three single-sensor and two multi-sensors fusion methods were used to assess the knee flexion-extension angle. The five methods were compared by analyzing their level of accuracy (RMSE), repeatability and reproducibility (LFM coefficients and CCC) using

a camera-based motion capture system (Vicon) as gold-standard.

Average of the knee flexion-extension angle errors were lower than 5.2° for both multi-sensor fusion methods (Gyro+Acc and IMU+POF based MEKF), however, for our IMU+POF based MEKF, the mean RMSE was significant lower ($< 3.3^\circ$ for all participants), which reveals a performance improvement, once the POF curvature sensor is used. Moreover, these findings demonstrate the potential of using complementary sensors, since their mean RMSE values individually were higher than 7.5° .

An approximated mean RMSE was obtained by using a similar system during walking (about 4°) (LEAL-JUNIOR et al., 2018), however, rigid structures (exoskeletons) were positioned on the participants, and the reference measurements were provided by an encoder. In another study (BILRO et al., 2011), the authors presented the knee angle measured by a similar single POF curvature sensor when compared to a video-based system, in which they stated that major differences occur in the descent stage. The authors concluded that the errors were due to the video system limitations, but given our findings, this fact may be related to the viscoelasticity feature of the polymers, as discussed in Section 4.5.1.

Regarding repeatability and reproducibility, both multi-sensor fusion methods presented substantial relation for the a_1 and R^2 LFM coefficients ($0.93 < a_1 < 1.16$, $R^2 \geq 0.98$), and excellent reproducibility trial-to-trial within-subject ($\rho_C \geq 0.99$). Moreover, concerning the a_0 LFM coefficient, the standard deviation (SD) of Gyro+Acc-based method was slightly higher (about 1.9°) than IMU+POF-based method. Along the RMSE values, our IMU+POF-based MEKF method exhibits the best performance when compared to the other methods.

In contrast, the accelerometer-based method presented the lowest performance (mean $R^2 = 0.52$), and according to Iosa et al. (2014), the associated a_0 and a_1 could not be considered meaningful. In corresponding with these LFM coefficients, a $\rho_C < 0.90$ should be considered as poor reproducibility in this study (AKOGLU, 2018). In concordance, the interval $0.90 < \rho_C < 0.95$ is considered as moderate, $0.95 < \rho_C < 0.99$ as substantial, and $\rho_C > 0.99$ as almost

perfect (AKOGLU, 2018). For POF-based sensor, a mean R^2 of 0.85 was found (about 12% lower than Gyro-based and both multi-sensor fusion methods). This is probably related to the conditions explained in Section 4.5.1 and errors associated (RMSE), but it still shows a good repeatability.

Moreover, it is worth to note that the mean values of a_1 (1.07) and R^2 (0.97) presented by Gyro-based methods demonstrate that gyroscope sensors track well the movement pattern, but shift of the signals, when associated with the a_0 coefficient (-4.59 ± 5.95), compromises their performance. Additionally, it is clear the high variability of this coefficient between-subjects (see Table 4.3 and Figure 4.8 (b)). This behaviour is probably related to the gyroscope bias instability and its associated drift. In (PASCIUTO et al., 2015; BERGAMINI et al., 2014), the findings demonstrate that the drift are related not only to the variance of the noise inherent to the gyroscope signals and the time of working, but also to the amplitude of the movement/task itself.

4.5.3 Comparison of the IMU-POF Based MEKF with Other Methods in the Literature

In this subsection we aim to compare our IMU-POF based MEKF with three methods presented in the literature. To accomplished that, we implemented a Complementary Filter (CF) which uses the axis estimation method proposed by Seel, Raisch and Schauer (2014), as shown in Algorithms 2 and 3 (Appendices A.2 and A.3). Recall that CF requires a single parameter to be tuned, and we used here the same as proposed by the authors.

In the method proposed by Allseits et al. (2018), the authors used the same axis estimation method, but only the gyroscope-related part (as shown in Algorithm 2). Additionally, they used a zero knee angle (ZKA) update in a specific point identified by using a noise zero-crossing (NZC) (ALLSEITS et al., 2017). It is worth to mention that neither of both previous methods state to have performed a filter to reduce the effects of movements around the longi-

tudinal axis (made here applying a 3CRT Filter, as shown in Algorithm 1).

For the PCA-based method (MCGRATH; FINEMAN; STIRLING, 2018), another axis estimator was proposed. The authors computed the knee angular velocity using the gyroscopes measurements and the orientation data provided by the manufacturer. Then, by using the complete signal of the knee angular velocity during each walking trial, a PCA was applied in order to calculate the knee joint axis. This axis was associated with the principal component of the PCA.

As in the previous section, we evaluated the repeatability and reproducibility of all methods for the same data set. Each knee flexion-extension angle estimated by specific method was compared to that obtained by the optical system. In Table 4.5, the RMSE values are shown for all participants. In the last column, we presented again the results obtained using our method. In Figure 4.10, we presented the worst case of each method. LFM and ρ_C (CCC) coefficients are presented in Table 4.6 and Table 4.7.

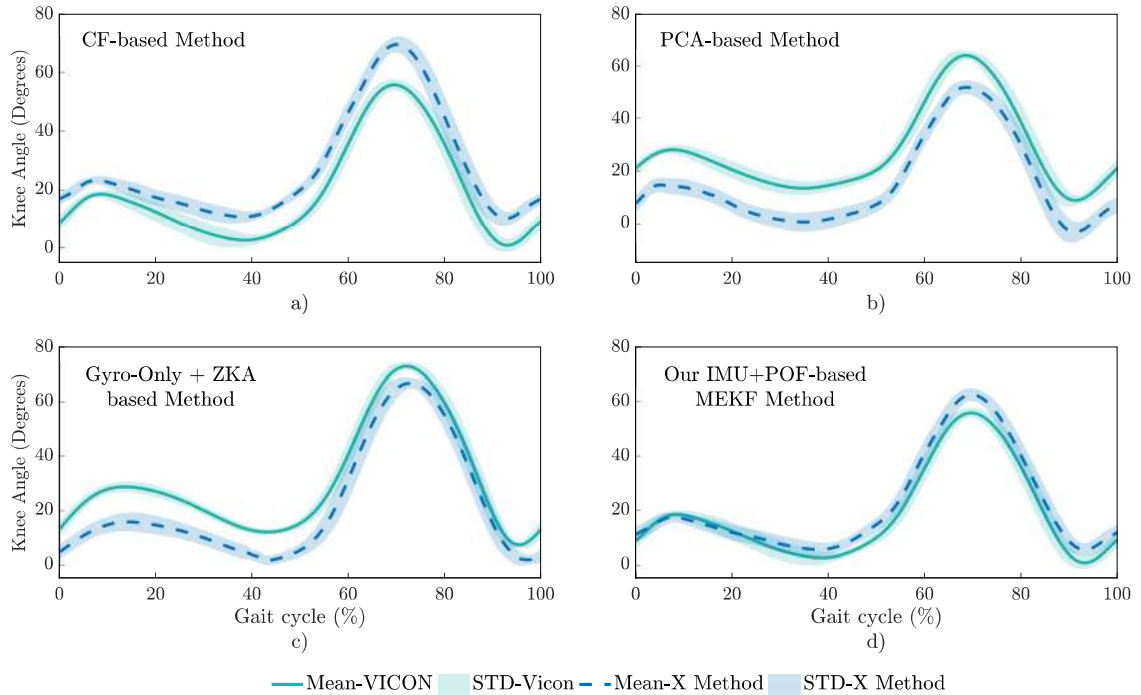


Figure 4.10: The worst case among 12 subjects (S1-S12) for each method when comparing to the reference system. (a) S11 (b) S9 (c) S9 (d) S11.

Table 4.5: Comparing the proposed method to the literature. Accuracy expressed in terms of the Root Mean Square Error (RMSE).

RMSE: Mean (SD) (Degrees)				
Participant	CF Algorithm (Gyro + Acc) [Seel-2014]	PCA-based axis estimator Algorithm [McGrath-2018]	Gyroscope Only Algorithm (with ZKA) [Allseits-2018]	Proposed Method (Gyro + Acc + POF)
S1	8.98 (0.01)	4.94 (2.19)	4.05 (1.44)	3.46 (0.62)
S2	7.11 (1.05)	12.65 (1.68)	5.60 (0.94)	3.56 (0.48)
S3	3.76 (1.17)	4.96 (1.74)	10.16 (1.05)	2.49 (0.75)
S4	4.47 (0.92)	6.38 (1.97)	5.78 (1.84)	1.89 (0.54)
S5	3.90 (1.67)	12.42 (4.89)	6.69 (1.57)	3.21 (1.53)
S6	4.56 (1.44)	6.01 (1.84)	3.58 (1.00)	2.94 (0.98)
S7	4.46 (0.73)	9.23 (1.48)	5.87 (1.49)	3.63 (0.98)
S8	3.90 (0.51)	7.74 (1.64)	11.21 (2.01)	2.98 (0.64)
S9	6.35 (3.00)	13.92 (3.68)	12.10 (2.67)	4.16 (0.68)
S10	2.76 (0.68)	8.12 (2.16)	11.90 (1.87)	1.83 (0.47)
S11	9.05 (0.92)	4.57 (1.61)	3.55 (0.76)	4.40 (0.90)
S12	7.24 (1.02)	11.20 (2.03)	9.69 (1.04)	3.80 (0.76)
Mean	5.70	8.60	7.70	3.28
SE	0.61	0.96	0.95	0.24

For each participant, values are presented as Mean (SD); SD, standard deviation; SE, standard error; CF, complementary filter; PCA, principal component analysis; ZKA, zero knee angle update.

Table 4.6: Comparing the proposed method to the literature. Repeatability and reproducibility expressed in terms of the Linear Fit Method (LFM) coefficients.

Linear Fit Method (LFM) coefficients: Mean (SD)												
Participant	CF Algorithm (Gyro + Acc) [Seel-2014]			PCA-based axis estimator Algorithm [McGrath-2018]			Gyroscope Only Algorithm (with ZKA) [Allseits-2018]			Proposed Method (Gyro + Acc + POF)		
	a_1	$a_0(^{\circ})$	R^2	a_1	$a_0(^{\circ})$	R^2	a_1	$a_0(^{\circ})$	R^2	a_1	$a_0(^{\circ})$	R^2
S1	0.95 (0.02)	9.46 (0.56)	0.97 (0.03)	0.98 (0.03)	2.86 (2.90)	0.97 (0.04)	1.00 (0.04)	-0.72 (1.57)	0.96 (0.03)	0.97 (0.02)	3.63 (0.69)	0.99 (0.01)
S2	1.08 (0.03)	4.04 (1.30)	0.98 (0.00)	1.06 (0.02)	-14.03 (1.67)	0.99 (0.00)	1.12 (0.06)	-6.62 (1.93)	0.97 (0.01)	1.05 (0.03)	-3.06 (1.27)	0.98 (0.00)
S3	1.04 (0.03)	1.62 (1.66)	0.99 (0.00)	1.07 (0.03)	-5.61 (3.30)	0.99 (0.00)	1.07 (0.06)	-11.60 (2.70)	0.98 (0.02)	0.97 (0.04)	2.05 (2.08)	0.99 (0.00)
S4	0.99 (0.02)	4.46 (1.07)	0.99 (0.00)	1.02 (0.04)	-5.02 (3.99)	0.98 (0.02)	1.03 (0.03)	-5.35 (2.26)	0.97 (0.03)	0.99 (0.02)	-0.43 (1.21)	0.99 (0.00)
S5	1.03 (0.05)	0.83 (1.91)	0.97 (0.04)	0.99 (0.05)	-10.76 (5.66)	0.98 (0.05)	1.06 (0.06)	-6.83 (2.36)	0.97 (0.05)	0.98 (0.04)	0.88 (1.87)	0.99 (0.04)
S6	1.01 (0.02)	3.58 (1.69)	0.99 (0.01)	1.04 (0.02)	-6.16 (2.32)	0.99 (0.00)	1.04 (0.03)	0.45 (1.80)	0.99 (0.01)	1.00 (0.02)	1.46 (1.66)	0.99 (0.01)
S7	0.96 (0.03)	-2.73 (1.17)	0.99 (0.01)	1.01 (0.03)	-9.07 (1.18)	0.99 (0.00)	1.00 (0.03)	-4.98 (1.07)	0.98 (0.02)	0.98 (0.03)	-1.99 (1.21)	0.99 (0.01)
S8	1.17 (0.03)	-3.96 (1.38)	0.98 (0.01)	1.12 (0.02)	-10.74 (1.97)	0.99 (0.00)	1.16 (0.06)	-13.62 (2.39)	0.90 (0.09)	1.03 (0.04)	-2.11 (1.42)	0.98 (0.01)
S9	1.00 (0.11)	0.48 (2.86)	0.88 (0.16)	0.96 (0.09)	-11.38 (3.36)	0.90 (0.15)	1.04 (0.10)	-11.11 (2.56)	0.87 (0.14)	0.93 (0.05)	2.64 (2.55)	0.95 (0.02)
S10	0.98 (0.02)	2.62 (0.91)	0.99 (0.00)	1.08 (0.02)	-9.75 (2.49)	0.99 (0.00)	1.03 (0.03)	-12.55 (1.96)	0.99 (0.01)	0.99 (0.02)	-0.50 (1.16)	0.99 (0.00)
S11	1.08 (0.02)	6.98 (1.16)	0.98 (0.00)	0.98 (0.02)	4.35 (1.88)	0.99 (0.00)	1.10 (0.02)	-2.78 (1.68)	0.98 (0.01)	1.06 (0.02)	2.10 (1.68)	0.98 (0.00)
S12	1.02 (0.03)	5.59 (1.96)	0.98 (0.01)	1.03 (0.02)	-11.60 (2.25)	0.98 (0.02)	1.05 (0.05)	-10.25 (2.31)	0.97 (0.02)	0.96 (0.02)	3.68 (1.78)	0.98 (0.00)
Mean	1.03	2.75	0.97	1.03	-7.24	0.98	1.06	-7.16	0.96	0.99	0.70	0.98
SD	0.06	3.83	0.03	0.05	5.74	0.02	0.05	4.70	0.04	0.04	2.29	0.01
Mean (abs(a_0))	-	3.86	-	-	8.45	-	-	7.24	-	-	2.04	-
SD (abs(a_0))	-	2.58	-	-	3.51	-	-	4.57	-	-	1.10	-

For each participant, values are presented as Mean (SD); SD, standard deviation; SE, standard error; CF, complementary filter; PCA, principal component analysis; ZKA, zero knee angle update; a_1 , angular coefficient, which represents the amplitude scaling factor; a_0 , intercept of the fitting line, which represents the scalar addition (shift); R^2 , coefficient of determination, which coincides with the square of the Pearson's correlation coefficient R . Ideal values of LFM parameters are $a_1 = 1$, $a_0 = 0$, $R^2 = 1$.

Table 4.7: Comparing the proposed method to the literature. Reproducibility expressed in terms of the Concordance Correlation Coefficient (CCC).

Participant	CCC (ρ_c): Mean (SD)			
	CF Algorithm (Gyro + Acc) [Seel-2014]	PCA-based axis estimator Algorithm [McGrath-2018]	Gyroscope Only Algorithm (with ZKA) [Allseits-2018]	Proposed Method (Gyro + Acc + POF)
S1	0.90 (0.01)	0.97 (0.03)	0.98 (0.02)	0.98 (0.00)
S2	0.94 (0.02)	0.82 (0.04)	0.96 (0.01)	0.98 (0.00)
S3	0.98 (0.01)	0.96 (0.02)	0.87 (0.02)	0.99 (0.01)
S4	0.97 (0.01)	0.94 (0.04)	0.95 (0.04)	0.99 (0.00)
S5	0.98 (0.02)	0.81 (0.12)	0.94 (0.03)	0.98 (0.02)
S6	0.98 (0.01)	0.96 (0.02)	0.99 (0.01)	0.99 (0.01)
S7	0.98 (0.01)	0.91 (0.03)	0.96 (0.02)	0.98 (0.01)
S8	0.98 (0.01)	0.90 (0.04)	0.82 (0.06)	0.98 (0.01)
S9	0.93 (0.11)	0.72 (0.12)	0.79 (0.10)	0.97 (0.01)
S10	0.98 (0.00)	0.89 (0.06)	0.78 (0.07)	0.99 (0.00)
S11	0.88 (0.02)	0.96 (0.02)	0.98 (0.01)	0.97 (0.01)
S12	0.94 (0.02)	0.86 (0.04)	0.90 (0.02)	0.98 (0.01)

For each participant values are presented as Mean (SD); ρ_c , concordance correlation coefficient (Lin's index); SD, standard deviation; CF, complementary filter; PCA, principal component analysis; ZKA, zero knee angle update.

A significant difference between methods was observed for RMSE values ($F_{2,21} = 10.29$, $p < 0.001$, $\eta^2 = 0.48$). *Post-hoc* tests revealed significant difference between our IMU-POF based MEKF and the other three methods ($p < 0.01$). Non-significant difference was found among the other methods (see Figure 4.11 (a)). The results show that in terms of accuracy our method is better than the other ones (mean RMSE $< 3.3^\circ$ for all participants). According to the mean RMSE values, PCA-based method presented the worst performance. Regarding repeatability and reproducibility, a significant difference between methods was found for a_1 (LFM) coefficient ($F_{2,22} = 9.75$, $p < 0.001$, $\eta^2 = 0.47$). According to the *post-hoc* comparisons, a significant difference was revealed between the GO+ZKA and the other methods ($p < 0.01$). Non-Significant difference was found for the others pairwise (see Figure 4.11 (b)).

Moreover, for a_0 (LFM) coefficient, a significant difference between methods was found ($F_{3,33} = 32.99$, $p < 0.0005$, $\eta^2 = 0.75$). *Post-hoc* tests revealed non-significant difference between our method and CF, and for PCA-based and GO+ZKA methods. Significant difference was

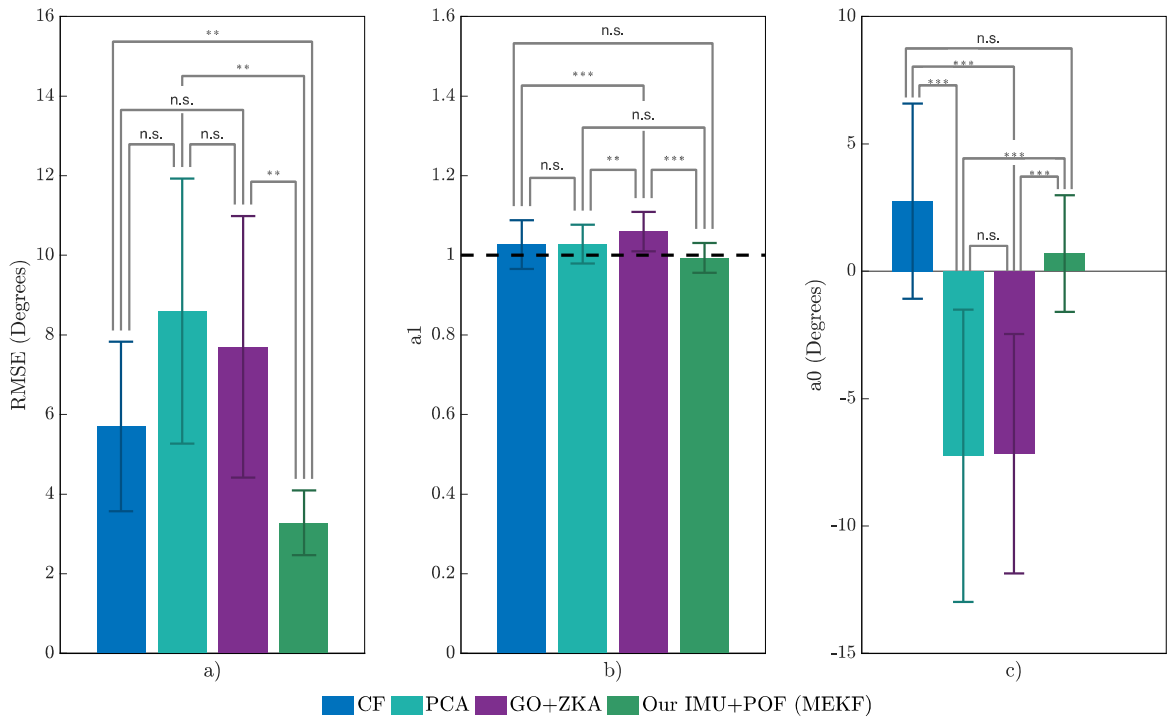


Figure 4.11: Performance of CF, PCA-based, GO+ZKA and our IM+POF (MEK) methods. Mean and standard deviation of (a) RMSE, and LFM coefficients (b) a_1 and (c) a_0 . n.s., non-significant p -value > 0.05 , ** $p < 0.01$, *** $p < 0.001$.

found between our proposed method and both PCA-based and GO+ZKA ($p < 0.001$), the same condition was found when comparing CF to both PCA-based and GO+ZKA (see Figure 4.11 (c)).

In addition, mean R^2 values were higher than 0.96 for almost all methods (see Figure 4.12). Significant difference was found between GO+ZKA and the other methods ($p < 0.01$). However, all methods presented a substantial repeatability. Interestingly, for ρ_C values and its associated Z-transformation, our proposed method was significant different of the other ones ($p < 0.05$).

Methods Comparison

In this second comparison scenario, we evaluated our method and three methods presented in the literature when used to assess the knee flexion-extension angle. The level of accuracy (RMSE), repeatability and reproducibility (LFM coefficients and CCC) using a camera-based

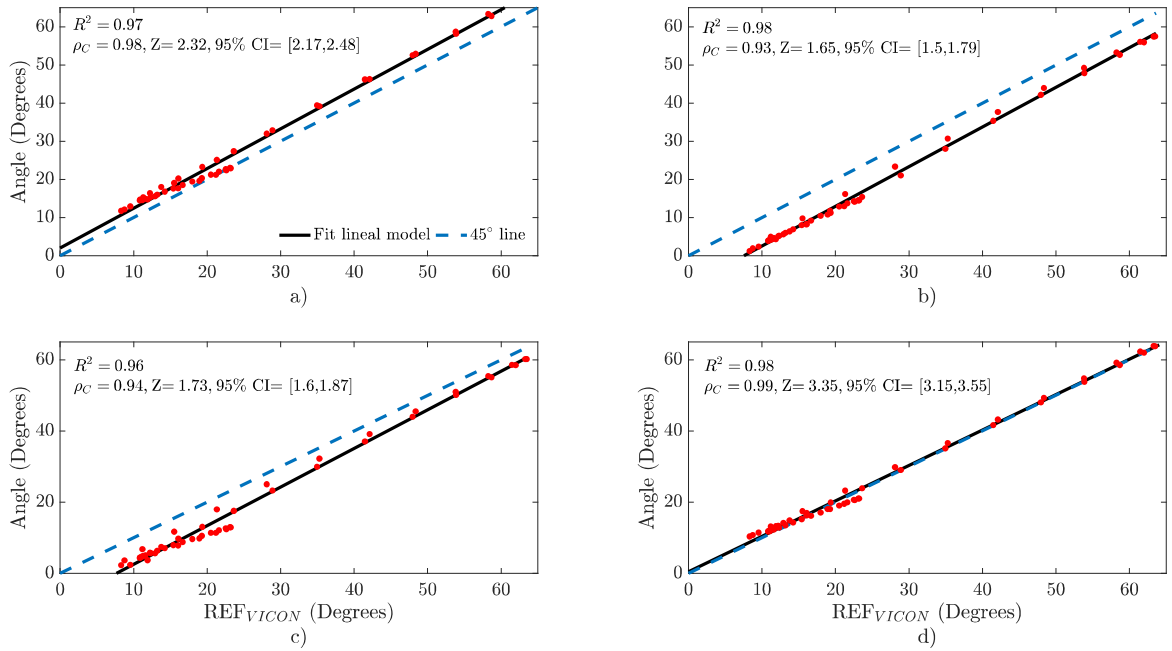


Figure 4.12: Repeatability and reproducibility of (a) Complementary Filter (CF), (b) PCA-based, (c) GO+ZKA based and (d) Our IMU+POF based MEKF method. Mean R^2 and ρ_C for all participants. Specific Method versus Reference system.

motion capture system (Vicon) as gold-standard was analyzed.

The mean RMSE value presented for our method was smaller than the other methods. For a_1 (LFM) coefficient, we can observe that all methods presented substantial values, although significant differences were presented between GO+ZKA and the other methods. This means that all methods have a good performance when assessing the range of motion (ROM). Certainly, R^2 (LFM) coefficient also confirms a good repeatability of the all methods. However, according to a_0 (LFM) coefficient and in concordance with mean RMSE values, PCA-based and GO+ZKA methods presented higher shift (offset) of the signals. This fact can also be observed with the greater dislocation and scale shift (with respect to the 45° line) (LAWRENCE; LIN, 1989)) shown by its models in Figure 4.12. Also, CF method presented a slighter shift if compared with PCA-based and GO+ZKA methods.

In (MCGRATH; FINEMAN; STIRLING, 2018) (PCA-based method), the authors reported a zero-mean RMSE of 9.69° for fifteen participants, attributing the errors to the IMU location and soft-tissue noise, mainly related to the thigh sensor and subjects' fatty tissue. However, we point out other possible error sources: (i) the use of IMU orientation measurements in indoor environments, which are highly compromised by the magnetic disturbances, and (ii) a wrong orientation estimation after IMU alignment. This last condition also applies for the work presented in (ALLSEITS et al., 2018). It is worth noting that, unlike simulated IMU data, they did not report the absolute RMSE using IMU real data. Additionally, McGrath, Fineman and Stirling (2018) carried out a comparison with the method proposed by Seel, Raisch and Schauer (2014), contrarily to our findings, the PCA-based method presented better performance than CF method in simulated conditions.

In addition, in (SEEL; RAISCH; SCHAUER, 2014) (CF method), the authors reported the results for six walking trials performed by one transfemoral amputee participant, assessing the prosthesis and the human leg. The mean RMSE values for knee flexion/extension angles were 0.71° and 3.30° for the prosthesis and the contralateral side, respectively. In our findings, at least three participants presented results approximated to those reported by Seel, Raisch and

Schauer (2014) for the human leg. However, it is difficult to make comparisons once that our participants are within normal gait pattern.

On the other hand, Allseits et al. (2018) did not reported the error of the whole gait cycle when comparing GO+ZKA to the camera-based measurements. They did present a mean difference of approximately 5° for the peak swing flexion, with a range of values approximately from -5° to 15° . They also stated that the camera-based and IMU-based systems operate with different underlying assumptions of joint biomechanical features, which limit their accuracy. In addition, another research demonstrated that the marker set choice significantly influences the estimation of gait parameters (MANTOVANI; LAMONTAGNE, 2017).

We attempt to accomplish these comparisons under similar conditions. To the best of our knowledge, barely the research in (TOGNETTI et al., 2015) proposed a fusion of signals from accelerometers and a goniometer. Thus, we accomplished the comparison task against IMU-based systems. In this way, we used the same data set when comparing our system and methods to other three methods presented in the literature. However, other conditions could generate different results. For instance, in (SEEL; RAISCH; SCHAUER, 2014; MCGRATH; FINEMAN; STIRLING, 2018), the authors used commercial IMU-based systems, MTw IMUs (Xsens, Netherlands) and Opal IMUs (APDM, Inc., USA), respectively. Contrarily, in (ALLSEITS et al., 2018) and our study, non-commercial systems were used. Also, different marker placement protocols and camera-based system were used. In summary, these conditions could explain some differences in the reported results.

As previously mentioned, a similar system was presented by Tognetti et al. (2015), where unlike an optical fiber, the authors used a goniometer based on two layers of knitted piezoresistive fabrics. They also used a Kalman Filter to fusion signals from accelerometers with that from the proposed goniometer. The mean RMSE values for five participants range from 1.07° for the slowest to 2.5° for the fastest speed during walking when comparing the system to the commercial IMU system used as reference. In addition, the mean RMSE values obtained by using the sensors separately range from 4.6° to 5.7° and 5.8° to 8.2° for the goniometer and

accelerometers, respectively. Nevertheless, given the different conditions between the studies, a direct comparison with this research is not easy.

Finally, the fact of our system and methods present the best performance (mean RMSE $< 3.3^\circ$, LFM coefficients, $a_1 = 0.99 \pm 0.04$, $a_0 = 0.70 \pm 2.29$, $R^2 = 0.98 \pm 0.01$ and $\rho_C > 0.99$) may be directly related not only to the use of a different aiding sensor, the POF curvature sensor, but also to the proposed multi-sensor fusion method.

Limitations and Future Work

Further experiments should be performed aiming to analyze the performance of our proposed system and methods in long time. It is well known that IMU sensors decrease their performance as work-time increases. In that cases, the POF curvature sensor measurements will be more exploited, again highlighting the advantage of our system. It is worth noting that little treatment of the accelerometers measurements was performed, in this way, other methods could be explored in order to remove the artifacts due to impacts and significant accelerations. Also, increasing the number of participants, including patients with pathological gait pattern will be taken in account for future works. Additionally, little adaptations of the algorithms need be done to use the proposed system in online applications.

Moreover, better conditions for POF curvature sensor could be found, in sense of improving its mechanical conditioning and alignment with real human joints. Include the fiber (without its coating) as part of the textile and more adjusted clothes could be an option. In addition, auto-calibration procedures could be provided in order to facilitate its use by ordinary people.

4.6 Preliminary Conclusions

To conclude, this chapter presented a novel IMU-POF sensor fusion system based on a knee sleeve for estimating knee flexion-extension angle. The advantages of the proposed method include the fast and easy knee sleeve placement and simple movements for the POF curvature

sensor calibration once placed in the user. The improvement gained in accuracy make this proposed system more attractive for daily clinical routine. Also, its portability and adaptability make it suitable for future online applications including in-home mobile motion monitoring in rehabilitation processes. Also, this system could be potentially benefit for exoskeletons and soft-robotics applications.

According to the results, our IMU-POF based MEKF method presented the best performance when compared with other methods in the literature, presenting a mean RMSE significant smaller ($< 3.3^\circ$ for twelve participants). The similarity indices (LFM coefficient and CCC) also showed its improvement in terms of repeatability and reproducibility. Further experiments including participants with pathological gait pattern should be made.

Chapter 5

Conclusion

Through this Ph.D. thesis, we introduced a set of novel methods to perform human motion analysis by means of lightweight and easy to use systems. It also describes the implementation of a robust multi-sensor fusion filter that combines inertial measurements and optical fiber data in order to create a more accurate output from wearable sensors.

This last chapter brings together the main conclusions of the work presented in this thesis. It also summarises the technical and scientific contributions of the developed work, and also includes the scientific papers published during the research conducted in this Ph.D. thesis.

Several contribution of this thesis were introduced in Chapters 2 to 4. The first contribution was to perform a literature study regarding methods and techniques for gait assessment using inertial sensors and optical fiber sensors, as well as data fusion approaches. This contribution was achieved in Chapter 2, which describes the fundamental knowledge, which allows a better comprehension of the analysis and the novel methods developed. It also presents the state-of-the-art fundamentals of inertial sensors, intensity variation-based Polymer Optical Fiber curvature sensors, and multi-sensor fusion methods.

The contribution number two was to develop an IMU-to-body alignment method that improves the estimation of human joint angles, aiming to reach a new approach to approximate sensor

coordinate system to anatomically-defined coordinate system. Chapter 3 describes the work that fulfil this contribution. Results from computational simulation demonstrate that, when applying the proposed method, the estimated angles are nearly equal to the expected values and consistent with the human joint's rotations. Moreover, experiment results indicate that the method is suitable to measure tridimensional angles of the hip, knee and ankle of the humans' joints during free walking. In conclusion, the proposed method is an interesting option to solve the alignment problem of human gait analysis based on inertial sensors, and is especially attractive for its simplicity, easy donning and doffing, and accurate results. It is worth to note that our method has been successfully applied and was the basis of researches in our group and different research papers were published.

The contribution number three was the implementation of a novel wearable system based on IMU sensors and a POF curvature sensor for knee joint angle estimation. The first part of Chapter 4 describes the implementation of such system, conceived as a knee sleeve device. As intended, the system is very lightweight, portable, adaptable and flexible, allowing to assess gait in a mobile way. Furthermore, the device provides very little to no disturbance in the gait pattern, is low voltage and battery operated, and transmits all data wirelessly. Those characteristics bring great freedom to the user and very little interference in the gait experience, if any.

The contribution number four was the development of a sensor fusion algorithm to merge measurements provided by accelerometers and gyroscopes with data from an optical fiber sensor. The final goal here was to improve the estimation accuracy of the human joint angles. The middle part of the Chapter 4 detailed the algorithm fulfilling this contribution. The algorithm is a Multiplicative Extended Kalman Filter (MEKF), that combines data from accelerometers, gyroscopes, and an optical fiber sensor based on kinematic constraints. In addition, the proposed fusion method is magnetometer-free seeking to avoid inaccuracies related to electromagnetic disturbances. Moreover, we proposed to deal with sensors uncertainties using reliability intervals defined during specific gait phases. For this purpose, a rule-based algorithm for gait phases

identification was also implemented.

The final contribution was to validate the proposed wearable system and the implemented data fusion algorithm against a gold standard, using a camera-based system as a reference. This validation was presented in the final part of Chapter 4, and served as a proof of concept of the whole system. Twelve subjects participated in a walking trial, in that way a total of 240 whole knee flexion-extension gait cycles were collected and analyzed. The final data from the proposed system was compared to the gold standard and other methods recently published in the state-of-the-art literature. Our proposed methods and system presented a significant better performance (mean RMSE $< 3.3^\circ$, LFM coefficients, $a_1 = 0.99 \pm 0.04$, $a_0 = 0.70 \pm 2.29$, $R^2 = 0.98 \pm 0.01$ and $\rho_C > 0.99$) when compared to other methods in the literature. Further experiments, including participants with pathological gait pattern, should be conducted.

In conclusion, in this Ph.D. thesis we present the development of a novel IMU-POF sensor fusion system and methods needed for motion analysis using wearables technologies, all the way from research, design, implementation and validation with human subjects. Through this, we contribute with the state-of-the-art of wearable systems and their use for assessing functional performance.

Nevertheless, our research has limitations that motivate future works. For instance, a further investigation on the reliability of the proposed methods and internal/external validity of the results involving more healthy participants and patients with altered gait pattern. Also, we have a particular interest in exploring other processing techniques aiming to identify and classify different gait disorders automatically.

Further experiments should be carried out in order to analyze the performance of our proposed system and methods in long time. Additionally, modifications of the algorithms should be made to use the proposed system in online applications. In addition, other ways of mechanical conditioning and alignment with real human joints should be explored for better POF curvature sensor adjustment.

5.1 Publications

We present here the papers published during the research conducted in this Ph.D. thesis as a consequence of the interaction with other researchers in our group:

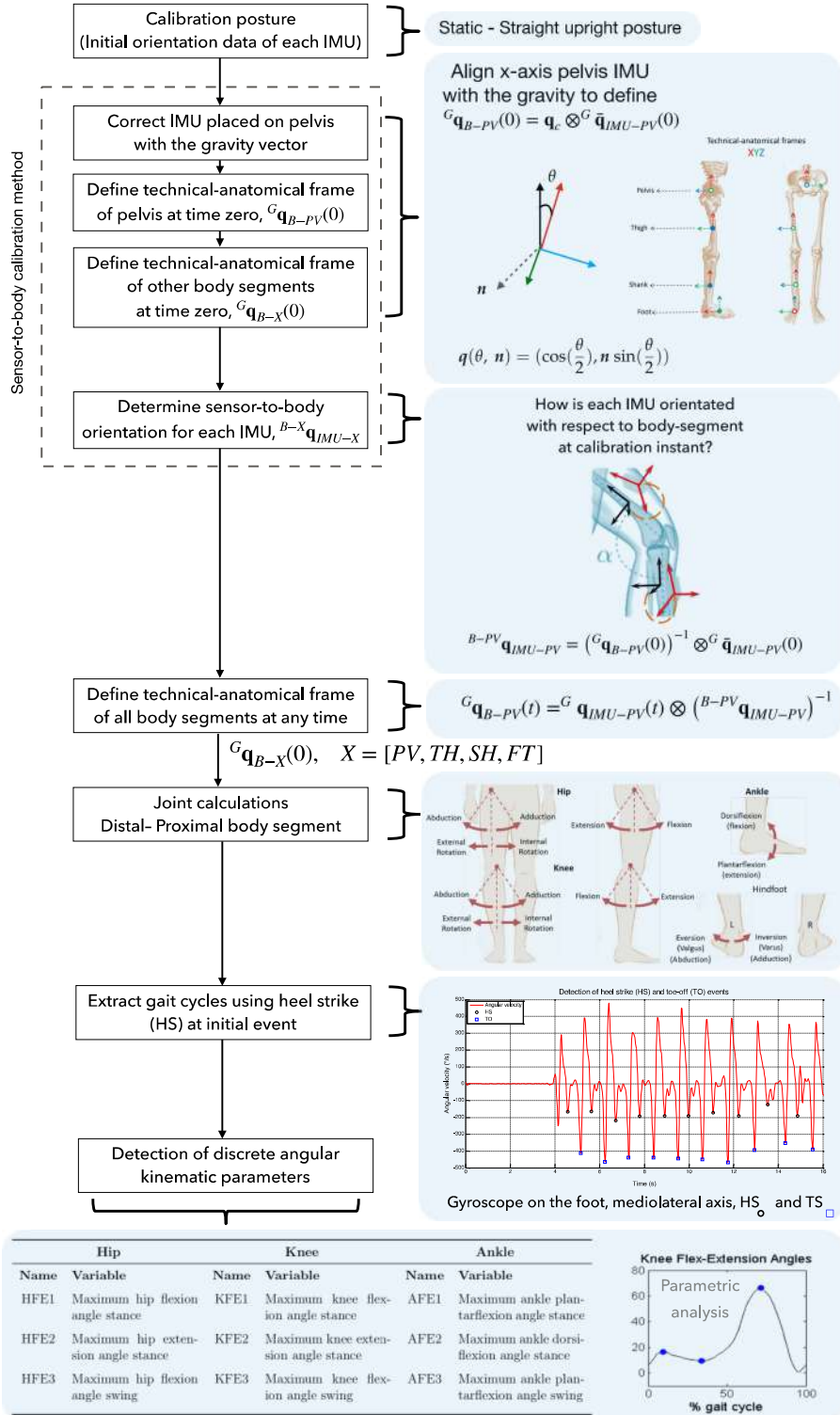
1. (Journal paper) Laura Susana Vargas-Valencia, Arlindo Elias, Eduardo Rocon, Teodiano Bastos-Filho, Anselmo Frizera. An IMU-to-Body Alignment Method Applied to Human Gait Analysis. *Sensors* 2016.
2. (Journal paper) Arnaldo G. Leal-Junior, Laura Vargas-Valencia, Willian M. Dos Santos, Felipe B.A. Schneider, Adriano A.G. Siqueira, Maria José Pontes, Anselmo Frizera. POF-IMU sensor system: A fusion between inertial measurement units and POF sensors for low-cost and highly reliable systems. *Optical Fiber Technology*, 43, 82-89, 2018.
3. (Journal paper) Arnaldo G. Leal-Junior, Anselmo Frizera, Laura Vargas-Valencia, Willian M. Dos Santos, Antônio P.L. Bó, Adriano A.G. Siqueira, Maria José Pontes. Polymer Optical Fiber Sensors in Wearable Devices: Toward Novel Instrumentation Approaches for Gait Assistance Devices. *IEEE Sensors Journal*, 7085–7092, 2018.
4. (Journal paper) Nicolas Valencia-Jimenez, Arnaldo Leal-Junior, Leticia Avellar, Laura Vargas-Valencia, Pablo Caicedo-Rodríguez, Andrés Ramírez-Duque, Mariana Lyra, Carlos Marques, Teodiano Bastos-Filho, Anselmo Frizera. A Comparative Study of Markerless Systems Based on Color-Depth Cameras, Polymer Optical Fiber Curvature Sensors, and Inertial Measurement Units: Towards Increasing the Accuracy in Joint Angle Estimation. *Electronics*, 8, 173, 2019.
5. (Journal paper) Ana Cecilia Villa-Parra, Jessica Souza-Lima, Denis Delisle-Rodriguez, Laura Vargas-Valencia, Anselmo Frizera, Teodiano Bastos. Assessment of an Assistive Control Approach Applied in an Active Knee Orthosis for Post-Stroke Gait Rehabilitation. *IEEE Transactions on Neural System and Rehabilitation Engineering*. *Submitted*, 2019.
6. (Conference Proceedings) Laura S. Vargas-Valencia, Anselmo Frizera-Neto, Teodiano Bastos-Filho. Assessment of Inertial Measurement Units' Orientation Accuracy in Static Conditions.

- XII Simpósio Brasileiro de Automação Inteligente (SBAI), Natal, October 2015.
7. (Conference Proceedings) Anderson S. Rosa, Laura S. Vargas, Anselmo Frizera, Teodiano Bastos. Real-Time Walker-Assisted Gait Analysis System using Wearable Sensors. Congresso Brasileiro de Automática (CBA), Vitoria, 2016.
 8. (Conference Proceedings) Laura Susana Vargas-Valencia, Javier Roa, Anselmo Frizera-Neto, Teodiano Bastos. Evaluación de la precisión de sensores inerciales en condiciones estáticas. IX Congreso Iberoamericano de Tecnología de Apoyo a la Discapacidad, Bogotá, 2017.
 9. (Conference Proceedings) Arnaldo G. Leal-Junior, Laura Vargas-Valencia, Anselmo Frizera, Maria José Pontes. Sensor Fusion between Inertial Measurement Units and Polymer Optical Fiber Curvature sensors for Joint Angle Assessment. IX Congreso Iberoamericano de Tecnología de Apoyo a la Discapacidad, Bogotá, 2017.
 10. (Conference Proceedings) Jessica P. Souza Lima, Laura S. Vargas-Valencia, John Villarejo, Anselmo Frizera, Teodiano Bastos. Análise de Movimento de Tronco e Membros Inferiores durante a Marcha usando Sensores IMU e sEMG. XIII Simpósio Brasileiro de Automação Inteligente, Porto Alegre, 2017.
 11. (Conference Proceedings) Arnaldo G. Leal-Junior, Gustavo B. Santi, Laura Vargas-Valencia, Anselmo Frizera, Maria José Pontes, Celso Munaro. Aplicação de Filtro de Kalman para Fusão do Sensor de Curvatura baseado em Fibra Óptica Polimérica e Giroscópio. XIII Simpósio Brasileiro de Automação Inteligente, Porto Alegre, 2017.
 12. (Conference Proceedings) Felipe Britto Azevedo Schneider, Laura Susana Vargas Valencia, Teodiano Freire Bastos-Filho, Patrick Marques Ciarelli, Anselmo Firzera. Automated Time Up and Go Test with Redundant IMU System. The 6th Brazilian Meeting of Biomechanical Engineering (ENEBI), Águas de Lindóia, 2018.
 13. (Conference Proceedings) M.A. Romero-Laiseca, L.A. Pereira da Silva, V. C. Scardua, F. B. A. Schneider, L. S. Vargas-Valencia, A. Frizera, T. F. Bastos-Fliho. Software Interface for Online Monitoring of Pedaling on an Exercise Bike. The 6th Brazilian Meeting of Biomechanical Engineering (ENEBI), Águas de Lindóia, 2018.

14. (Book Chapter) Laura Susana Vargas Valencia, Luis Eduardo Rodríguez Cheu, Ángel M. Gill Agudo, Patricio Barría, Juan C. Monero. Exosqueletos como alternativa para la movilidad. In: CYTED & Red Reasiste. (Org.). Exoesqueletos Robóticos para Rehabilitación y Asistencia de Pacientes con Daño Neurológico. 1ed. Madrid-España, Vitória-Brasil: Programa Iberoamericano de Ciencia y Tecnología para el Desarrollo, v. 1, p. 15-35, 2016.

Appendix A

A.1 Flowchart: IMU-to-Body Alignment Method



A.2 Three Criteria Filter (3CRTF)

Algorithm 1: Store samples that pass the filter.

Input: $\omega_1, \omega_2, a_1, a_2$

- 1 **Criteria 1:**
- 2 Set $N = \text{length}(\omega_1)$, $k = 1$,
- 3 **for** $t = 1$ **to** N **do**
- 4 **if** $\|\omega_1(t)\|_2 + \|\omega_2(t)\|_2 > 30$ **then**
- 5 $\omega_{1,CRT1}(k) = \omega_1(t)$
- 6 $\omega_{2,CRT1}(k) = \omega_2(t)$
- 7 $a_{1,CRT1}(k) = a_1(t)$
- 8 $a_{2,CRT1}(k) = a_2(t)$
- 9 $\eta_{CRT1}(k) = t$ // store time instants of significant motion
- 10 $k = k + 1$
- 11 **end**
- 12 **end**
- 13 Calculate longitudinal axes, l_1 and l_2 , by averaging 3D accelerations over 3 seconds (t_{3s}
 $= [\eta_{CRT1}(1), \eta_{CRT1}(t) + 300]$) during gait.
- 14 **Criteria 2 and 3:**
- 15 Set $N = \text{length}(\omega_{1,CRT1})$, $k = 1$,
- 16 **for** $t = 1$ **to** N **do**
- 17 **if** $|(\omega_{1,CRT1}/\|\omega_{1,CRT1}\|_2) \cdot l_1| < 0.2$ **and** $|(\omega_{2,CRT1}/\|\omega_{2,CRT1}\|_2) \cdot l_2| < 0.2$ **then**
- 18 $\omega_{1,CRT}(k) = \omega_{1,CRT1}$
- 19 $\omega_{2,CRT}(k) = \omega_{2,CRT1}$
- 20 $a_{1,CRT}(k) = a_{1,CRT1}$
- 21 $a_{2,CRT}(k) = a_{2,CRT1}$
- 22 $k = k + 1$
- 23 **end**
- 24 **end**

Output: $\omega_{1,CRT}, \omega_{2,CRT}, a_{1,CRT}, a_{2,CRT}$

A.3 Estimation of Knee Main Axis of Motion

Algorithm 2: Estimation of knee principal axis of motion (SEEL; RAISCH; SCHAUER, 2014).

Input: ω_1, ω_2

- 1 Initialize $\eta_{axis} = [\phi_1, \theta_1, \phi_2, \theta_2]^T$, $N = \text{length}(\omega_1)$
- 2 **for** $i = 1$ **to** 20 **do**
- 3 Calculate \mathbf{j}_1 and \mathbf{j}_2 from η_{axis}
- 4 $\mathbf{j}_1 = [\cos(\phi_1)\cos(\theta_1), \cos(\phi_1)\sin(\theta_1), \sin(\phi_1)]^T$
- 5 $\mathbf{j}_2 = [\cos(\phi_2)\cos(\theta_2), \cos(\phi_2)\sin(\theta_2), \sin(\phi_2)]^T$
- 6 **for** $t = 1$ **to** N **do**
- 7 Calculate the error vector $\mathbf{E}_{axis} \in R^{N \times 1}$ and the Jacobian $\mathbf{J}_{axis} \in R^{N \times 1}$
- 8 $\mathbf{E}_{axis}(t) = \|\omega_2(t) \times \mathbf{j}_2\|_2 - \|\omega_1(t) \times \mathbf{j}_1\|_2$
- 9 $\mathbf{J}_{axis}(t) = \frac{d\mathbf{E}_{axis}(t)}{d\eta_{axis}}$
- 10 Update η_{axis} by $\eta_{axis} - (\mathbf{J}_{axis}^T \mathbf{J}_{axis})^{-1} \mathbf{J}_{axis}^T \mathbf{E}_{axis}$
- 11 **end**
- 12 **end**

Output: $\mathbf{j}_1, \mathbf{j}_2$

A.4 Estimation of Knee Joint Position

Algorithm 3: Estimation of knee joint position (SEEL; RAISCH; SCHAUER, 2014).

Input: $\mathbf{a}_1, \mathbf{a}_2, \omega_1, \omega_2, \mathbf{j}_1, \mathbf{j}_2$

- 1 Initialize $\eta_{pos} = [o_{11}, o_{12}, o_{13}, o_{21}, o_{22}, o_{23}]^T$, $N = \text{length}(\mathbf{a}_1)$
- 2 **for** $i = 1$ **to** 20 **do**
- 3 Calculate \mathbf{o}_1 and \mathbf{o}_2 from η_{pos}
- 4 $\mathbf{o}_i = [o_{i1}, o_{i2}, o_{i3}]$ // i = 1 or 2
- 5 **for** $t = 1$ **to** N **do**
- 6 Calculate the error vector $\mathbf{E}_{pos} \in R^{N \times 1}$ and the Jacobian $\mathbf{J}_{pos} \in R^{N \times 6}$
- 7 $\mathbf{E}_{pos}(t) = \|\mathbf{a}_1(t) - \mathbf{o}_1 \times \dot{\omega}_1(t) - \omega_1(t) \times \mathbf{o}_1 \times \omega_1(t)\|_2 -$
 $\|\mathbf{a}_2(t) - \mathbf{o}_2 \times \dot{\omega}_2(t) - \omega_2(t) \times \mathbf{o}_2 \times \omega_2(t)\|_2$
- 8 $\mathbf{J}_{pos}(t) = \frac{d\mathbf{E}_{pos}(t)}{d\eta_{pos}}$
- 9 **end**
- 10 Update η_{pos} by $\eta_{pos} - (\mathbf{J}_{pos}^T \mathbf{J}_{pos})^{-1} \mathbf{J}_{pos}^T \mathbf{E}_{pos}$
- 11 **end**
- 12 Shift \mathbf{o}_1 and \mathbf{o}_2 as close as possible to the sensors
- 13 $\tilde{\mathbf{o}}_i = \mathbf{o}_i - \mathbf{j}_i \frac{(\mathbf{o}_1 \cdot \mathbf{j}_1 + \mathbf{o}_2 \cdot \mathbf{j}_2)}{2}$ // i = 1 or 2

Output: $\tilde{\mathbf{o}}_1, \tilde{\mathbf{o}}_2$

A.5 RI-ACC and RI-POF Intervals Definition

Algorithm 4: Rule-based method to define RI-ACC and RI-POF intervals (offline detection using *findpeaks* function from MATLAB).

Input: ω_{2ML} , shank angular velocity, medio-lateral axis KAV, knee angular velocity

- 1 Initialize $t_{\omega_{max}} = 60$, $t_{\omega_{min}} = 40$, $t_{h_{max}} = 1$ rad/s, $t_{h_{min}} = 1.4$ rad/s
- 2 Calculate the local maxima of ω_{2ML} , separated by more than $t_{\omega_{max}}$ samples and
 $|\omega_{2ML}| > t_{h_{max}}$
- 3 $[l_{max}, l_{ocs1}] = \text{findpeaks}(\omega_{2ML}, \text{'MinPeakDistance'}, t_{\omega_{max}}, \text{'MinPeakHeight'}, t_{h_{max}})$
- 4 Calculate the local minima of ω_{2ML} , separated by more than $t_{\omega_{min}}$ samples and
 $|\omega_{2ML}| > t_{h_{min}}$
- 5 $[l_{min}, l_{ocs2}] = \text{findpeaks}(\omega_{2ML}, \text{'MinPeakDistance'}, t_{\omega_{min}}, \text{'MinPeakHeight'}, t_{h_{min}})$
- 6 Identify HS and TO instants. Each HS is located only after a local maxima. TO is located only after a HS
- 7 Set $h = 1$, $k = 1$, $N_{max} = \text{length}(l_{ocs1})$, $N_{min} = \text{length}(l_{ocs2})$
- 8 **for** $i = 1$ **to** N_{max} **do**
- 9 **while** $(h + 1) < N_{min}$ **do**
- 10 **if** $l_{ocs1}(i) < l_{ocs2}(h)$ **and** $|\omega_{2ML}(l_{ocs2}(h))| < |\omega_{2ML}(l_{ocs2}(h + 1))|$ **then**
- 11 HS(k) = $l_{ocs2}(h)$
- 12 TO(k) = $l_{ocs2}(h + 1)$
- 13 **else**
- 14 TO(k) = $l_{ocs2}(h)$
- 15 HS(k) = $l_{ocs2}(h + 1)$
- 16 **end**
- 17 $k = k + 1$
- 18 $h = h + 2$
- 19 **end**
- 20 **end**
- 21 Identify two zero crossings between HS and TO events of each gait cycle. The first zero-crossing (ascending) is identified as aTS (\sim toe strike) and the second one (descending) as aHO (\sim heel Off)
- 22 Identify the maximum of KAV between TO and next HS events. This event is identified as eMSW (approximately the end of mid-swing phase)

Output: HS, TO, aTS, aHO, eMSW

A.6 IMU-POF based MEKF

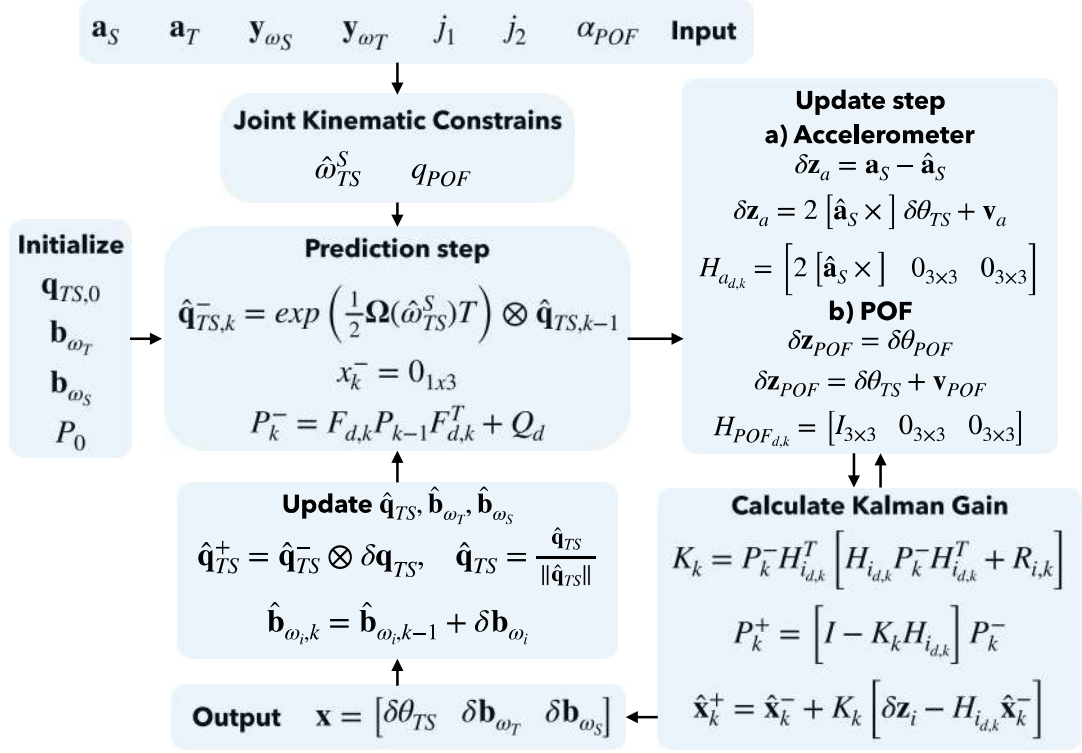
Algorithm 5: IMU-POF based MEKF.

Input: $Y_{\omega T}, Y_{\omega S}, \mathbf{j}_1, \mathbf{j}_2, \mathbf{a}_T, \mathbf{a}_S, q_{POF}$

- 1 Initialize $\hat{q}_{TS,1} = [1, 0, 0, 0]$, $P_1^- = \text{diag}(\sigma_{\delta\theta_{RS}}, \sigma_{\delta b_S}, \sigma_{\delta b_T},)$, $\hat{b}_{\omega T} = [0, 0, 0]$, $\hat{b}_{\omega S} = [0, 0, 0]$,
 $T = 0.01$, $N = \text{lenght}(Y_{\omega T})$
- 2 **for** $k = 2$ **to** N **do**
- 3 **(a) Prediction step**
- 4 Calculate $\hat{\omega}_{TS,k}$ using Equation 4.18
- 5 Compute the estimated quaternion using Equation 4.16
- 6 Calculate $[\hat{\omega}_{TS,k}^S, X]$ using Equation 4.17
- 7 Compute $F_{d,k} = \begin{bmatrix} \Psi_1 & \Psi_2 & \Psi_3 \\ 0_{3 \times 3} & I_{3 \times 3} & 0_{3 \times 3} \\ 0_{3 \times 3} & 0_{3 \times 3} & I_{3 \times 3} \end{bmatrix}$
- 8 with $\Psi_1 = e^{-[\hat{\omega}_{TS,k}^S, X]^T}$, $\Psi_2 = \frac{1}{2} \int_0^T e^{-[\hat{\omega}_{TS,k}^S, X]t} dt$, $\Psi_3 = \frac{1}{2} \int_0^T e^{-[\hat{\omega}_{TS,k}^S, X]t} dt$
- 9 Set to zero X_k^-
- 10 Compute P_k^- using Equation 4.21
- 11 **(b) Measurement update**
- 12 **(b1) Accelerometer update**
- 13 Calculate \hat{a}_s using Equation 4.23
- 14 Compute δz_a using Equation 4.27
- 15 Calculate $H_{ad,k}$ using Equation 4.28
- 16 Compute/adapt $R_{a,k}$
- 17 **if** $k \in RI-ACC$ **then**
- 18 | $R_{a,k} = \sigma_{aTS} \cdot I_{3 \times 3}$
- 19 **else**
- 20 | $R_{a,k} = A \cdot I_{3 \times 3}$
- 21 **end**
- 22 Calculate K_k (Kalman gain) and apply the update using Equation 4.32
- 23 **(b2) POF curvature sensor**
- 24 Calculate the difference quaternion δq_p using Equation 4.29
- 25 Calculate $H_{POFd,k}$ using Equation 4.31
- 26 Compute/adapt $R_{POF,k}$
- 27 **if** $k \in RI-POF$ **then**
- 28 | $R_{POF,k} = \sigma_{POF} \cdot I_{3 \times 3}$
- 29 **else**
- 30 | $R_{POF,k} = P \cdot I_{3 \times 3}$
- 31 **end**
- 32 Calculate K_k and apply again the update using Equation 4.32
- 33 Update orientation quaternion \hat{q}_{TS}^+ and biases $\hat{b}_{\omega T,k}$ and $\hat{b}_{\omega S,k}$ using Equation 4.33
- 34 **end**

Output: $\hat{q}_{TS}, \hat{b}_{\omega S}, \hat{b}_{\omega T}$

A.7 Flowchart: IMU-POF based MEKF



Bibliography

ACAR, C.; SHKEL, A. *MEMS vibratory gyroscopes: structural approaches to improve robustness*. [S.l.]: Springer Science & Business Media, 2008.

AKOGLU, H. User's guide to correlation coefficients. *Turkish journal of emergency medicine*, Elsevier, 2018.

AL-AMRI, M. et al. Inertial measurement units for clinical movement analysis: reliability and concurrent validity. *Sensors*, Multidisciplinary Digital Publishing Institute, v. 18, n. 3, p. 719, 2018.

ALAM, F.; ZHAIHE, Z.; JIA, H. A comparative analysis of orientation estimation filters using mems based imu. In: *Proceedings of the International Conference on Research in Science, Engineering and Technology, Dubai, UAE*. [S.l.: s.n.], 2014. p. 21–22.

ALEXANDER, N. B.; GOLDBERG, A. Gait disorders: search for multiple causes. *Cleveland Clinic journal of medicine*, Cleveland Clinic Foundation, v. 72, n. 7, p. 586, 2005.

ALLSEITS, E. et al. A novel method for estimating knee angle using two leg-mounted gyroscopes for continuous monitoring with mobile health devices. *Sensors*, Multidisciplinary Digital Publishing Institute, v. 18, n. 9, p. 2759, 2018.

ALLSEITS, E. et al. The development and concurrent validity of a real-time algorithm for temporal gait analysis using inertial measurement units. *Journal of biomechanics*, Elsevier, v. 55, p. 27–33, 2017.

AMOAKO, A. O.; PUJALTE, G. G. A. Osteoarthritis in young, active, and athletic individuals. *Clinical Medicine Insights: Arthritis and Musculoskeletal Disorders*, SAGE Publications Sage UK: London, England, v. 7, p. CMAMD–S14386, 2014.

ANATOMYNOTE. *Human anatomy planes*. 2019. Disponível em: <<https://www.anatomynote.com/wp-content/uploads/2019/04/5312/Human-anatomy-planes.png>>.

ASCHER, C. et al. Dual imu indoor navigation with particle filter based map-matching on a smartphone. In: IEEE. *2010 International Conference on Indoor Positioning and Indoor Navigation*. [S.l.], 2010. p. 1–5.

BAGHDADI, A.; CAVUOTO, L. A.; CRASSIDIS, J. L. Hip and trunk kinematics estimation in gait through kalman filter using imu data at the ankle. *IEEE Sensors Journal*, IEEE, v. 18, n. 10, p. 4253–4260, 2018.

- BANCROFT, J. B.; LACHAPELLE, G. Data fusion algorithms for multiple inertial measurement units. *Sensors*, Molecular Diversity Preservation International, v. 11, n. 7, p. 6771–6798, 2011.
- BENEDETTI, M. G. et al. Data management in gait analysis for clinical applications. *Clinical Biomechanics*, Elsevier, v. 13, n. 3, p. 204–215, 1998.
- BERGAMINI, E. et al. Estimating orientation using magnetic and inertial sensors and different sensor fusion approaches: Accuracy assessment in manual and locomotion tasks. *Sensors*, Multidisciplinary Digital Publishing Institute, v. 14, n. 10, p. 18625–18649, 2014.
- BERNOULLI, T. et al. Infrastructurless indoor positioning system for first responders. In: *Proceedings of the 7th International ISCRAM Conference, Seattle, USA*. [S.l.: s.n.], 2010.
- BERTOLDI, A. et al. Magnetoresistive magnetometer with improved bandwidth and response characteristics. *Review of scientific instruments*, AIP, v. 76, n. 6, p. 065106, 2005.
- BESIER, T. F. et al. Repeatability of gait data using a functional hip joint centre and a mean helical knee axis. *Journal of biomechanics*, Elsevier, v. 36, n. 8, p. 1159–1168, 2003.
- BILRO, L. et al. Optical sensors based on plastic fibers. *Sensors*, Molecular Diversity Preservation International, v. 12, n. 9, p. 12184–12207, 2012.
- BILRO, L. et al. A reliable low-cost wireless and wearable gait monitoring system based on a plastic optical fibre sensor. *Measurement Science and Technology*, IOP Publishing, v. 22, n. 4, p. 045801, 2011.
- BISHOP, E. L. et al. Error reduction in the finite helical axis for knee kinematics. *Computer methods in biomechanics and biomedical engineering*, Taylor & Francis, v. 21, n. 2, p. 186–193, 2018.
- BOTELHO, T. R. Predição de movimento baseada em eeg e semg para controle de exoesqueleto de membro inferior. Universidade Federal do Espírito Santo, 2017.
- BRENNAN, A. et al. Quantification of inertial sensor-based 3d joint angle measurement accuracy using an instrumented gimbal. *Gait & posture*, Elsevier, v. 34, n. 3, p. 320–323, 2011.
- CAI, Y. et al. Magnetometer basics for mobile phone applications. *Electron. Prod. (Garden City, New York)*, v. 54, n. 2, 2012.
- CEREATTI, A.; TROJANIELLO, D.; CROCE, U. D. Accurately measuring human movement using magneto-inertial sensors: techniques and challenges. In: IEEE. *2015 IEEE International Symposium on Inertial Sensors and Systems (ISISS) Proceedings*. [S.l.], 2015. p. 1–4.
- CHO, Y.-S. et al. Evaluation of validity and reliability of inertial measurement unit-based gait analysis systems. *Annals of rehabilitation medicine*, Korean Academy of Rehabilitation Medicine, v. 42, n. 6, p. 872, 2018.
- CIMOLIN, V.; GALLI, M. Summary measures for clinical gait analysis: a literature review. *Gait & posture*, Elsevier, v. 39, n. 4, p. 1005–1010, 2014.
- COLLE, F. et al. Comparison of three formal methods used to estimate the functional axis of rotation: an extensive in-vivo analysis performed on the knee joint. *Computer methods in biomechanics and biomedical engineering*, Taylor & Francis, v. 19, n. 5, p. 484–492, 2016.

- CUTTI, A. G. et al. 'outwalk': a protocol for clinical gait analysis based on inertial and magnetic sensors. *Medical & biological engineering & computing*, Springer, v. 48, n. 1, p. 17, 2010.
- CUTTI, A. G. et al. Ambulatory measurement of shoulder and elbow kinematics through inertial and magnetic sensors. *Medical & biological engineering & computing*, Springer, v. 46, n. 2, p. 169–178, 2008.
- DIEBEL, J. Representing attitude: Euler angles, unit quaternions, and rotation vectors. *Matrix*, v. 58, n. 15-16, p. 1–35, 2006.
- DOOLEY, E. et al. The effects of knee support on the sagittal lower-body joint kinematics and kinetics of deep squats. *Journal of biomechanics*, Elsevier, v. 82, p. 164–170, 2019.
- FAISAL, A. I. et al. Monitoring methods of human body joints: State-of-the-art and research challenges. *Sensors*, Multidisciplinary Digital Publishing Institute, v. 19, n. 11, p. 2629, 2019.
- FARAGHER, R. et al. Understanding the basis of the kalman filter via a simple and intuitive derivation. *IEEE Signal processing magazine*, v. 29, n. 5, p. 128–132, 2012.
- FASEL, B. et al. Validation of functional calibration and strap-down joint drift correction for computing 3d joint angles of knee, hip, and trunk in alpine skiing. *PloS one*, Public Library of Science, v. 12, n. 7, p. e0181446, 2017.
- FAVRE, J. et al. Functional calibration procedure for 3d knee joint angle description using inertial sensors. *Journal of biomechanics*, Elsevier, v. 42, n. 14, p. 2330–2335, 2009.
- FAVRE, J. et al. Ambulatory measurement of 3d knee joint angle. *Journal of biomechanics*, Elsevier, v. 41, n. 5, p. 1029–1035, 2008.
- FERRARI, A. et al. First in vivo assessment of "outwalk": a novel protocol for clinical gait analysis based on inertial and magnetic sensors. *Medical & biological engineering & computing*, Springer, v. 48, n. 1, p. 1, 2010.
- FILIPPESCHI, A. et al. Survey of motion tracking methods based on inertial sensors: a focus on upper limb human motion. *Sensors*, Multidisciplinary Digital Publishing Institute, v. 17, n. 6, p. 1257, 2017.
- FIORENTINO, N. M. et al. Soft tissue artifact causes significant errors in the calculation of joint angles and range of motion at the hip. *Gait & posture*, Elsevier, v. 55, p. 184–190, 2017.
- FOUNDATION, A. *Arthritis by the numbers - Book of trusted facts & figures*. 2018.
Disponível em: <<https://www.arthritis.org/Documents/Sections/About-Arthritis/arthritis-facts-stats-figures.pdf>>.
- GARGANO, J. W.; WEHNER, S.; REEVES, M. J. Presenting symptoms and onset-to-arrival time in patients with acute stroke and transient ischemic attack. *Journal of stroke and cerebrovascular diseases*, Elsevier, v. 20, n. 6, p. 494–502, 2011.
- GEBRE-EGZIABHER, D. et al. Calibration of strapdown magnetometers in magnetic field domain. *Journal of Aerospace Engineering*, American Society of Civil Engineers, v. 19, n. 2, p. 87–102, 2006.

- GHOBADI, M.; ESFAHANI, E. T. A robust automatic gait monitoring approach using a single imu for home-based applications. *Journal of Mechanics in Medicine and Biology*, World Scientific, v. 17, n. 05, p. 1750077, 2017.
- GHOBADI, M.; ESFAHANI, E. T. A robust automatic gait monitoring approach using a single imu for home-based applications. *Journal of Mechanics in Medicine and Biology*, World Scientific, v. 17, n. 05, p. 1750077, 2017.
- GHOBADI, M.; SINGLA, P.; ESFAHANI, E. T. Robust attitude estimation from uncertain observations of inertial sensors using covariance inflated multiplicative extended kalman filter. *IEEE Transactions on Instrumentation and Measurement*, IEEE, v. 67, n. 1, p. 209–217, 2018.
- GLONEK, G.; WOJCIECHOWSKI, A. Hybrid orientation based human limbs motion tracking method. *Sensors*, Multidisciplinary Digital Publishing Institute, v. 17, n. 12, p. 2857, 2017.
- GRAHAM, K. et al. Cerebral palsy. *Nature Reviews Disease Primers*, v. 2, p. 15082, 01 2016.
- GRAUROCK, D.; SCHAUER, T.; SEEL, T. User-adaptive inertial sensor network for feedback-controlled gait support systems. In: . [S.l.: s.n.], 2016.
- GREWAL, M. S.; WEILL, L. R.; ANDREWS, A. P. *Global positioning systems, inertial navigation, and integration*. [S.l.]: John Wiley & Sons, 2007.
- GROOD, E. S.; SUNTAY, W. J. A joint coordinate system for the clinical description of three-dimensional motions: application to the knee. *Journal of biomechanical engineering*, American Society of Mechanical Engineers, v. 105, n. 2, p. 136–144, 1983.
- GROSS, J. N. et al. Flight-test evaluation of sensor fusion algorithms for attitude estimation. *IEEE Transactions on Aerospace and Electronic Systems*, IEEE, v. 48, n. 3, p. 2128–2139, 2012.
- HAILEY, D. et al. Evidence of benefit from telerehabilitation in routine care: a systematic review. *Journal of telemedicine and telecare*, SAGE Publications Sage UK: London, England, v. 17, n. 6, p. 281–287, 2011.
- HAMILL, J.; KNUTZEN, K. M. *Biomechanical basis of human movement*. [S.l.]: Lippincott Williams & Wilkins, 2015.
- HANSON, A. J. Visualizing quaternions. In: ACM. *ACM SIGGRAPH 2005 Courses*. [S.l.], 2005. p. 1.
- HONG, S. K. Fuzzy logic based closed-loop strapdown attitude system for unmanned aerial vehicle (uav). *Sensors and Actuators A: Physical*, Elsevier, v. 107, n. 2, p. 109–118, 2003.
- IOSA, M. et al. Assessment of waveform similarity in clinical gait data: the linear fit method. *BioMed research international*, Hindawi, v. 2014, 2014.
- JIMÉNEZ, M. F. et al. Admittance controller with spatial modulation for assisted locomotion using a smart walker. *Journal of Intelligent & Robotic Systems*, Springer, p. 1–17, 2018.
- JOHNSON, W. et al. Stroke: a global response is needed. *Bulletin of the World Health Organization*, World Health Organization, v. 94, n. 9, p. 634, 2016.

- KALKBRENNER, C. et al. Motion capturing with inertial measurement units and kinect. In: SCITEPRESS-SCIENCE AND TECHNOLOGY PUBLICATIONS, LDA. *Proceedings of the International Joint Conference on Biomedical Engineering Systems and Technologies-Volume 1*. [S.l.], 2014. p. 120–126.
- KANG, D.; JANG, C.; PARK, F. C. Unscented kalman filtering for simultaneous estimation of attitude and gyroscope bias. *IEEE/ASME Transactions on Mechatronics*, IEEE, v. 24, n. 1, p. 350–360, 2019.
- KAO, W.-W.; CHEN, C.-K.; LIN, J.-S. Step-length estimation using wrist-worn accelerometer and gps. In: . [S.l.: s.n.], 2011.
- KAVANAGH, J. J. et al. Reliability of segmental accelerations measured using a new wireless gait analysis system. *Journal of biomechanics*, Elsevier, v. 39, n. 15, p. 2863–2872, 2006.
- KIM, K.; KIM, J. S.; KIM, Y. J. Application of nonlinear complementary filters to human motion analysis. In: IEEE. *2015 17th International Conference on E-health Networking, Application & Services (HealthCom)*. [S.l.], 2015. p. 594–595.
- KOK, M.; HOL, J. D.; SCHÖN, T. B. An optimization-based approach to human body motion capture using inertial sensors. *IFAC Proceedings Volumes*, Elsevier, v. 47, n. 3, p. 79–85, 2014.
- KOK, M.; HOL, J. D.; SCHÖN, T. B. Indoor positioning using ultrawideband and inertial measurements. *IEEE Transactions on Vehicular Technology*, IEEE, v. 64, n. 4, p. 1293–1303, 2015.
- KONG, W. et al. Development of a real-time imu-based motion capture system for gait rehabilitation. In: IEEE. *2013 IEEE International Conference on Robotics and Biomimetics (ROBIO)*. [S.l.], 2013. p. 2100–2105.
- KORTIER, H. G. et al. Hand pose estimation by fusion of inertial and magnetic sensing aided by a permanent magnet. *IEEE transactions on neural systems and rehabilitation engineering*, IEEE, v. 23, n. 5, p. 796–806, 2015.
- KOTIADIS, D.; HERMENS, H. J.; VELTINK, P. H. Inertial gait phase detection for control of a drop foot stimulator: Inertial sensing for gait phase detection. *Medical engineering & physics*, Elsevier, v. 32, n. 4, p. 287–297, 2010.
- KREHEL, M. et al. Development of a luminous textile for reflective pulse oximetry measurements. *Biomedical optics express*, Optical Society of America, v. 5, n. 8, p. 2537–2547, 2014.
- LAIDIG, D.; SCHAUER, T.; SEEL, T. Exploiting kinematic constraints to compensate magnetic disturbances when calculating joint angles of approximate hinge joints from orientation estimates of inertial sensors. In: IEEE. *2017 International Conference on Rehabilitation Robotics (ICORR)*. [S.l.], 2017. p. 971–976.
- LANGFELDER, G. et al. Z-axis magnetometers for mems inertial measurement units using an industrial process. *IEEE Transactions on Industrial Electronics*, IEEE, v. 60, n. 9, p. 3983–3990, 2013.
- LAWRENCE, I.; LIN, K. A concordance correlation coefficient to evaluate reproducibility. *Biometrics*, JSTOR, p. 255–268, 1989.

- LEAL-JUNIOR, A. et al. Polymer-optical-fiber-based sensor system for simultaneous measurement of angle and temperature. *Applied optics*, Optical Society of America, v. 57, n. 7, p. 1717–1723, 2018.
- LEAL-JUNIOR, A. G. et al. Design considerations, analysis, and application of a low-cost, fully portable, wearable polymer optical fiber curvature sensor. *Applied optics*, Optical Society of America, v. 57, n. 24, p. 6927–6936, 2018.
- LEAL-JUNIOR, A. G. et al. Viscoelastic features based compensation technique for polymer optical fiber curvature sensors. *Optics & Laser Technology*, Elsevier, v. 105, p. 35–40, 2018.
- LEAL-JUNIOR, A. G.; FRIZERA, A.; PONTES, M. J. Dynamic compensation technique for pof curvature sensors. *Journal of Lightwave Technology*, IEEE, v. 36, n. 4, p. 1112–1117, 2018.
- LEAL-JUNIOR, A. G.; FRIZERA, A.; PONTES, M. J. Sensitive zone parameters and curvature radius evaluation for polymer optical fiber curvature sensors. *Optics & Laser Technology*, Elsevier, v. 100, p. 272–281, 2018.
- LEAL-JUNIOR, A. G. et al. Polymer optical fiber sensors in wearable devices: Toward novel instrumentation approaches for gait assistance devices. *IEEE Sensors Journal*, IEEE, v. 18, n. 17, p. 7085–7092, 2018.
- LEAL-JUNIOR, A. G. et al. Hysteresis compensation technique applied to polymer optical fiber curvature sensor for lower limb exoskeletons. *Measurement Science and Technology*, IOP Publishing, v. 28, n. 12, p. 125103, 2017.
- LEAL-JUNIOR, A. G. et al. Pof-imu sensor system: A fusion between inertial measurement units and pof sensors for low-cost and highly reliable systems. *Optical Fiber Technology*, Elsevier, v. 43, p. 82–89, 2018.
- LEBEL, K. et al. Inertial measures of motion for clinical biomechanics: comparative assessment of accuracy under controlled conditions-effect of velocity. *PloS one*, Public Library of Science, v. 8, n. 11, p. e79945, 2013.
- LEE, J. K.; JEON, T. H. Imu-based but magnetometer-free joint angle estimation of constrained links. In: IEEE. *2018 IEEE SENSORS*. [S.l.], 2018. p. 1–4.
- LEE, J. K.; PARK, E. J. Quasi real-time gait event detection using shank-attached gyroscopes. *Medical & biological engineering & computing*, Springer, v. 49, n. 6, p. 707–712, 2011.
- LEE, M. et al. Kinematic model-based pedestrian dead reckoning for heading correction and lower body motion tracking. *Sensors*, Multidisciplinary Digital Publishing Institute, v. 15, n. 11, p. 28129–28153, 2015.
- LEFFERTS, E. J.; MARKLEY, F. L.; SHUSTER, M. D. Kalman filtering for spacecraft attitude estimation. *Journal of Guidance, Control, and Dynamics*, v. 5, n. 5, p. 417–429, 1982.
- LI, H. et al. Soft optical fiber curvature sensor for finger joint angle proprioception. *Optik*, Elsevier, v. 179, p. 298–304, 2019.
- LIGORIO, G.; SABATINI, A. Dealing with magnetic disturbances in human motion capture: A survey of techniques. *Micromachines*, Multidisciplinary Digital Publishing Institute, v. 7, n. 3, p. 43, 2016.

- LIM, K. Y. et al. A wearable, self-calibrating, wireless sensor network for body motion processing. In: IEEE. *2008 IEEE International Conference on Robotics and Automation*. [S.l.], 2008. p. 1017–1022.
- LUINGE, H. J.; VELTINK, P. H. Measuring orientation of human body segments using miniature gyroscopes and accelerometers. *Medical and Biological Engineering and computing*, Springer, v. 43, n. 2, p. 273–282, 2005.
- LUINGE, H. J.; VELTINK, P. H.; BATEN, C. T. Ambulatory measurement of arm orientation. *Journal of biomechanics*, Elsevier, v. 40, n. 1, p. 78–85, 2007.
- LUNNI, D. et al. Shape estimation based on kalman filtering: Towards fully soft proprioception. In: IEEE. *2018 IEEE International Conference on Soft Robotics (RoboSoft)*. [S.l.], 2018. p. 541–546.
- MADGWICK, S. O.; HARRISON, A. J.; VAIDYANATHAN, R. Estimation of imu and marg orientation using a gradient descent algorithm. In: IEEE. *2011 IEEE international conference on rehabilitation robotics*. [S.l.], 2011. p. 1–7.
- MAENAKA, K. Mems inertial sensors and their applications. In: IEEE. *2008 5th International Conference on Networked Sensing Systems*. [S.l.], 2008. p. 71–73.
- MAHONY, R.; HAMEL, T.; PFLIMLIN, J.-M. Nonlinear complementary filters on the special orthogonal group. *IEEE Transactions on automatic control*, v. 53, n. 5, p. 1203–1217, 2008.
- MANTOVANI, G.; LAMONTAGNE, M. How different marker sets affect joint angles in inverse kinematics framework. *Journal of biomechanical engineering*, American Society of Mechanical Engineers, v. 139, n. 4, p. 044503, 2017.
- MARCARD, T. von et al. Recovering accurate 3d human pose in the wild using imus and a moving camera. In: *Proceedings of the European Conference on Computer Vision (ECCV)*. [S.l.: s.n.], 2018. p. 601–617.
- MARKLEY, F. L. Attitude error representations for kalman filtering. *Journal of guidance, control, and dynamics*, v. 26, n. 2, p. 311–317, 2003.
- MAROUANE, H.; SHIRAZI-ADL, A.; ADOUNI, M. 3d active-passive response of human knee joint in gait is markedly altered when simulated as a planar 2d joint. *Biomechanics and modeling in mechanobiology*, Springer, v. 16, n. 2, p. 693–703, 2017.
- MARSCHOLLEK, M. et al. Wearable sensors in healthcare and sensor-enhanced health information systems: all our tomorrows? *Healthcare informatics research*, v. 18, n. 2, p. 97–104, 2012.
- MARTIN, H.; GROVES, P.; NEWMAN, M. The limits of in-run calibration of mems inertial sensors and sensor arrays. *NAVIGATION: Journal of The Institute of Navigation*, Wiley Online Library, v. 63, n. 2, p. 127–143, 2016.
- MCCLELLAND, J. A. et al. Knee kinematics during walking at different speeds in people who have undergone total knee replacement. *The Knee*, Elsevier, v. 18, n. 3, p. 151–155, 2011.
- MCGRATH, T.; FINEMAN, R.; STIRLING, L. An auto-calibrating knee flexion-extension axis estimator using principal component analysis with inertial sensors. *Sensors*, Multidisciplinary Digital Publishing Institute, v. 18, n. 6, p. 1882, 2018.

- MENTIPLAY, B. F. et al. Lower limb angular velocity during walking at various speeds. *Gait & posture*, Elsevier, v. 65, p. 190–196, 2018.
- MOLNAR, M. et al. A method for lower back motion assessment using wearable 6d inertial sensors. In: IEEE. *2018 21st International Conference on Information Fusion (FUSION)*. [S.l.], 2018. p. 799–806.
- MUCCIACCIA, S. *Algoritmo de Calibração de Magnetômetros Triaxiais Utilizando Ajuste de Quádrica por Distância Algébrica*. Dissertação (Mestrado) — Universidade Federal do Espírito Santo, 2017.
- MURO-DE-LA-HERRAN, A.; GARCIA-ZAPIRAIN, B.; MENDEZ-ZORRILLA, A. Gait analysis methods: An overview of wearable and non-wearable systems, highlighting clinical applications. *Sensors*, Multidisciplinary Digital Publishing Institute, v. 14, n. 2, p. 3362–3394, 2014.
- NAKAMURA, Y. et al. Bone alterations are associated with ankle osteoarthritis joint pain. *Scientific reports*, Nature Publishing Group, v. 6, p. 18717, 2016.
- NATIONS, D. o. E. U.; AFFAIRS, S. *World population ageing 2017: highlights*. [S.l.]: United Nations New York, 2017.
- NETTER, F. H.; THOMPSON, J. C. *Netters Concise Atlas of Orthopaedic Anatomy*. [S.l.]: Saunders, 2002.
- NGUYEN, K. D. et al. A wearable sensing system for tracking and monitoring of functional arm movement. *IEEE/ASME Transactions on mechatronics*, IEEE, v. 16, n. 2, p. 213–220, 2011.
- NOGUEIRA, S. L. et al. Estimation of lower limbs angular positions using kalman filter and genetic algorithm. In: IEEE. *2013 ISSNIP Biosignals and Biorobotics Conference: Biosignals and Robotics for Better and Safer Living (BRC)*. [S.l.], 2013. p. 1–6.
- NOGUEIRA, S. L. et al. Global kalman filter approaches to estimate absolute angles of lower limb segments. *Biomedical engineering online*, BioMed Central, v. 16, n. 1, p. 58, 2017.
- OKITA, N.; SOMMER, H. A novel foot slip detection algorithm using unscented kalman filter innovation. In: IEEE. *2012 American Control Conference (ACC)*. [S.l.], 2012. p. 5163–5168.
- ONDER, G. et al. Assessment of nursing home residents in europe: the services and health for elderly in long term care (shelter) study. *BMC health services research*, BioMed Central, v. 12, n. 1, p. 5, 2012.
- ORGANIZATION, W. H.; AGEING, W. H. O.; UNIT, L. C. *WHO global report on falls prevention in older age*. [S.l.]: World Health Organization, 2008.
- ORGANIZATION, W. H. et al. *Telemedicine: opportunities and developments in member states. Report on the second global survey on eHealth*. [S.l.]: World Health Organization, 2010.
- O'DONOVAN, K. J. et al. An inertial and magnetic sensor based technique for joint angle measurement. *Journal of biomechanics*, Elsevier, v. 40, n. 12, p. 2604–2611, 2007.

- PALERMO, E. et al. Experimental evaluation of accuracy and repeatability of a novel body-to-sensor calibration procedure for inertial sensor-based gait analysis. *Measurement*, Elsevier, v. 52, p. 145–155, 2014.
- PARISI, F. *Automated IMU-based Motion Analysis for Clinical Applications: the Parkinson's Disease and Post-stroke Cases*. Tese (Doutorado) — Università di Parma. Dipartimento di Ingegneria dell'Informazione, 2017.
- PASCIUTO, I. et al. How angular velocity features and different gyroscope noise types interact and determine orientation estimation accuracy. *Sensors*, Multidisciplinary Digital Publishing Institute, v. 15, n. 9, p. 23983–24001, 2015.
- PELTOLA, P.; HILL, C.; MOORE, T. Particle filter for context sensitive indoor pedestrian navigation. In: IEEE. *2016 International Conference on Localization and GNSS (ICL-GNSS)*. [S.l.], 2016. p. 1–6.
- PETERS, K. Polymer optical fiber sensors—a review. *Smart materials and structures*, IOP Publishing, v. 20, n. 1, p. 013002, 2010.
- PICERNO, P.; CEREATTI, A.; CAPPOZZO, A. Joint kinematics estimate using wearable inertial and magnetic sensing modules. *Gait & posture*, Elsevier, v. 28, n. 4, p. 588–595, 2008.
- PICERNO, P.; CEREATTI, A.; CAPPOZZO, A. A spot check for assessing static orientation consistency of inertial and magnetic sensing units. *Gait & Posture*, Elsevier, v. 33, n. 3, p. 373–378, 2011.
- POSTOLACHE, O. et al. Assistive smart sensing devices for gait rehabilitation monitoring. In: SPRINGER. *ICTs for Improving Patients Rehabilitation Research Techniques*. [S.l.], 2014. p. 234–247.
- PRENTICE, M. J. Orientation statistics without parametric assumptions. *Journal of the Royal Statistical Society: Series B (Methodological)*, Wiley Online Library, v. 48, n. 2, p. 214–222, 1986.
- RANA, M. M.; HALIM, N. Motion capture systems using optimal signal processing algorithm: A state-of-the-art literature. *Universal Journal of Communications and Network*, v. 6, n. 1, p. 1–5, 2018.
- RHUDY, M. et al. Sensitivity analysis of extended and unscented kalman filters for attitude estimation. *Journal of Aerospace Information Systems*, v. 10, n. 3, p. 131–143, 2013.
- ROETENBERG, D. et al. Compensation of magnetic disturbances improves inertial and magnetic sensing of human body segment orientation. *IEEE Transactions on neural systems and rehabilitation engineering*, IEEE, v. 13, n. 3, p. 395–405, 2005.
- ROSENBAUM, P. et al. A report: the definition and classification of cerebral palsy april 2006. *Developmental medicine and child neurology. Supplement*, v. 109, p. 8–14, 2007.
- SAAVEDRA, M. Á. et al. Clinical anatomy of the knee. *Reumatologia clinica*, Elsevier, v. 8, p. 39–45, 2012.
- SABATINI, A. M. Estimating three-dimensional orientation of human body parts by inertial/magnetic sensing. *Sensors*, Molecular Diversity Preservation International, v. 11, n. 2, p. 1489–1525, 2011.

- SABATINI, A. M. et al. Assessment of walking features from foot inertial sensing. *IEEE Transactions on biomedical engineering*, IEEE, v. 52, n. 3, p. 486–494, 2005.
- SANTOS, F. C. et al. Treatment of pain associated to knee osteoarthritis in the elderly: a randomized double-blind clinical trial with lysine clonixinate. *Revista Dor*, SciELO Brasil, v. 12, n. 1, p. 6–14, 2011.
- SCHNEIDER, F. *Assessment of Global Orientation Estimation Using Redundant Inertial and Magnetic Sensors*. Dissertação (Mestrado) — Universidade Federal do Espírito Santo, 2018.
- SCHNEIDER, R.; GEORGAKIS, C. How to not make the extended kalman filter fail. *Industrial & Engineering Chemistry Research*, ACS Publications, v. 52, n. 9, p. 3354–3362, 2013.
- SEEL, T.; RAISCH, J.; SCHAUER, T. Imu-based joint angle measurement for gait analysis. *Sensors*, Multidisciplinary Digital Publishing Institute, v. 14, n. 4, p. 6891–6909, 2014.
- SIMS, N. R.; MUYDERMAN, H. Mitochondria, oxidative metabolism and cell death in stroke. *Biochimica et Biophysica Acta (BBA)-Molecular Basis of Disease*, Elsevier, v. 1802, n. 1, p. 80–91, 2010.
- SOUÇIE, J. et al. Range of motion measurements: reference values and a database for comparison studies. *Haemophilia*, Wiley Online Library, v. 17, n. 3, p. 500–507, 2011.
- STAGNI, R. et al. Quantification of soft tissue artefact in motion analysis by combining 3d fluoroscopy and stereophotogrammetry: a study on two subjects. *Clinical Biomechanics*, Elsevier, v. 20, n. 3, p. 320–329, 2005.
- STARKEY, C.; JOHNSON, G. *Athletic training and sports medicine*. [S.l.]: Jones & Bartlett Learning, 2006.
- STOKDIJK, M. et al. Determination of the optimal elbow axis for evaluation of placement of prostheses. *Clinical Biomechanics*, Elsevier, v. 14, n. 3, p. 177–184, 1999.
- SUH, Y. S. Orientation estimation using a quaternion-based indirect kalman filter with adaptive estimation of external acceleration. *IEEE Transactions on Instrumentation and Measurement*, IEEE, v. 59, n. 12, p. 3296–3305, 2010.
- TADANO, S.; TAKEDA, R.; MIYAGAWA, H. Three dimensional gait analysis using wearable acceleration and gyro sensors based on quaternion calculations. *Sensors*, Multidisciplinary Digital Publishing Institute, v. 13, n. 7, p. 9321–9343, 2013.
- TAO, W. et al. Gait analysis using wearable sensors. *Sensors*, Molecular Diversity Preservation International, v. 12, n. 2, p. 2255–2283, 2012.
- TEAGUE, C. N. et al. Novel methods for sensing acoustical emissions from the knee for wearable joint health assessment. *IEEE Transactions on Biomedical Engineering*, IEEE, v. 63, n. 8, p. 1581–1590, 2016.
- TEUFL, W. et al. Validity, test-retest reliability and long-term stability of magnetometer free inertial sensor based 3d joint kinematics. *Sensors*, Multidisciplinary Digital Publishing Institute, v. 18, n. 7, p. 1980, 2018.

- THOMAS, C. K.; ZIJDEWIND, I. Fatigue of muscles weakened by death of motoneurons. *Muscle & Nerve: Official Journal of the American Association of Electrodiagnostic Medicine*, Wiley Online Library, v. 33, n. 1, p. 21–41, 2006.
- TIAN, Y. et al. Upper limb motion tracking with the integration of imu and kinect. *Neurocomputing*, Elsevier, v. 159, p. 207–218, 2015.
- TO, G.; MAHFOUZ, M. R. Modular wireless inertial trackers for biomedical applications. In: IEEE. *2013 IEEE Topical Conference on Wireless Sensors and Sensor Networks (WiSNet)*. [S.l.], 2013. p. 139–141.
- TOGNETTI, A. et al. Wearable goniometer and accelerometer sensory fusion for knee joint angle measurement in daily life. *Sensors*, Multidisciplinary Digital Publishing Institute, v. 15, n. 11, p. 28435–28455, 2015.
- VALADÃO, C. et al. A new controller for a smart walker based on human-robot formation. *Sensors*, Multidisciplinary Digital Publishing Institute, v. 16, n. 7, p. 1116, 2016.
- VALENCIA, L. S. V. *Sensor-to-body calibration procedure and definition of anatomical references for Gait analysis based on inertial sensors*. [S.l.]: Ufes, 2015.
- VAUGHAN, C. L. et al. *Dynamics of human gait*. [S.l.]: Kiboho publishers, 1999.
- VICON. *Plug-in Gait Reference Guide*. 2016. Disponível em: <[https://docs.vicon.com/display/Nexus25/PDF+downloads+for+Vicon+Nexus?preview=/50888706/50889377/Plug-in\\$\\%\\$20Gait\\$\\%\\$20Reference\\$\\%\\$20Guide.pd](https://docs.vicon.com/display/Nexus25/PDF+downloads+for+Vicon+Nexus?preview=/50888706/50889377/Plug-in$\\%$20Gait$\\%$20Reference$\\%$20Guide.pd)>.
- VICTOR, J. Kinematics of the normal native knee. In: *Soft Tissue Balancing in Total Knee Arthroplasty*. [S.l.]: Springer, 2017. p. 29–37.
- VILLA-PARRA, A. et al. Knee impedance modulation to control an active orthosis using insole sensors. *Sensors*, Multidisciplinary Digital Publishing Institute, v. 17, n. 12, p. 2751, 2017.
- VITALI, R. et al. Method for estimating three-dimensional knee rotations using two inertial measurement units: Validation with a coordinate measurement machine. *Sensors*, Multidisciplinary Digital Publishing Institute, v. 17, n. 9, p. 1970, 2017.
- WAEGLI, A.; SKALOUD, J. Optimization of two gps/mems-imu integration strategies with application to sports. *GPS solutions*, Springer, v. 13, n. 4, p. 315–326, 2009.
- WALTZ, E.; LLINAS, J. et al. *Multisensor data fusion*. [S.l.]: Artech house Boston, 1990. v. 685.
- WHITTLE, M. W. *Gait analysis: an introduction*. [S.l.]: Butterworth-Heinemann, 2007.
- WHO. *World report on disability*. 2011. Disponível em: <https://www.who.int/disabilities/world/_report/2011/report/en/>.
- WHO. *Spinal cord injury*. 2013. Disponível em: <<http://www.who.int/mediacentre/factsheets/fs384/en/>>.
- WHO. *Spinal cord injury: as many as 500 000 people suffer each year*. 2013. Disponível em: <<http://www.who.int/mediacentre/news/releases/2013/spinal-cord-injury-20131202/en/>>.

WHO. *Stroke, cerebrovascular accident*. 2014. Disponível em: <http://www.who.int/topics/cerebrovascular/_accident/en/>.

WITTMANN, F.; LAMBERCY, O.; GASSERT, R. Magnetometer-based drift correction during rest in imu arm motion tracking. *Sensors*, Multidisciplinary Digital Publishing Institute, v. 19, n. 6, p. 1312, 2019.

WOLTRING, H. Data processing and error analysis. In: WORTHINGTON, OH: BERLEC CORPORATION. *Biomechanics of human movement: applications in rehabilitation, sport and ergonomics*. [S.l.], 1990. p. 203–237.

WOODMAN, O. J. *An introduction to inertial navigation*. [S.l.], 2007.

WRISLEY, D. M. et al. Reliability, internal consistency, and validity of data obtained with the functional gait assessment. *Physical therapy*, Oxford University Press, v. 84, n. 10, p. 906–918, 2004.

WU, G. et al. Isb recommendation on definitions of joint coordinate system of various joints for the reporting of human joint motion—part i: ankle, hip, and spine. *Journal of biomechanics*, Elsevier, v. 35, n. 4, p. 543–548, 2002.

XIA, D.; YU, C.; KONG, L. The development of micromachined gyroscope structure and circuitry technology. *Sensors*, Multidisciplinary Digital Publishing Institute, v. 14, n. 1, p. 1394–1473, 2014.

XIA, M. et al. Performance enhancement of pedestrian navigation systems based on low-cost foot-mounted mems-imu/ultrasonic sensor. *Sensors*, Multidisciplinary Digital Publishing Institute, v. 19, n. 2, p. 364, 2019.

XING, Z.; GEBRE-EGZIABHER, D. Modeling and bounding low cost inertial sensor errors. In: IEEE. *2008 IEEE/ION Position, Location and Navigation Symposium*. [S.l.], 2008. p. 1122–1132.

YANG, A. J.; JAIN, N. B. Knee. In: *Pain Medicine*. [S.l.]: Springer, 2017. p. 65–67.

YUAN, Q. et al. Uncertainty based imu orientation tracking algorithm for dynamic motions. *IEEE/ASME Transactions on Mechatronics*, IEEE, 2019.

ZHU, R.; ZHOU, Z. A real-time articulated human motion tracking using tri-axis inertial/magnetic sensors package. *IEEE Transactions on Neural systems and rehabilitation engineering*, Citeseer, v. 12, n. 2, p. 295–302, 2004.

ZIHAJEHZADEH, S.; PARK, E. J. A novel biomechanical model-aided imu/uwb fusion for magnetometer-free lower body motion capture. *IEEE Transactions on Systems, Man, and Cybernetics: Systems*, IEEE, v. 47, n. 6, p. 927–938, 2017.

ZUBIA, J.; ARRUE, J. Plastic optical fibers: An introduction to their technological processes and applications. *Optical Fiber Technology*, Elsevier, v. 7, n. 2, p. 101–140, 2001.